POLYTECHNIQUE MONTRÉAL
affiliée à l'Université de Montréal

Parameter Estimation in a Nonlinear Vibration System via Cubature Kalman Filtering: Toward Developing Digital Twins of Hydroelectric Turbines

LUDIVINE MOYNE
Département de génie mécanique

Mémoire présenté en vue de l'obtention du diplôme de *Maîtrise ès sciences appliquées*
Génie mécanique

Novembre 2025

© Ludivine Moyne, 2025.

POLYTECHNIQUE MONTRÉAL
affiliée à l'Université de Montréal

Ce mémoire intitulé :

Parameter Estimation in a Nonlinear Vibration System via Cubature Kalman Filtering: Toward Developing Digital Twins of Hydroelectric Turbines

présenté par **Ludivine MOYNE**
en vue de l'obtention du diplôme de *Maîtrise ès sciences appliquées*
a été dûment accepté par le jury d'examen constitué de :

Njuki MUREITHI, président
Frédérick GOSSELIN, membre et directeur de recherche
Oguzhan TUYSUZ, membre et codirecteur de recherche
Cédric BÉGUIN, membre

DEDICATION

À mes parents, Francine et Sylvain, mon frère Loïc et ma soeur Lousion, merci de m'avoir encouragée et soutenue, merci pour votre soutien indéfectible malgré la distance.

ACKNOWLEDGEMENTS

I would like to sincerely thank my supervisor, Frédérick Gosselin, for giving me the opportunity to work with him on this project, and for trusting me at the start of my research journey. I am very grateful for his guidance, invaluable support, and kindness throughout this project. Thanks also to my co-supervisor, Oguzhan Tuysuz, for his support, encouragement, and insightful advice, which have been instrumental to the success of this research.

I would also like to thank Esmaeil Ghorbani for giving up his time to assist me with my project. His optimism and enthusiasm for my research, as well as his dedication, were a great source of help and motivation throughout the project.

I would like to express my gratitude to the technicians from Polytechnique Montréal, and especially to Bénédict Besner and Fabrice Danet, for their technical assistance and availability. I am thankful for their technical guidance, provision of equipment, and for sharing their expertise. I would also like to thank Julien Reis for building the experimental setup and LabVIEW measurement system during his internship.

A special thanks to the other members of this project, with whom I was able to collaborate and exchange ideas: Lucas Berthet, Mohammed Abda, Sima Rishmawi, and in particular, Vincent Laperle, who was always available to discuss my challenges and answer my questions. Moreover, I would like to thank the LM2 laboratory and all its students. Working in such a positive environment is truly invaluable and has been a key factor in achieving success. I would like to thank my sports teammates at LM2: Josua, Florian, Cédric and E'ouann; and my Québécois friends: Raphaël, Loïc, Étienne and Dorian. Finally, many thanks to Saeideh, Maryam, and Jana, for their mutual support and for the wonderful moments and discussions shared together.

Finally, I am grateful for the financial and technical support offered by Hydro-Qu´ebec and Maya HTT. I acknowledge the financial support of the Natural Sciences and Engineering Research Council of Canada (NSERC) [funding ref. ALLRP 556353-20], InnovÉÉ and IVADO.

RÉSUMÉ

Au Québec, l'hydroélectricité représente 94 % de la production totale d'énergie électrique. Cependant, ce mode de production est confronté à de nouveaux défis. La diversification des sources de production implique, en effet, l'intégration croissante de sources d'énergie renouvelable intermittentes dans le réseau électrique. La production hydroélectrique compense alors ces fluctuations, ce qui entraîne une augmentation du nombre de démarrages et d'arrêts. Les turbines hydrauliques fonctionnent alors de plus en plus souvent en dehors de leurs conditions nominales, ce qui accélère l'usure des composants et augmente le risque de défaillances prématurées, voire de pannes majeures. Afin d'optimiser la maintenance et de prévenir ces défaillances, Hydro-Québec entreprend le développement de jumeaux numériques de turbines hydroélectriques.

Un jumeau numérique constitue une représentation digitale de la turbine, offrant la possibilité d'identifier les dommages, de surveiller l'état de santé des installations, et de prédire les pannes futures, en intégrant modèles, algorithmes avancés et données issues des systèmes réels. Ce projet s'inscrit dans cette perspective, en se concentrant sur l'une des composantes du jumeau numérique : l'identification de paramètres à partir de données réelles. Compte tenu de la complexité inhérente à la modélisation directe d'une turbine à l'échelle réelle, une approche simplifiée a été adoptée, modélisant la turbine par une poutre encastrée-libre, soumise à une condition aux limites non linéaire. Ce modèle mécanique permet de reproduire le comportement dynamique du rotor et de son palier, dont les paramètres restent à déterminer. L'objectif principal de ce travail est d'estimer ces paramètres inconnus, afin de détecter et caractériser des défauts, tels que des dommages aux paliers.

L'estimation des paramètres inconnus est réalisée à l'aide d'un filtre de Kalman adapté aux données non linéaires, le *Cubature Kalman Filter* (CKF). Ce filtre combine les mesures expérimentales et le modèle mathématique décrivant la dynamique du système, afin d'identifier les paramètres inconnus. Le montage expérimental, permettant l'acquisition des données, consiste en une poutre encastrée libre, à laquelle sont ajoutés, à l'extrémité libre, des ressorts perpendiculaires à la direction du mouvement. Ce système représente un palier endommagé, dont on veut identifier les coefficients inconnus. La poutre est mise en mouvement par un excitateur modal. Un capteur de force mesure l'effort appliqué à la poutre, tandis qu'un accéléromètre enregistre l'accélération en bout de poutre, avec une fréquence d'échantillonnage de 2048 Hz. Le modèle mathématique est ensuite calibré à partir de données expérimentales linéaires pour représenter le plus fidèlement possible la dynamique de la poutre, analogue à

un arbre de turbine saine.

Le CKF permet de résoudre des problèmes inverses et d'estimer les raideurs linéaires et non linéaires associées au système de ressorts. Les tests effectués sur des données synthétiques démontrent la précision de la méthode, avec des erreurs d'estimation respectives de 0,8 % et 1 % pour les raideurs linéaires et non linéaires. Toutefois, la capacité du CKF à identifier le terme non linéaire dépend de l'amplitude du déplacement en bout de poutre : si celui-ci est trop faible, les effets non linéaires deviennent négligeables sur la dynamique de la poutre, et la raideur non linéaire est impossible à estimer.

Les raideurs sont ensuite estimées à partir des données expérimentales mesurées sur la poutre linéaire (sans ressorts), et non linéaire. Estimer la raideur en flexion de la poutre linéaire démontre que l'utilisation d'une excitation multi-fréquentielle améliore significativement la qualité de l'identification des paramètres. En effet, ce type d'excitation fournit une réponse dynamique plus riche, ce qui réduit les problèmes de non-unicité typiques des problèmes inverses. Ainsi, pour une excitation harmonique, une erreur de 16 % sur la fréquence propre est observée, contre seulement 1 % pour une excitation de type chirp. Enfin, les erreurs d'estimation des raideurs linéaire et non linéaire sont respectivement de 7 % et 18 %, tandis que la simulation du modèle avec ces paramètres conduit à une erreur de 3 % par rapport à la courbe expérimentale de réponse en fréquence.

Ce travail constitue une étape fondamentale vers la conception d'un jumeau numérique, capable non seulement d'identifier, mais aussi de prédire l'évolution de dommages structurels dans les turbines hydrauliques. Intégrer cette méthode d'estimation de paramètres inconnus à d'autres algorithmes plus avancés contribue à la construction du jumeau numérique. À terme, la mise en œuvre d'un tel outil permettra une surveillance en temps réel et une gestion proactive des équipements, fiabilisant les installations, en réduisant les risques de panne et les coûts d'exploitation.

ABSTRACT

The increasing integration of intermittent renewable energy sources into the power grid requires compensation through hydroelectric generation. As a result, hydro-turbines operate more frequently under off-design conditions, which accelerates wear and increases the risk of premature damage or even catastrophic failure. To predict failures and optimize maintenance operations, Hydro-Quebec aims to develop digital twins (DT) of Francis turbines. Given the complexity of directly constructing a DT for a full-scale turbine, a cantilever beam with a nonlinear boundary condition simplifies the turbine, and model the vibrating rotor-shaft line with unknown bearing coefficients. This project focuses on one key aspect of DT development: estimating unknown parameters to detect and characterize defaults such as bearing damage. The cantilever beam system is excited with a modal shaker. A force sensor measures the input force applied to the beam, while an accelerometer records the tip acceleration response. Before solving inverse problem, the model is calibrated to match the simulated response with the experimental linear data. The linear beam represent the undamaged Francis turbine and introducing a nonlinear spring system at its free end, reproduces a damaged nonlinear bearing, for which unknown parameters are estimated. Parameter estimation and inverse problem solving are performed with the cubature Kalman filter (CKF). This filtering approach combines experimental data with the mathematical model of the system to estimate both the linear and nonlinear stiffness coefficients associated with the nonlinear boundary condition. The proposed framework is first verified with synthetic data, demonstrating that the CKF accurately identifies the linear and nonlinear stiffness coefficients, with respective estimation errors of 0.8 % and 1 %. However, the ability to estimate the nonlinear stiffness depends on the beam tip displacement: when the displacement amplitude is too small, the nonlinear effect becomes negligible and the CKF cannot reliably estimate the nonlinear term. Considering the response of the beam under a multi-frequency excitation also improves parameter identification as shown when estimating the beam's bending stiffness. This signal provides richer information for the filter and mitigates non-uniqueness issues commonly encountered in inverse problem solving. For harmonic excitation an error of 16 % on the natural frequency is ached compared to 1 % for a chirp excitation. Finally, the estimation of the linear and nonlinear spring stiffness yielded errors of 7 % and 18 %, respectively. Simulating the model with these estimated parameters shows a 3 % error when compared with the experimental frequency response curve. Developing a complete DT, however, requires integrating this estimation approach with complementary algorithms to form a hybrid twin that identifies and predicts structural damage.

TABLE OF CONTENTS

DEDICATION iii

ACKNOWLEDGEMENTS iv

RÉSUMÉ v

ABSTRACT vii

TABLE OF CONTENTS viii

LIST OF TABLES xi

LIST OF FIGURES xii

LIST OF SYMBOLS AND ACRONYMS xvii

LIST OF APPENDICES xxii

CHAPTER 1 INTRODUCTION 1
- 1.1 Motivations 2
  - 1.1.1 Digital twinning for predictive maintenance in hydropower 2
  - 1.1.2 Hybrid modeling and parameter estimation in digital twins 2
  - 1.1.3 The nonlinear cantilever beam as a simplified experimental system . 3
- 1.2 Thesis goals and organization 4

CHAPTER 2 LITERATURE REVIEW 7
- 2.1 Kalman filtering : 7
  - 2.1.1 The linear Kalman filter 7
  - 2.1.2 Kalman filter for nonlinear systems 9
  - 2.1.3 The cubature Kalman filter : 10
  - 2.1.4 Kalman filter with adaptive covariance and parameter tuning 13
  - 2.1.5 Parameter estimation with Kalman filtering techniques 15
- 2.2 The nonlinear cantilevered beam setup 17
  - 2.2.1 Beam excited by a modal shaker 19
  - 2.2.2 Beam shaker interactions 20
  - 2.2.3 Modal analysis 21

2.3 Duffing oscillator 24

CHAPTER 3 SYNTHESIS OF THE LITERATURE REVIEW AND REASEARCH OBJECTIVES 29
3.1 Synthesis of the literature review 29
3.2 Research objectives 29

CHAPTER 4 CHARACTERIZATION OF THE BEAM SETUP 31
4.1 The experimental setup 31
4.1.1 Experimental procedure to quantify the linear and nonlinear stiffness 33
4.1.2 Spring fixation design 35
4.2 Static force displacement tests 38
4.2.1 Experimental validation: static testing of the linear beam 38
4.2.2 Experimental characterization of the nonlinear springs system 40
4.3 Beam setup modeling 41
4.3.1 General assumptions and equation of motion 41
4.3.2 Discretization through Galerkin method 42
4.3.3 Rayleigh damping model 45
4.4 Modal analysis of the cantilevered beam without the springs 46
4.5 Dynamic response of the cantilever beam setup: linear case, the beam without springs and nonlinear case, the beam with springs 47
4.5.1 Comparison of experimental and simulated data for the cantilever beam without springs 48
4.5.2 Dynamic response of the beam with the perpendicular springs 51

CHAPTER 5 PARAMETER ESTIMATION OF THE BEAM SETUP WITH CUBATURE KALMAN FILTER 55
5.1 Methodology: The cubature Kalman filter framework 55
5.2 Parameter estimation with synthetic data 58
5.3 Parameter estimation with experimental data 63
5.3.1 Configuration 1: The linear cantilevered beam, without the springs . 64
5.3.2 Configuration 2: The nonlinear cantilevered beam 69

CHAPTER 6 CONCLUSION 74
6.1 Summary of Works 74
6.2 Limitations 75
6.3 Future Research 76

REFERENCES 78

APPENDICES 86

LIST OF TABLES

Table 2.1 **Comparison of Kalman filter variants for nonlinear state estimation** 11

Table 4.1 **Physical parameters of the system** 32

Table 4.2 **Modal properties of the cantilevered beam, without the springs and with the accelerometer and the magnet and force sensor assembly, obtained with the FRF** 48

Table 4.3 **Natural frequencies f_n of the first three modes for different stiffness values, compared with experimental values obtained from the FRF analysis** 50

Table 4.4 **Fitting input values compared to excepted values** 54

Table 5.1 **Initial Values of states, parameters and variances, for the initialization of the CKF** 59

Table A.1 **Experimental signal types and initial Values of states, parameters and variances, for the initialization of the CKF, for the two tests cases presented in Figure 5.5** 86

LIST OF FIGURES

Figure 1.1 **Schematic of the digital twin framework highlighting the specific cantilever beam system developed and analyzed to achieve system identification with the Cubature Kalman Filter (CKF)** 5

Figure 2.1 **Schematic of nonlinear spring system at the free end of the beam** 19

Figure 2.2 **Force sensor measurement when the shaker apply a sinusoidal excitation.** **(a)** Recorded force when the excitation is applied far from the resonant frequency, illustrating reduced beam-shaker interaction. **(b)** Recorded force when the beam system is excited at its resonant frequency, showing strong beam-shaker interaction effects 22

Figure 2.3 **Frequency–amplitude curves near the primary resonance simulated with Eq.**(2.17)**.** Softening ($\alpha = -0.0006$ and $\alpha = -0.0004$); hardening ($\alpha = 0.0006$) an linear ($\alpha = 0$) behavior are plotted. All cases are calculated with $\zeta = 0.02$ and the dashed lines represents the unstable regions. Backbones curves are also plotted with dash-dot lines 27

Figure 4.1 **Experimental setup.** **(a)** Schematic of the beam. **(b)** Schematic of the springs system at the end of the beam, highlighting of the no-load spring length l_0 and the preload length a. **(c)** Global photograph of the experimental setup - the beam measures half a meter. **(d)** Top view photograph of the spring mechanism 32

Figure 4.2 **Photograph of the tip of the beam post-processed in Tracker software** 34

Figure 4.3 **Diagram of the different spring assemblies.** **(a)** Cut view of Assembly 1: the springs are hooked onto the beam. **(b)** Cut view of Assembly 2: the springs are rigidly compressed between a screw and the beam. **(c)** Top view of Assembly 3: a nylon thread knot the springs to the beam 36

Figure 4.4 **Temporal response of the beam to a sin chirp excitation around the first natural frequency** from 10 Hz to 25 Hz, with a frequency rate of 0.037 Hz/s, for 50 mV and 150 mV of input voltages sent to the modal shaker. **(a)** Acceleration response at the tip of the beam. **(b)** Excitation force applied to the beam by the model shaker, with a zoomed-in view in the resonance region. **(c)** Input voltage signal sent to the shaker, with a zoomed-in view in the resonance region. (–·–·-) and (- - - -) are respectively the resonance region for the signal with 50 mV input voltage and 150 mV input voltage 37

Figure 4.5 **Static force displacement at the free end of the beam for the 3 different springs assemblies**, with corresponding cubic curve fitting equations 38

Figure 4.6 **Static displacement at the tip of the beam without the springs and the sensors, when imposing a known force,** with the 95 % confidence interval (shadow). Comparison with the theoretical stiffness of the beam, $EI_{th,geom}$ (–·–·-) 39

Figure 4.7 **Static displacement at the tip of the nonlinear beam with the springs, when imposing a known force**, with its 95 % confidence interval (shadow), and the corresponding cubic equation from curve fitting (- - - -). Comparison with the linear part of the equation (——), to illustrate the nonlinear behavior of the beam. The dotted curve (–·–·-) is obtained with Equations (4.2) and (4.3) from Shaw et al. (2016) 41

Figure 4.8 **Modal energy distribution** for the cantilevered beam, without the springs and accounting for the mass of the accelerometer and the magnet and force sensor assembly, excited at 20 Hz and with a force amplitude of 3 N 45

Figure 4.9 **Frequency response function and curve fitting for modal identification, of the cantilevered beam without the springs, and with the mass of the accelerometer and the magnet and force sensor assembly.** **(a)** Experimental (·····) and filtered (——) FRF of the beam. **(b)**, **(c)**, **(d)** are zoomed-in view of the first three resonance peaks (——) and the results of the curve fitting (- - - -) 47

Figure 4.10 **Response of the linear beam, without springs and with the accelerometer and the magnet and force sensor assembly, in the resonance region as a function of frequency.** (a) Steady-state acceleration amplitude at different frequencies for experimental data (+), and simulated data considering the experimental excitation force (△). (b) Experimental excitation force amplitude recorded by the force sensor at different frequencies 49

Figure 4.11 **Response of the beam with the perpendicular springs in the resonance region as a function of frequency.** (a) Steady-state acceleration amplitude at different frequencies for experimental data (+). (b) Experimental excitation force amplitude recorded by the force sensor at different frequencies 52

Figure 4.12 **Temporal response of the nonlinear beam with the springs to a sin chirp excitation around the first natural frequency**, from 8 Hz to 18 Hz, with a frequency rate of 0.083 Hz/s, for 150 mV input voltage. **(a)** Acceleration response at the tip of the beam. **(b)** Excitation force applied to the beam by the model shaker 53

Figure 4.13 **Dimensionless frequency-amplitude curve**, comparing experimental data points (+) with the theoretical fit (——), around the first natural frequency 54

Figure 5.1 **Schematic of the CKF framework.** Based on the prior knowledge, the CKF estimates the augmented state space vector $\mathbf{z}$ (-·-·-). While $t < t_{max}$, CKF estimates both states $\hat{\mathbf{x}}$ and parameters $\hat{\theta}$, from the mathematical model Ω, during the prediction step. Then it updates the estimation according the the measurement $\mathbf{y}$. Running multiple CKF iterations, NOMAD subsequently optimizes the process and noise covariance matrices and their forgetting factors $(\mathbf{Q}, \mathbf{R}, \alpha_Q, \alpha_R)$ by minimizing the physical loss $\mathcal{L}$ (- - - -) 56

Figure 5.2 **CKF state and parameter estimations from synthetic acceleration data**, when the beam is subjected to an harmonic excitation 15 N and 14 Hz. **(a)** 3D schematic of the nonlinear beam with the springs. **(b), (c)** Respectively, CKF estimation (——) of the nonlinear stiffness k_{NL} and the linear stiffness k_L, compared to the true value (- - - -), during the first 5 seconds. The shadow represents the 3σ uncertainty interval of the estimate. The CKF also estimates the states: it reconstruct the true acceleration form the noisy measurements **(d)** and estimates the velocity **(e)** and the deflection **(f)** 60

Figure 5.3 **Ability of the CKF to estimate the linear and nonlinear stiffness (k_L et k_{NL}) as a function of the displacement amplitude at the tip of the beam. (a)** Force contribution of the linear (- - - -) and nonlinear terms (——) of the beam's equation of motion (4.14) as a function of tip displacement. **(b)** Relative estimation error of the CKF for linear (★) and nonlinear (◯) stiffness parameters as a function of the displacement amplitude at the beam tip. **(c)** Estimated nonlinear stiffness coefficient k_{NL} as a function of tip displacement, with associated 2σ uncertainty interval (◯). The estimations are compared with the expected value (- - - -) and initial value (–·–·-) of k_{NL} 62

Figure 5.4 **NOMAD optimization process with associated CKF parameter estimation**, under experimental sine excitation at 18 Hz with an input voltage of 150 mV. **(a)** Physical loss of the CKF estimation as a function of the NOMAD iteration i. **(b)** Estimated parameters at different iteration steps (——), with their 3σ uncertainty intervals (shadow), compared to the true value (- - - -) 65

Figure 5.5 **CKF estimation of the intrinsic stiffness of the beam EI for different input signals. (a)** Under sine excitation at 15 Hz with an input voltage of 150 mV. **(b)** Under a chirp excitation with a cyclic frequency sweep from 9 Hz to 11 Hz and back to 9 Hz, repeated 3 times over 60 seconds. In both cases, the estimated parameters (——) are compared with the bending stiffness obtained with geometrical parameters (- - - -), and with the experimental value obtained from static tests (–·–·-). The shaded area represents the 3σ uncertainty interval. **(c)** Reconstructed tip displacement of the beam under chirp excitation 68

Figure 5.6 **CKF estimation results with the measured acceleration response at the tip of the beam under chirp excitation as the filter input signal.** **(a)** Time evolution of the estimated linear stiffness k_L. **(b)** Time evolution of the estimated nonlinear stiffness k_{NL}. The shaded regions around the estimated parameters represent the 2σ uncertainty intervals. **(c)** Comparison between the experimental acceleration and its CKF-based reconstruction 71

Figure 5.7 **Response of the nonlinear beam under harmonic excitation as a function of the excitation frequency in the resonance region.(a)** Comparison between the experimental steady-state acceleration amplitude and the simulated amplitude, considering the experimental force as input, and the estimated linear and nonlinear stiffness obtained from the CKF. **(b)** Amplitude of the experimental excitation force recorded by the force sensor at various frequencies 72

LIST OF SYMBOLS AND ACRONYMS

Acronyms

CKF	Cubature Kalman filter
DT	Digital Twin
EKF	Extended Kalman Filter
EMA	Experimental Modal Analysis
FRF	Frequency Response Function
KFT	Kalman Filtering Techniques
LKF	Linear Kalman Filter
MDOF	Multi Degree Of Freedom
NRMSE	Normalized Root Mean Square Error
SCKF	Square Root Cubature Kalman Filter
SDOF	Single Degree Of Freedom
UKF	Unscented Kalman filter

Symbols

Linear and Cubature Kalman filter

$\mathbf{x}$	State vector
$\hat{\mathbf{x}}$	Estimated state vector
θ	Unknown parameters vector
$\hat{\theta}$	Estimated parameters vecteor
$\mathbf{z}$	Augmented state vector
$\hat{\mathbf{z}}$	Estimated augmented state vector
$\mathbf{y}$	measurement vector
$\hat{\mathbf{y}}$	Estimated measurement vector
$\mathbf{v}$	Process noise vector
$\mathbf{w}$	Measurement noise vector
$\mathbf{Q}$	Process noise covariance matrix
$\mathbf{R}$	Measurement noise covariance matrix
α_Q	Process forgetting factor
α_R	Measurement forgetting factor
$\mathbf{F}$	State transition matrix
$\mathbf{H}$	Measurement matrix
$\mathbf{f}$	Transition function
$\mathbf{h}$	Measurement function
$\mathbf{P}$	Covariance matrix
$\mathbf{S}$	"Square root" of the covariance matrix
$\mathbf{K}$	Kalman gain
$\boldsymbol{\chi}$	Sigma points
$\boldsymbol{\Upsilon}$	Second set of sigma points
$\boldsymbol{\xi}$	Vector to build the sigma points
w	Weigth of the sigma points
n	Lenght of the state vector
M	Number of unknown parameters
Δt	Time step
t_{max}	Final time
k	Time increment
$\mathcal{L}$	Physic aware loss function
σ	Standard deviation of the estimated parameter
it	Iteration number of the NOAMD optimization process

Duffing oscillator

x	Displacement
y	Dimensionless displacement
Y	Steady state displacement amplitude
τ	Dimensionless time
m_d	Mass
c	Damping
f	Force magnitude
ω	Frequency
ω_0	Natural frequency
α	Nonlinear coefficient
Ω	Dimensionless frequency
ζ	Dimensionless damping coefficient
ϕ	Phase

Perpendicular springs system

F_k	Restoring force of the springs
k	Spring stiffness
l	Length of the springs when the beam is moving
l_0	Initial spring length
a	Length of the springs when the beam is at rest
θ	Spring angle
P	Force displacement curve
k_L	Linear stiffness
$k_{L,exp}$	Linear stiffness determined experimentally
$k_{L,th}$	Linear stiffness obtained with the formulas
k_{NL}	Nonlinear stiffness
$k_{NL,exp}$	Nonlinear stiffness determined experimentally
$k_{NL,th}$	Nonlinear stiffness obtained with the formulas

Cantilever beam model

w	Deflection of the beam
ρ	Material density
E	Young's modulus

L	Lenght of the beam
L_S	Shaker location
L_{acc}	Accelerometer location
b	Width of the beam
h	Thickness of the beam
I	Moment of inertia of the beam
A	Cross section of the beam
EI	Stiffness of the beam
$EI_{th,geom}$	Theoretical stiffness of the beam
$EI_{th,exp}$	Experimentally determined stiffness of the beam
EI_{corr}	Corrected stiffness of the beam
m	Mass per unit lenght
m_S	Mass of the magnet and force sensor
m_{acc}	Mass of the accelerometer
M_{cor}	Corrected modal mass
ζ	Damping ratio
t	Time
Ω_e	Excitation frequency
F_0	Excitation force magnitude
N	Number of beam mode shapes
q_i	i_{th} Modal coordinate
$\mathbf{q}$	Generalized coordinate vector
ϕ_i	i_{th} Cantilever beam mode shape
λ_i	i_{th} Beam eigenfrequency
σ_i	i_{th} Modal coefficient
$\mathbf{M}$	Mass matrix
$\mathbf{C}$	Damping matrix
$\mathbf{K_L}$	Linear stiffness matrix
$\mathbf{K_{NL}}$	Nonlinear stiffness matrix
$\mathbf{F}$	Force vector
α	Mass proportional damping coefficient
β	Stiffness proportional damping coefficient

Modal analysis

$\mathbf{H}_{FRF}$	Frequency response function

$\mathbf{A}_{FRF}$	Spectrum of the output acceleration response
$\mathbf{F}_{FRF}$	Spectrum of the input excitation force
ω_n	Natural angular frequency of the n_{th} mode
f_n	Natural frequency of the n_{th} mode
ζ_n	Modal damping ration of the n_{th} mode
K_n	Modal stiffness coefficient of the n_{th} mode
M_n	Modal mass of the n_{th} mode
E_n	Energy contribution of the n_{th} mode
W_n	Modal amplitude of the n_{th} mode

General symbols and Mathematics

$\mathbf{I}$	Identity matrix
δ	Kronecker symbol
$\mathcal{N}$	Gaussian distribution
$^\top$	Matrix transpose
j	Imaginary unit

LIST OF APPENDICES

Appendix A Initialization of the CKF 86

CHAPTER 1 INTRODUCTION

In order to achieve carbon neutrality, Quebec aims to produce 100 % green electricity by 2050. Currently, hydroelectric plants produce around 94 % of the province's electricity, making Quebec one of the world's greenest energy producers (Gouvernement du Canada, 2024). However, the energy demand increases due to economic development and the population growth. Further expansion of hydropower production is constrained by limited suitable sites, high environmental considerations, and complex infrastructure requirements. Therefore, to meet demand and achieve carbon neutrality , Hydro-Québec plans to optimize the energy consumption and diversify the energy mix by integrating other renewable sources such as wind and solar energy (Hydro-Québec, 2023, 2024, 2025).

The intermittent nature of these renewable energy sources, driven by weather variability and day–night cycles, causes fluctuations in the power grid. Hydro-turbines must compensate for these variations through more frequent starts, stops, and load changes, operating more often under off-design conditions. Such fluctuations impose additional mechanical strain on turbine components, accelerating wear, and increasing the risk of failures. Maintenance operations must be carried out more frequently, particularly in older facilities, where aging infrastructure requires careful monitoring and more regular preventive maintenance to avoid costly breakdowns and revenue losses due to downtime.

In many hydroelectric facilities, maintenance follows fixed preventive schedules where turbines are routinely serviced or overhauled at predetermined intervals, regardless of the equipment's current condition. While straightforward, this approach leads to unnecessary maintenance on healthy equipment and may miss degradation occurring between inspections, such as crack propagation. Even optimized, the preventive maintenance causes avoidable downtime without actually reflecting the real health of the asset (Li et al., 2020). Predictive maintenance aims to overcome these limitations by forecasting equipment failures, optimizing maintenance schedules, and minimizing life-cycle costs. Building a digital twin is a powerful tool in this approach, as this enables real-time monitoring and supports decision-making, thereby enhancing maintenance efficiency.

Following this introduction, we present the motivations for developing a Digital Twin (DT) of an hydraulic turbine and explain why we have chosen to study a simplified nonlinear vibrating cantilever beam with a focus on parameter estimation. Lastly, we describe the thesis organization.

1.1 Motivations

1.1.1 Digital twinning for predictive maintenance in hydropower

In hydropower plants, predicting turbine failures by accurately assessing the current state of equipment is fundamental for optimizing maintenance scheduling, minimizing downtime, and reducing operational costs. Industry 4.0 transforms many sectors, such as energy, aerospace, and manufacturing, by driving the development of advanced digital tools. Digital twins stand out for their powerful predictive capabilities, enabling intelligent decision-making. A DT is a dynamic virtual representation that continuously synchronizes with its physical counterpart by integrating real-time sensor data and advanced simulations, supporting actionable insights and anticipating future system behaviors. Despite variations in definition across sources (Wright and Davidson, 2020), the digital twin concept generally integrates three primary elements (Liang et al., 2025). The physical asset serves as the source for data. The digital model captures and replicates the relevant physical behaviors and system responses. Lastly, an ongoing data flow connects the physical and virtual components. With this continuous flow of information and data, the digital model continuously tracks the evaluation of the asset's performance. In a two-way or closed-loop DT, the model not only receives updates from the physical asset, but also actively communicates back to adapt the asset's operating conditions. With integrated decision-making tools, the DT autonomously determine optimal actions to enhance performance or mitigate issues (Arthur et al., 2020; McClellan et al., 2022). A one-way digital twin process, also known as a digital shadow, involves data flowing from the physical asset to the digital model only (Bergs et al., 2021).

Digital twin technology for predictive maintenance in hydroelectricity is still emerging and lacks fully validated implementations. Hydro-Québec is developing this technology and has already applied it to a turbine speed governor for anomaly detection (Giroux et al., 2023). This project is part of a broader initiative to create comprehensive DT of hydro-turbines, combining real-time sensor data with physics-based models to enable accurate, real-time monitoring and forecasting of turbine health.

1.1.2 Hybrid modeling and parameter estimation in digital twins

There are three primary approaches to developing the digital model inside a DT (Tidriri et al., 2016; Jimenez et al., 2020). Data-driven models combine large volumes of sensor data with machine learning techniques to predict and analyze system performance. While they can be easy to build, their accuracy depends on having enough good-quality data, and scaling them can be challenging. The opposite approach is model-based or knowledge-

driven, relying on engineering principles and physical laws to simulate system behavior. While these models enable accurate simulations, they may require considerable development and calibration effort. Finally hybrid models integrate both approaches, combining physics-based understanding with data-derived insights to enhance accuracy and adaptability (Liang et al., 2025).

One important aspect of building an accurate hybrid digital model is the estimation of system states and parameters, which involves solving inverse problems. This process allows the DT to capture and monitor critical variables that cannot be directly measured by sensors, such as bearing coefficients, to assess the actual state of the system. Kalman Filtering Techniques (KTF) combines physics-based equations with data and enables this joint states and parameters estimation process, even with noisy and incomplete information (Ghorbani and Cha, 2018). Being white-box modeling methods, Kalman filters offer significant advantages over black-box artificial intelligence techniques by providing transparency and clear insight into how the model operates. This approach facilitates building hybrid models that combine mathematical modeling with real data. State estimation through KFT also enables virtual sensing that can reduce sensor numbers or feed data-driven models with enhanced data.

In this work, we apply a the Cubature Kalman Filter (CKF) to estimate unknown states and parameters of a cantilever beam system with the aim of contributing to the development of a digital twin for hydroelectric turbines.

1.1.3 The nonlinear cantilever beam as a simplified experimental system

In rotating machinery, such as the shaft line of a hydraulic turbine, the bearings, are critical components (Adams, 2001). The reaction forces developed within the bearings provide essential information about their mechanical condition and are key indicators to assess operational health (Nässelqvist et al., 2013). Effective health monitoring of bearings requires the estimation of their internal reaction forces, which depend on specific parameters. In the context of building a DT, the vibration behavior of the bearings must be continuously monitored to predict damage and ensure the turbine's integrity. However, directly installing sensors inside an operating hydraulic turbine, to develop a system identification tool, is challenging due to its structural complexity, large scale, and operational constraints. This motivates the development of a simplified system, to reproduce and study the dynamic behavior of the shaft line and its bearings, under controlled conditions.

We simplify the shaft line of a hydraulic turbine, composed of the rotating shaft and its supporting bearings, in a setup that will serves to develop and validate parameter estimation methods for DT applications. At low rotational speeds, the centrifugal and gyroscopic effects

are negligible, allowing the shaft to be approximated as a cantilevered beam. The bearings can be represented as a nonlinear boundary condition at the beam's free end. Therefore, to reflect the vibrating behavior of a turbine shaft line, we choose a nonlinear vibrating cantilever beam as a smaller, simpler, and more cost-effective experimental framework. At first glance, the cantilever beam appears straightforward; however, by adding springs to its free end, it exhibits rich nonlinear dynamics, including nonlinear resonances, bifurcations, jump phenomena, and even chaotic behavior at high vibration amplitudes (Shaw et al., 2016). The cantilever beam setup provides a controlled laboratory environment where tests can be conducted quickly and reliably, and where data acquisition is easier to implement. Acceleration measurements from accelerometers are fundamental for monitoring vibrating systems (Adams, 2001). These sensors provide direct, high-fidelity vibration data essential for creating accurate digital twins of turbine shafts. In the cantilever beam experimental setup, accelerometers measure the beam's vibration response. Exciting the cantilever beam with a modal shaker allows for the investigation of its dynamic behavior across a wide range of excitation scenarios. This setup enables testing with various input signals, including single- and multi-frequency excitations, and across a broad range of frequencies, to replicate the operational conditions of a turbine shaft effectively.

In order to best approximate real-world conditions and support the creation of a reliable DT for turbine health monitoring, the nonlinear cantilevered beam model and accelerometer sensor data are integrated into the CKF to estimate hidden parameters. This method allows us to tackle inverse problems by estimating unknown parameters of a continuous vibrating system, analogous to identifying parameters related to bearing damage in hydraulic turbines.

1.2 Thesis goals and organization

In this thesis, we present the work carried out to solve inverse problem and estimate parameters on a cantilever beam experimental setup, representing a key step toward building a digital twin of a hydraulic turbine.

Figure 1.1 draws a parallel between the shaft line of a hydraulic turbine and the simplified experimental setup, which serves as a foundation to develop and test methods for the DT framework. The nonlinear cantilever beam is excited by a modal shaker under controlled conditions, while an accelerometer and a force sensor collect response data. The CKF combines these experimental measurements, with the known physical model of the beam, to estimate both the dynamic states and the nonlinear stiffness of the spring-boundary condition. This system identification strategy forms an essential part of the broader digital twin framework envisioned by Hydro-Québec, supporting real-time parameter tracking and decision-making.

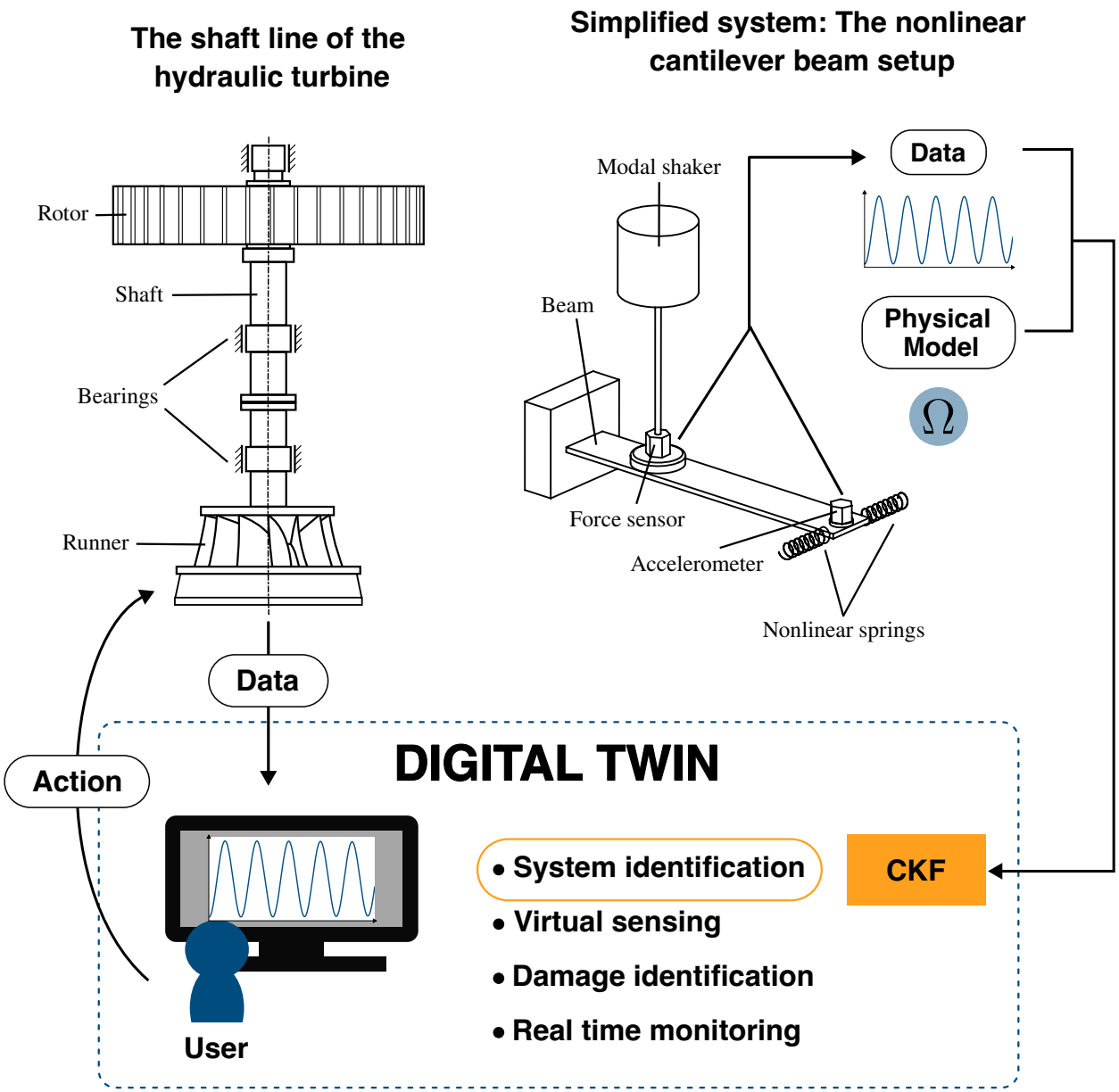

Figure 1.1 **Schematic of the digital twin framework highlighting the specific cantilever beam system developed and analyzed to achieve system identification with the Cubature Kalman Filter (CKF)**

Based on the CKF results, users receive information about the estimated system parameters and can then adjust the actual operating conditions of the physical asset accordingly.

In order to solve the inverse problem with the CKF, it is first necessary to develop a reliable physical model of the experimental setup and ensure the acquisition of high-quality data. The simplified linear cantilever beam represents the healthy state of the vibrating shaft line of a hydraulic turbine. The developed mathematical model describing the beam's dynamic behavior is adjusted to accurately reproduce the linear response of the beam. When operating, especially under off-design conditions, the turbine's bearings begin to deteriorate, and their coefficients evolves. To reproduce this behavior in the simplified test rig, a nonlinear boundary condition is introduced through a spring system. Then, the objective is to estimate the corresponding unknown parameters, the linear and nonlinear stiffness coefficients, with the CKF.

After this first introduction chapter, the thesis is structured as follows: Chapter 2 reviews the relevant literature on Kalman filtering techniques, especially for parameter estimation, on beams excited by a modal shaker and Duffing oscillator as a representative model for nonlinear vibrating systems. Chapter 3 synthesizes the literature review and outlines the objectives of the present study. Chapter 4 describes how to obtain clean experimental data and establish an accurate system model, highlighting the essential preliminary steps before applying Kalman filtering techniques. This chapter details the experimental setup, the experimental quantification of spring stiffness, the mathematical modeling of the nonlinear cantilevered beam, and the comparison between the model and the experimental data. Chapter 5 focuses on the implementation of the CKF for joint state and parameters estimation, with results obtained for both simulated and experimental cases. Finally, Chapter 6 summarizes the key findings, discusses the limitations of the current work, and suggests directions for future research.

CHAPTER 2 LITERATURE REVIEW

This literature review begins by introducing the principles of Kalman filtering, starting with the linear Kalman filter and progressing toward the Cubature Kalman Filter (CKF), which extends the approach to nonlinear systems. The discussion then focuses on the application of these filters to parameter estimation. The second part of the review examines the studied experimental setup, emphasizing the specific characteristics of excitation with a modal shaker. Finally, the literature review presents key concepts from modal analysis and the Duffing oscillator that are relevant to this work.

2.1 Kalman filtering :

The initial formulation of the Linear Kalman Filter (LKF) was developed to estimate the states, position and velocity, of a dynamic system under a Gaussian noise assumption. Until then, the Wiener filter could only handle linear, time-invariant systems with stationary noise and processes the entire data set at once. This made it problematic to estimate the response of time-varying systems with noisy measurements (Kalman and Bucy, 1961). The LKF, developed by Kalman (1960), relies on a state-space formulation in order to solve Wiener problem. All the Kalman Filtering Techniques (KFT) are based on a prediction step and an update step. The algorithm iterates while it receives a new measurement from the system which enables real-time application of Kalman filtering.

2.1.1 The linear Kalman filter

The linear Kalman filter is based on a discrete-time state-space model and estimates the system state vector $\mathbf{x}$, along with its associated uncertainty, described by the covariance matrix $\mathbf{P}$. The LKF is a model-based estimation technique that recursively incorporates measurements ($\mathbf{y}$) to refine state estimates and reduce uncertainty. System dynamics are captured by the transition matrix $\mathbf{F}$. The relationship between the system state and the observed measurements is defined by the measurement matrix $\mathbf{H}$ and enables the filter to predict the measurement vector $\hat{\mathbf{y}}$.

The current system state vector $\mathbf{x}_k$ and the measurement vector $\hat{\mathbf{y}}_k$ are both modeled as linear stochastic processes. The equations are written as (Ghorbani, 2021):

$$\mathbf{x}_k = \mathbf{F}_k \mathbf{x}_{k-1} + \mathbf{v}_k, \quad \mathbf{v}_k \sim \mathcal{N}(0, \mathbf{Q}) \tag{2.1}$$

$$\hat{\mathbf{y}}_k = \mathbf{H}_k \mathbf{x}_k + \mathbf{w}_k, \quad \mathbf{w}_k \sim \mathcal{N}(0, \mathbf{R}). \tag{2.2}$$

The predicted state $\mathbf{x}_k$ is obtained knowing the previous state $\mathbf{x}_{k-1}$ and the discrete transition matrix $\mathbf{F}_k$. The process noise $\mathbf{v}_k$ and measurement noise $\mathbf{w}_k$ are both modeled as zero-mean Gaussian noise, characterized by the process covariance $\mathbf{Q}$, and measurement covariance $\mathbf{R}$, respectively. Given the predicted state $\mathbf{x}_k$, the LFK predicts the measurement $\hat{\mathbf{y}}_k$ thanks to the discrete measurement matrix $\mathbf{H}_k$. Equations (2.1) and (2.2) are the basis of the linear Kalman filter algorithm (Algorithm 1).

Algorithm 1: Linear Kalman filter algorithm

Data: Sensor measurement $\mathbf{y}$ with a time step Δt, transition matrix $\mathbf{F}$, measurement matrix $\mathbf{H}$

Result: Estimated state $\mathbf{x}_k$ and state covariance $\mathbf{P}_k$ for all time step k

1 **Initialize:** Initial state $\mathbf{x}_0$ and initial covariance matrix $\mathbf{P}_0$

2 **Set:** Process noise covariance matrix $\mathbf{Q}$ and measurement noise covariance matrix $\mathbf{R}$

for $k = 1$ **to** $\frac{t_{max}}{\Delta t}$ **do**

3 $\hat{\mathbf{x}}_{k|k-1} = \mathbf{F}_k \mathbf{x}_{k-1}$

4 $\mathbf{P}_{k|k-1} = \mathbf{F}_k \mathbf{P}_{k-1} \mathbf{F}_k^\top + \mathbf{Q}$

5 $\hat{\mathbf{y}}_k = \mathbf{H}_k \hat{\mathbf{x}}_{k|k-1}$

6 $\mathbf{K}_k = \mathbf{P}_{k|k-1} \mathbf{H}_k^\top (\mathbf{H}_k \mathbf{P}_{k|k-1} \mathbf{H}_k^\top + \mathbf{R})^{-1}$

7 $\mathbf{x}_k = \hat{\mathbf{x}}_{k|k-1} + \mathbf{K}_k (\mathbf{y}_k - \hat{\mathbf{y}}_k)$

8 $\mathbf{P}_k = (\mathbf{I} - \mathbf{K}_k \mathbf{H}_k) \mathbf{P}_{k|k-1}$

During the prediction step, Algorithm 1 integrates the governing equations of the system with the transition matrix and predicts the next state vector $\hat{\mathbf{x}}$ and its covariance matrix $\mathbf{P}$ at lines 3 and 4. This matrix represents how uncertain the filter is about each element of the predicted state. The filter also predicts the estimated measurement vector $\hat{\mathbf{y}}$ at line 5. Then during the update step the filter computes the Kalman gain $\mathbf{K}$ at line 6. $\mathbf{K}$ acts as a weight factor and balances the measurement versus the predicted state for the update of the state and covariance matrix at lines 7 and 8.

In the present LKF formulation, the Gaussian assumption is made meaning that all the sources of uncertainty in the system: the process noise, the measurement noise and the initial state, are described by Gaussian probability distributions and only depend on their second order statistics (mean and covariance). This assumption regularizes the estimation and allows the filter to represent the estimated and predicted states only with their covariance. Then the filter provides the best possible solution by minimizing the covariance without overfitting noisy data. The algorithm needs a prior knowledge of the initial state $\mathbf{x}_0$, initial state

covariance matrix $\mathbf{P}_0$, measurement covariance matrix $\mathbf{R}$ and process covariance matrix $\mathbf{Q}$. The initial state covariance matrix is diagonal and describes the confidence in the initial state vector. The measurement and process covariance matrices quantify the uncertainty associated with the sensor measurements and in the system model, respectively.

The linear Kalman filter is widely applied for state estimation in control, navigation, signal processing in real time, robotics to position a robot or to track a target. However the LKF is only applicable to system described by a linear model and with size-limited state vectors (Afshari et al., 2017; Khodarahmi and Maihami, 2023).

2.1.2 Kalman filter for nonlinear systems

To overcome the limitations of the LKF, Hoshiya and Saito (1984) developed the Extended Kalman Filter (EKF), which accommodates nonlinear models and measurements. The EKF linearize locally the nonlinear model (transition and measurement functions) with first order Taylor expansion. However, computing Jacobian matrices at each iteration leads to linearization errors and an increased risk of divergence. This calculation is also not trivial for all applications and is often difficult to implement. (Julier and Uhlmann, 1997, 2004; Khodarahmi and Maihami, 2023). Because of linearization errors, the EFK also fails to estimate the states in highly nonlinear system or those described by high number of independent coordinates (Romanenko and Castro, 2004; Wu and Smyth, 2007; Ghorbani, 2021).

To avoid Jacobian approximation, the Unscented Kalman Filter (UKF) was developed by Julier et al. (1995). The UKF is derivative-free and doesn't approximate directly the nonlinear function that model the system. Instead, it computes a finite set of points called sigma points, to approximate the Gaussian distribution of the system's state (mean and covariance). The sigma points are chosen following a deterministic rule: the unscented transform (Julier and Uhlmann, 1997). The sigma points are distributed around the mean and they reflects the spread (covariance) of the state. Then, the filter applies the nonlinear transient $\mathbf{f}$ and measurement $\mathbf{h}$ functions to each sigma point individually. The transformed sigma points are weighted and recombined to estimate the new means and covariances of the states. Sigma point based Kalman filters, sample and recombine key points to estimate the mean and covariance of the states, by numerically integrating the nonlinear system's governing equations, rather than relying on a linear approximation as with the EKF.

After the UKF, other Sigma points based Kalman filter were developed, like the Gauss-Hermite filter, the quadrature Kalman filter or the Cubature Kalman Filter (CKF) (Afshari et al., 2017; Khodarahmi and Maihami, 2023). Those filters choose different sets of weights and points to evaluate the nonlinear functions and obtain higher accuracy in the estimation of

the states. For example Ghorbani and Cha (2018) combine the sigma points of the UKF and CKF and perform the identification of 10 degree of freedom noisy systems with a better accuracy. Menegaz et al. (2015) provide an overview of the principal UKF variants and introduce a systematic framework to mitigate issues arising from these variations such as instability. Each variation of the Kalman filter has its own strengths and ideal use cases. Among these, the cubature Kalman filter developed by Arasaratnam and Haykin (2009) computes $2n$ sigma points and weights with the cubature rule, where n is the length of the state vector. Then the CKF's computational complexity scales linearly with the number of state variables n, balancing accuracy and efficiency. The CKF accommodates a both low and high dimensional ($n \geq 20$) nonlinear dynamical systems (Arasaratnam and Haykin, 2009). Table 2.1 compares the main Kalman filter variants (LKF, EKF, UKF, CKF) presented previously in terms of their system assumptions, nonlinearity treatment, computational structure and advantages and limitations.

2.1.3 The cubature Kalman filter :

Instead of linearizing the nonlinear equations like the EKF, the CKF computes cubature points to approximate the Gaussian mean and covariance of the system's state. The sigma points $\boldsymbol{\chi}$ and weights w are obtained by solving a third degree spherical-radial cubature rule (Arasaratnam and Haykin, 2009) and,

$$\boldsymbol{\chi}_i = \hat{\mathbf{x}} + \mathbf{S} \cdot \boldsymbol{\xi}_i, \quad \text{for } i = 1, 2, \ldots, 2n \tag{2.3}$$

$$w_i = \frac{1}{2n}, \quad \text{for } i = 1, 2, \ldots, 2n \quad , \tag{2.4}$$

where $\hat{\mathbf{x}}$ is the estimation of the state. The vector $\boldsymbol{\xi}_i$ is defined by the following equations, considering $\mathbf{I}_i$ as the i-th column of the identity matrix.

$$\begin{aligned} \boldsymbol{\xi}_i &= \sqrt{n} \times \mathbf{I}_i, \qquad \text{for } i = 1, 2, \ldots, n \\ \boldsymbol{\xi}_i &= -\sqrt{n} \times \mathbf{I}_i, \qquad \text{for } i = n+1, n+2, \ldots, 2n \end{aligned} \tag{2.5}$$

To ensure the stability of the filter and avoid negative uncertainty, the covariance matrix $\mathbf{P}$ is a positive symmetric semi-definite matrix. Then the Cholesky decomposition factorizes $\mathbf{P}$ into $\mathbf{P} = \mathbf{S}\mathbf{S}^\top$, where $\mathbf{S}$ is a lower triangular matrix and correspond to the "square root" of $\mathbf{P}$. Square-rooting a matrix requires precise calculation: tiny numerical error can be amplified leading to inaccurate or unstable results. The Cholesky decomposition is numerically stable and have a better efficiency and computational cost than other techniques like singular value decomposition (SVD) or the LU decomposition especially for large matrices (Arasaratnam

Table 2.1 **Comparison of Kalman filter variants for nonlinear state estimation**

Filter	**System type**	**Nonlinearity treatment**	**Main advantages**	**Main limitations**
Linear Kalman filter (LKF)	Linear dynamics	Strictly linear model	- Closed-form - Well-understood	- Not suitable for nonlinear dynamics or measurements
Extended Kalman filter (EKF)	Weakly nonlinear dynamics	First-order Taylor expansion (Jacobian-based)	- Structurally similar to LKF - Low cost - Widely used	- Requires analytic or numerical Jacobians - Diverge for strong nonlinearities or poor linearization
Unscented Kalman filter (UKF)	Nonlinear dynamics	Propagation of sigma points (unscented transform)	- Captures nonlinearity better than EKF without Jacobians - Often more accurate and robust than EKF	- More parameters to tune - Computational cost increases with state dimension n ($2n+1$ nonlinear function evaluations per step)
Cubature Kalman filter (CKF)	Nonlinear dynamics	Propagation of cubature points (Spherical–radial cubature rule)	- Symmetric cubature points - Good numerical properties for higher dimensional systems	- More expensive than EKF/LKF: number of cubature points scales with state dimension n ($2n$ nonlinear function evaluations per step)

Algorithm 2: Cubature Kalman filter algorithm

Data: Sensor measurement $\mathbf{y}$ with a time step Δt, transition function $\mathbf{f}$, measurement function $\mathbf{h}$

Result: Estimated state $\mathbf{x}_k$ and state covariance $\mathbf{P}_k$ for every time step k

Initialize: Initial state $\mathbf{x}_0$ and initial covariance matrix $\mathbf{P}_0$

Set: Process noise covariance matrix $\mathbf{Q}$ and measurement noise covariance matrix $\mathbf{R}$

for $k = 1$ **to** $\frac{t_{max}}{\Delta t}$ **do**

Evaluate the sigma points with the current state vector:
$\mathbf{S}_{k-1|k-1} = \text{chol}(\mathbf{P}_{k-1|k-1})$
$\boldsymbol{\chi}^{(i)}_{k-1|k-1} = \mathbf{S}_{k-1|k-1}\boldsymbol{\xi}_i + \hat{\mathbf{x}}_{k|k-1} \quad \text{for } i = 1, 2, \ldots, 2n$

Propagate the sigma points through the model: $\boldsymbol{\chi}^{*(i)}_{k|k-1} = \mathbf{f}(\boldsymbol{\chi}^{(i)}_{k-1|k-1})$

Compute the estimated state vector: $\hat{\mathbf{x}}_{k|k-1} = w_i \sum_{i=1}^{2n} \boldsymbol{\chi}^{*(i)}_{k|k-1}$

Compute the associated covariance matrix:
$\mathbf{P}_{k|k-1} = w_i \sum_{i=1}^{2n} \boldsymbol{\chi}^{*(i)}_{k|k-1}\boldsymbol{\chi}^{*(i)\top}_{k|k-1} - \hat{\mathbf{x}}_{k|k-1}\hat{\mathbf{x}}^{\top}_{k|k-1} + \mathbf{Q}_{k-1}$

Evaluate the new sigma points with the estimated state vector:
$\mathbf{S}_{k|k-1} = \text{chol}(\mathbf{P}_{k|k-1}) \quad ; \quad \boldsymbol{\chi}^{(i)}_{k|k-1} = \mathbf{S}_{k|k-1}\boldsymbol{\xi}_i + \hat{\mathbf{x}}_{k|k-1} \quad \text{for } i = 1, 2, \ldots, 2n$

Propagate the sigma points through the measurement model: $\boldsymbol{\Upsilon}^{(i)}_{k|k-1} = \mathbf{h}(\boldsymbol{\chi}^{(i)}_{k|k-1})$

Compute the predicted measurement vector: $\hat{\mathbf{y}}_{k|k-1} = w_i \sum_{i=1}^{2n} \boldsymbol{\Upsilon}^{(i)}_{k|k-1}$

Compute the innovation covariance matrix:
$P^{YY}_{k|k-1} = w_i \sum_{i=1}^{2n} \boldsymbol{\Upsilon}^{(i)}_{k|k-1}\boldsymbol{\Upsilon}^{(i)\top}_{k|k-1} - \hat{\mathbf{y}}_{k|k-1}\hat{\mathbf{y}}^{\top}_{k|k-1} + \mathbf{R}_k$

Compute the cross covariance matrix:
$\mathbf{P}^{XY}_{k|k-1} = w_i \sum_{i=1}^{2n} \boldsymbol{\chi}^{(i)}_{k|k-1}\boldsymbol{\Upsilon}^{(i)\top}_{k|k-1} - \hat{\mathbf{x}}_{k|k-1}\hat{\mathbf{y}}^{\top}_{k|k-1}$

Calculate the Kalman gain: $\mathbf{K}_k = \mathbf{P}^{XY}_{k|k-1}(\mathbf{P}^{YY}_{k|k-1})^{-1}$

Update the predicted state vector: $\hat{\mathbf{x}}_{k|k} = \hat{\mathbf{x}}_{k|k-1} + \mathbf{K}_k(\mathbf{y}_k - \hat{\mathbf{y}}_{k|k-1})$

Update the state covariance matrix: $\mathbf{P}_{k|k} = \mathbf{P}_{k|k-1} - \mathbf{K}_k\mathbf{P}^{YY}_{k|k-1}\mathbf{K}^{\top}_k$

and Haykin, 2009).

In practice, because of sensitive numerical operation like square-rooting, matrix inversion or subtraction, the covariance matrix often loses its positive semi-definiteness which impede the filter to continue running. To avoid these issues Tian et al. (2022) compute the sigma points of the CKF with other decomposition methods than Cholesky and compare them. With the other methods they can handle non positive definite covariance matrix. Arasaratnam and Haykin (2009) also present a square root version of the CKF (SCKF) which improve the numerical accuracy. Kang et al. (2022) demonstrate the efficiency of the SCKF for the joint estimation of states and time varying stiffness and damping of a journal bearing. The SCKF considers directly the square root of the covariance matrix and computes the Kalman gain with least squares method to avoid square rooting and matrix inversion. However this square root version increases the computational cost and implementation complexity.

We apply the CKF to a nonlinear dynamic system with Gaussian noise. The measurement $\mathbf{f}$ and transient $\mathbf{h}$ nonlinear functions have the same meaning as the transition matrix $\mathbf{F}_k$ and the measurement matrix $\mathbf{H}_k$ for the LKF, respectively. Like the linear case, the cubature Kalman filter presented algorithm 2 operates in two main steps: the time and measurement prediction from lines 3 to 11 and the measurement update from lines 12 to 14. Unlike the UKF, the CKF considers two distinct sets of sigma points: one for state prediction and another for measurement prediction. The CKF iterates over time and applies the prediction and the covariance of the previous step as the prior knowledge for the next cycle. The filter continuously refines its estimations by incorporating new measurements.

2.1.4 Kalman filter with adaptive covariance and parameter tuning

Effective parameter tuning is a challenging issue with Kalman filtering (Akhlaghi et al., 2017). The process noise covariance matrix $\mathbf{Q}$ and measurement noise covariance matrix $\mathbf{R}$ must be set to reflect process and measurement uncertainties. With accurate tuning the filter balances trust between model predictions and new measurements. A standard Kalman filter assumes fixed $\mathbf{Q}$ and $\mathbf{R}$ matrices. If in reality these matrices must change over time to accurately reflect the system's uncertainties, but the filter keeps them fixed, then the filter's estimates are no longer guaranteed to be statistically optimal. As a result, state and parameter estimates may become inaccurate or systematically biased.

In real-world engineering problems, the statistical properties of process and measurement noise are often time-varying, uncertain, or difficult to model precisely. Greś et al. (2025) provide an efficient method for estimating $\mathbf{Q}$ and $\mathbf{R}$, and get accurate virtual sensing data from a linear Kalman filter. On the other hand, adaptive Kalman filter adjusts the values of $\mathbf{Q}$

and $\mathbf{R}$ at each iteration. Guo and Zhao (2022) formulate an adaptive CKF to improve target tracking. Akhlaghi et al. (2017) developed an Extended Kalman filter, in which a forgetting factor α updates the covariance matrices $\mathbf{Q}_k$ and $\mathbf{R}_k$ by blending recent innovation (difference between predicted $\hat{\mathbf{y}}_{k+1}$ and actual measurement $\mathbf{y}_{k+1}$) with previous covariance values. The forgetting factors α_Q and α_R take values between 0 and 1, and act as relaxation factors that control the weighting of past observations.

Ghorbani et al. (2025) and Dollon et al. (2025) adapted the idea of Akhlaghi et al. (2017) to the UKF algorithm and defined the adaptive covariance matrices as:

$$\mathbf{Q}_{k+1} = \alpha_Q \mathbf{Q}_k + (1-\alpha_Q)(\mathbf{K}_{k+1}(\mathbf{y}_{k+1} - \hat{\mathbf{y}}_{k+1})(\mathbf{K}_{k+1}(\mathbf{y}_{k+1} - \hat{\mathbf{y}}_{k+1}))^\top \tag{2.6}$$

$$\mathbf{R}_{k+1} = \alpha_R \mathbf{R}_k + (1-\alpha_R)((\mathbf{y}_{k+1} - \hat{\mathbf{y}}_{k+1})(\mathbf{y}_{k+1} - \hat{\mathbf{y}}_{k+1})^\top + \mathbf{P}^{YY}_{k+1})^\top, \tag{2.7}$$

where $\mathbf{P}^{YY}_{k+1}$ is the innovation covariance (Algorithm 2, line 10). Equations (2.6) and (2.7) are included in Algorithm 2 at the end of the iteration loop after line 14. Although this adaptive procedure improves the estimation of the statistical properties of noise, it introduces more parameter to tune: the forgetting factors (α_Q and α_R) are added alongside the initial noise properties ($\mathbf{Q}_0$ and $\mathbf{R}_0$).

Inaccurate tuning leads to divergence or unreliable results. In practice, users adjust these parameters with a trial-and-error approach. While straightforward, trial-and-error is time consuming and may not guarantee the best parameter selection, especially for complex systems. Chen et al. (2018) and Scardua and Da Cruz (2017) illustrate, among many others, the need for tuning and propose optimization methods based on minimizing the error between estimated states and measurement data. However, in its initial formulation, the Kalman filter already minimize the mean square error between the states and the data so these methods present redundancy. Instead Ghorbani et al. (2025) propose an optimization process based on a physics-aware loss function. Minimizing this loss function ensures that the states estimated by the Kalman filter are consistent with the underlying physical model. In their work, the black-box optimizer NOMAD of Audet et al. (2021) repeatedly runs the Kalman filter within an optimization loop to search for the optimal set of initial covariance matrices and forgetting factors. Dollon et al. (2025) apply this framework to estimate simultaneously unknown inputs, system states and unknown parameters of hydrodynamic bearings with an adaptive UKF.

2.1.5 Parameter estimation with Kalman filtering techniques

System identification is the starting point in many engineering applications and especially to build a digital twin for health monitoring. It relies on the mathematical modeling of the behavior of a dynamical system from observed data. In such model, not all the parameters are known or easy to estimate. For nonlinear systems like a hydraulic turbine, damping, bearing coefficients, imbalance masses or nonlinear stiffness coefficients are unmeasurable directly on the system. However, estimating these unknown parameters and tracking their rate of change is a way to identify damage (Dollon et al., 2025; Tripura et al., 2020). A wide range of techniques have been developed to suit specific contexts. Classical algorithms such as ordinary least squares regression or maximum likelihood estimation determine the best-fit values between the measured system response and the physical model by minimizing a cost function. While these approaches are effective under ideal conditions, they are sensitive to measurement noise and outliers. Inverse problems like parameter estimation are particularly well-suited to Bayesian techniques because they treat parameters as random variables with associated probability , enabling also the quantification of the uncertainty.

Within the Bayesian framework, the Kalman filter and its nonlinear extensions stand out as one of the most effective methods for state and parameter estimation, offering distinct advantages over other techniques. Operating recursively in real time, they combine predictions from a physical model with noisy measurements to produce optimal estimates under a Gaussian assumption. Unlike many traditional Bayesian or non-Bayesian approaches, KFT that rely on batch processing and require storing the full measurement history, Kalman filters update estimates with only the current state and latest observation, making them both computationally efficient and well suited for real-time applications. They are also advantageous for time-varying systems, as the estimates as they can adaptively update estimates as new data arrive. Chatzi and Smyth (2009) and Wu and Smyth (2007) show that KFT are a valuable tool for parameter estimation for nonlinear system. In particular, Chatzi and Smyth (2009) explore the advantages of the derivative free UKF over the EKF and the particle filter. Although the particle filter handles non Gaussian noise, it is computationally expensive because it requires a large number of particles to accurately represent the distribution in high-dimensional spaces.

The Kalman filter estimates simultaneously both the system states and the unknown parameters. To achieve this joint estimation, we extend the original state vector $\mathbf{x}_k$ with a vector of unknown parameters θ_k and create the following augmented state space vector,

$$\mathbf{z}_k = \begin{bmatrix} \mathbf{x}_k \\ \boldsymbol{\theta}_k \end{bmatrix}. \tag{2.8}$$

The process noise covariance matrix $\mathbf{Q}$ and the covariance matrix $\mathbf{P}$ must also be expanded to accommodate the additional parameters. This increases the dimensionality of the state-space representation. Moreover, even if the underlying system model is linear, the interaction between time-invariant parameters and time-varying original states introduces nonlinearities into the augmented system dynamics. Nonlinear Kalman filter variants must be employed for effective joint estimation (Chatzi and Smyth, 2009; Kontoroupi and Smyth, 2016; Ghorbani and Cha, 2018). The CKF in particular, offers a better accuracy and computational efficiency than the UKF when dealing with high-dimensional, nonlinear systems, making it a strong choice for parameter estimation. Moreover even with smaller systems CKF is slightly faster than the UKF as demonstrated by Garcia et al. (2019). They compare the performance of CKF, UKF and EKF for joint estimation of spacecraft orientation and they incorporate real measurements such as the angular velocity. The CKF has been applied for joint estimation of states and parameters, across many fields, such as aerospace (Garcia et al., 2019), hydrology (Sun et al., 2023), electrical engineering (Peng et al., 2019), transportation for fault diagnosis of railway system (Zoljic-Beglerovic et al., 2018), rotating machines (Kang et al., 2022).

The success of Kalman filter-based parameter estimation strongly depends on the proper initialization of the filter. Due to its recursive nature, the filter propagates errors in the initial state vector through the iterations, potentially leading to instability. Furthermore, the results of parameter estimation are highly sensitive to initial conditions. If prior knowledge is far from the truth or the covariance matrix is not properly represented, the filter may converge slowly, produce biased estimates, or even diverge. Therefore, the initial values of the states $\mathbf{x}_0$, parameters $\boldsymbol{\theta}_0$, and their uncertainties $\mathbf{P}_0$, must be chosen correctly. It is particularly important for practical applications, when the physical model does not perfectly describe the experimental behavior of the system.

Kalman filtering techniques are model based methods or white box modeling. Although they integrate experimental data to improve estimations of unmeasured variables or parameters, they are fundamentally constrained by the underlying mathematical model and they cannot deviate significantly from the solution of the model. Then, the accuracy of the results (states or parameter estimation) depends strongly on the accuracy of the underlying model describing the system's physical behavior. If the model is oversimplified, poorly calibrated, or fails to represent key physical phenomena, the state estimates can become biased, unstable, or even divergent. The discrepancies between model predictions and observed data impact even more

the estimated parameters. Moreover, when a Kalman filter estimates a parameter with joint estimation, it solves an inverse problem. These problems are often ill-posed: the solution can lack stability, uniqueness or existence, and small errors in the measurement or modeling can lead to large inaccuracies. Even when the estimated and experimental states match correctly, the final value of the parameter may make no physical sense, as if it converge to a local minimum. This issue worsens in highly nonlinear models, high-dimensional state space model, or when measurements provide insufficient information about the parameters. Additionally, multiple parameter sets can produce similar outputs, leading to non-uniqueness problems. Parameter estimation is also a challenge when the parameters weakly influence the observed outputs, making them difficult to identify. In summary, accurate parameter estimation with KFT relies on accurate modeling of the physical system, careful tuning, and initialization of the filter parameters.

2.2 The nonlinear cantilevered beam setup

The cantilever beam is a classic and fundamental problem in structural dynamics, widely studied, due to its simplicity and practical relevance. Complex systems with intricate boundary conditions are often approximated by beam-like systems, to simplify the study of vibration behavior and structural response. Nonlinearities also have a strong influence on vibration responses, and their impact cannot be neglected in most engineering systems (Butlin et al., 2015; Younesian et al., 2019).

Nonlinear cantilevered beam-like systems are studied in both experimental and simulation perspectives. Sari and Al-Solihat (2025) develop an analytical model for a functionally graded porous cantilever beam with an intermediate spring subjected to a harmonic tip force. They explore how porosity, material gradation, and spring stiffness affect the nonlinear free and forced vibration characteristics of the beam. On the experimental side, Wang et al. (2022) focus on parameter estimation in piezo-electrically excited cantilever beams. Here, they estimate unknown parameters, based on measured data, with adaptive modeling techniques. Beyond modeling, Habtour et al. (2022) develop a nonlinear identification method as a diagnostic tool. They tracks variations in the vibration response and associated parameters, in order to detect early signs of fatigue in a cantilevered beam subjected to large vibration amplitude.

One important focus in the study of nonlinear cantilevered beams is on configurations with special boundary conditions at the free end, particularly the inclusion of cubic springs. While Santo et al. (2020) investigate the impact of this type of boundary condition on system dynamics, others focus on estimating the nonlinear stiffness with the vibration response of

the beam. Sadati et al. (2012) reproduced a nonlinear joint consisting of a cantilevered beam with two perpendicular beams at its tip, which acted as cubic springs. They then identify the nonlinear characteristics of the beam using an optimal equivalent linear frequency response function. With the same system modeling (a cantilevered beam with a cubic spring at its end), Sadeghi and Lotfan (2017) develop a method based on nonlinear system identification and artificial neural networks to estimate the cubic stiffness, even in noisy conditions, with simulated data. Shaw et al. (2016) incorporated a nonlinear spring system at the tip of their cantilevered beam setup to develop a nonlinear experimental test bench with rich dynamics. With this configuration, they tuned the natural frequencies of the structure to induce a 3:1 internal resonance and study the complex vibration responses of the beam, near the first natural frequency. Taghipour et al. (2022) present a nonlinear system identification technique, based on the harmonic balance approach. They consider the same experimental system: a cantilevered beam with perpendicular springs, among other applications. Their method accurately identifies the nonlinear stiffness added by the springs, even when the system exhibits pronounced multi-harmonic responses arising from cubic nonlinearity.

In the configuration studied by Shaw et al. (2016) and Taghipour et al. (2022), two perpendicular springs are attached to the free end of a cantilever beam. The nonlinear behavior in this system stems from the geometry of the springs. The springs, of stiffness k, are initially preloaded so that their length when the beam is at rest, is a, while their free length outside the setup is l_0. At rest, the springs are horizontal and exert no force in the transverse z-axis. As the beam deflects, the displacement at its free end w, causes the springs to incline with an angle θ, generating a restoring force $\overrightarrow{F_r}$, as illustrated in Figure 2.1. The component of this force aligned with the beam's direction of motion is responsible for the nonlinear behavior. Projected onto the vertical axis, this component of the force becomes

$$F_k = k(l - l_0)\sin(\theta). \tag{2.9}$$

The two springs on either side act as parallel springs with the same stiffness, so the total force is doubled. By substituting $\sin(\theta) = w/l$ and $l^2 = a^2 + w^2$ into the equation (2.9), we derive the nonlinear force-displacement relationship for this two springs configuration,

$$P(w) = 2kw\left(1 - \frac{l_0}{\sqrt{a^2 + w^2}}\right). \tag{2.10}$$

This experimental setup is simple enough to be accurately modeled by mathematical equations, yet it exhibits complex vibration responses. This makes it an ideal application for validating and verifying CKF-based parameter estimation method.

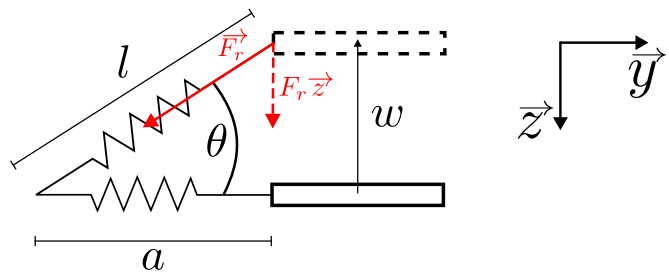

Figure 2.1 **Schematic of nonlinear spring system at the free end of the beam**

2.2.1 Beam excited by a modal shaker

In the experimental studies that have already been presented, the structure under test is frequently excited by a modal shaker (Sadati et al., 2012; Shaw et al., 2016; Taghipour et al., 2022). The modal shaker provides controlled and repeatable excitation, making it ideal for modal analysis and to study nonlinear vibration responses (Ewins, 2000). Unlike impact hammers, which deliver impulsive forces, modal shakers can excite a structure with controlled force across a broad frequency range. This enables detailed analysis of the structure's dynamic response in specific frequency bands, such as resonance regions. A modal shaker can excite the system with various excitation types, including random signals, such as white noise, pseudo-random noise, and periodic noise, for broadband excitation, or with chirp or sine sweep signals to focus on specific frequency ranges (Noël and Kerschen, 2017). Furthermore, harmonic excitation can be applied to investigate nonlinear behavior or resonance phenomena.

Proper mounting of the modal shaker and precise signal piloting strategy are essential to ensure accurate excitation and reliable measurement during beam testing (Mayes and Gomez, 2006). Typically, a stinger connects the structure under test to the modal shaker. The stinger is a critical component designed to transmit force while minimizing unwanted loads. It must be axially stiff, to efficiently transmit the excitation force, and laterally flexible to prevent side loads and moments that could distort the measurement or damage the equipment. The stinger is usually composed of a material that exhibits both axial rigidity and lateral flexibility, such as nylon rods. Several researchers, including Cloutier et al. (2009) and, Peres and Bono (2011), have studied the optimal arrangement for attaching the shaker, leading to the establishment of guidelines. However, the shaker setup depends greatly on the structure under test, and on the frequency ranges excited. A force sensor, often piezoelectric, attached between the stinger and the structure, measure the input force.

2.2.2 Beam shaker interactions

When a system, like a beam, is excited by a modal shaker, complex interactions arise between the shaker, stinger, and structure, and can influence experimental results. Proper alignment of the entire assembly (shaker, stinger, force sensor, and beam) is crucial to ensure axial force transmission, avoid unmeasured forces and limit interactions between the structure under test, and the shaker. However, even with careful use of a stinger to minimize the transfer of unwanted rotational forces to the structure, it does not eliminate all interaction effects, arising from the dynamic excitation and the compliant mounting (Mohammadali and Ahmadian, 2016). The shaker-stinger assembly changes the way a structure responds to excitation because both components introduce their own mechanical characteristics (stiffness, damping) into the test setup, altering the boundary conditions and dynamic response of the structure. On the other hand, the structure motion directly influences the force that the shaker delivers to the system. The beam does not simply absorb the input force, it also reacts dynamically and pushes back on the shaker. This phenomenon generates reactive forces that interact with the shaker itself and alter the transmitted excitation force. Zhang et al. (2022) analytically model the coupled beam-shaker-structure system, and develop an analytical expression of the excitation force. They also validate their model by comparing the results with experimental data.

The impact of beam-shaker coupling on the excitation force, is accentuated in the resonance region, where the system exhibits greater vibration amplitude. At resonance frequencies, even when the shaker should impose a purely sinusoidal drive, the transmitted force becomes distorted and multi-harmonic, and loses its expected harmonic character (Figure 2.2). Force dropout also occurs: the measured force drops sharply, diverging from the steady sinusoidal excitation applied by the shaker (Varoto and de Oliveira, 2002; Gabos and Dombovari, 2025). In linear systems, force dropout may not pose significant issues; however, in nonlinear systems, the amplitude of excitation greatly influences the system's response, making this phenomenon potentially problematic.

The primary goal of using a modal shaker is to excite a structure in a controlled manner. Chirp or swept-sine signals with constant amplitude are often imposed to study the system's dynamic response across a frequency range, assuming that the excitation frequency is swept slowly enough to observe quasi-steady-state responses. This is typically done near resonance, so that only the excitation frequency changes over time. However, it is difficult to maintain an ideal constant excitation force in practice due to beam-shaker interactions and the force dropout at resonance. As a result, the system may be subjected to either insufficient or excessive excitation at certain frequencies, compromising the reliability and

accuracy of the measured dynamic response. Tang et al. (2018) modeled beam-shaker interactions, with a method based on the dynamic stiffness, to understand better of the impacts of these interactions in nonlinear systems. Gabos and Dombovari (2025) propose a control-free method to account for force dropout when analyzing swept frequency response of nonlinear structures. Their approach enables accurate reconstruction of nonlinear frequency response curves without relying on force controllers.

Rather than taking these phenomena into account, Shaw et al. (2016) and Hippold et al. (2022) focused on actively controlling the harmonic content of excitation forces generated by modal shakers, in order to improve the accuracy of testing in nonlinear dynamic systems. By using feedback control strategies on the shaker's input voltage, they successfully isolated the fundamental harmonic, thereby maintaining constant force amplitude and periodicity, and reducing nonlinear force artifacts. While active control of the excitation force harmonics can improve measurement quality in some cases, achieving this often requires specialized controllers and advanced control methodologies.

Beam shaker interactions undeniably influence the accuracy and interpretation of dynamic testing results, particularly for nonlinear structures near resonance frequencies. Therefore, it is important to be aware of these phenomena in order to correctly interpret experimental data.

2.2.3 Modal analysis

When an external dynamic force excites a structure, it response can be expressed as a linear combination of distinct vibration modes. The physical properties (mass, stiffness, damping) and the geometry determine the natural modes of vibrations of a system. Each natural mode is characterized by modal parameters: natural frequency, modal damping and mode shape. Modal analysis is the process of identifying and evaluating these modal parameters in order to understand and describe the dynamic behavior of the system. Understanding the vibrational response through modal analysis is crucial because, at resonance, vibration amplitudes can grow significantly, potentially leading to damage or even failure. With modal analysis, engineer check whether operating conditions overlap with natural frequencies and, if necessary, modify the excitation or alter the system's properties to avoid resonance. Beyond resonance avoidance, one of the central outcomes of modal analysis, is the development of simplified but representative models of structural dynamics.

In this field, several foundational textbooks provide a comprehensive treatment of modal analysis. Ewins (2000), He and Fu (2001), Brandt (2023) and Modak (2023), cover both the theoretical framework and the experimental application of modal analysis techniques. Sev-

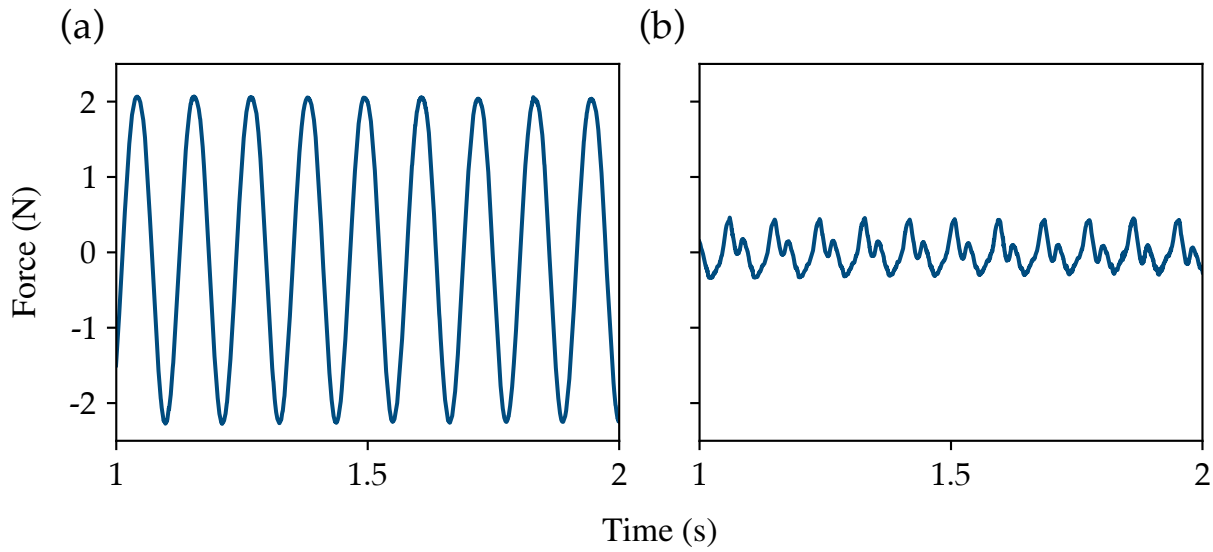

Figure 2.2 **Force sensor measurement when the shaker apply a sinusoidal excitation.** **(a)** Recorded force when the excitation is applied far from the resonant frequency, illustrating reduced beam-shaker interaction. **(b)** Recorded force when the beam system is excited at its resonant frequency, showing strong beam-shaker interaction effects

eral approaches exist for conducting modal analysis, each suited to specific applications and available information. Analytical modal analysis relies on mathematical models to predict a system's dynamic properties. Operational modal analysis is applied when the excitation forces are not measurable, which is often the case in civil engineering structures subjected to ambient loads such as wind or traffic. In contrast, Experimental Modal Analysis (EMA) also known as modal testing, directly measures the system's response under controlled excitation. In this work, we will focus on EMA to identify modal parameters, because it's the standard technique for laboratory and industrial investigations of structural dynamics.

In EMA, a modal shaker or an impact hammer impose a known force to the structure and accelerometers measure the vibration response at different locations. Both the applied force and the vibration response are recorded to compute the Frequency Response Function (FRF). The FRF is a complex-valued function that describes how the structure responds at each frequency and forms the basis for extracting modal parameters. To compute the FRF, it is necessary to convert the time-domain measurements of the acceleration and the force, into the frequency domain with Fourier transform. The FRF is the ratio of the output spectrum (usually acceleration: $\mathbf{A}_{FRF}(\omega)$) to the input spectrum (force: $\mathbf{F}_{FRF}(\omega)$) for each frequency such as:

$$\mathbf{H}_{FRF}(\omega) = \frac{\mathbf{A}_{FRF}(\omega)}{\mathbf{F}_{FRF}(\omega)}. \tag{2.11}$$

To extract the modal parameters from the FRF, it is common practice to consider each mode of vibration independently. Modeling each mode as if it is a simple Single Degree Of Freedom (SDOF) system relies on the assumption that, near a resonance peak, the system's response is mainly influenced by the corresponding mode alone. This assumption is only valid for a linear system, where the principle of superposition is applicable and the modal parameters remain constant regardless of vibration amplitude. The modes must also not interact with each other. Then the SDOF approximation greatly simplifies the analysis by allowing each mode to be treated separately rather than simultaneously.

Within this framework, several methods exist to extract modal parameters from the measured FRFs. These include peak-picking techniques, circle-fit methods, and curve-fitting among other approaches (Ewins, 2000). While peak-picking is straightforward and relies on identifying resonance peaks, it tends to lose accuracy for structures with closely spaced or highly damped modes. Circle-fit methods analyze the FRF's Nyquist plot to estimate modal parameters more reliably. Among these, the curve-fitting method is a precise technique and gives reliable estimates of natural frequency ω_n and modal damping coefficient ζ, even in the presence of noise or closely spaced modes. From the equation of motion for a SDOF damped oscillator with a stiffness k, we get the analytical form of the complex FRF, obtained with the acceleration signal :

$$\mathbf{H}_{FRF}(\omega) = \frac{-\omega^2/K_n}{1-(\frac{\omega}{\omega_n})^2 + 2j\zeta(\frac{\omega}{\omega_n})}. \tag{2.12}$$

Then a least squares method fits the analytical equation (2.12) to the the experimental FRF data around resonance to obtain the modal parameters.

SDOF modal analysis techniques are not suitable for all scenarios. SDOF assumptions are not valid and each mode cannot be considered independently, when modes are too closely spaced or heavily coupled, or when damping is very light. In such cases, it is necessary to analyze the entire FRF data with Multiple Degree Of Freedom (MDOF) methods. More advanced methods, including MDOF curve fitting and time domain methods like the Least Squares Complex Exponential and Stochastic Subspace Identification, handle coupled modes and provide accurate parameter estimation for complex systems (Ewins, 2000). Nonetheless for many practical applications, SDOF based curve fitting provides a reliable and straightforward approach to get a first sufficient estimation of modal parameters.

2.3 Duffing oscillator

The Duffing equation, developed by Duffing (1918), serves as a fundamental model for approximating and analyzing the behavior of a wide range of nonlinear physical oscillatory systems. This equation exhibits in fact different nonlinear phenomena, such as nonlinear resonance, bistability and amplitude jumps, bifurcation, or chaos behavior. In mechanical engineering, Kovacic and Brennan (2011) model the nonlinear response of plates and cables, the motion of nonlinear pendulums; Habtour et al. (2022) and Tang et al. (2018) model respectively large-amplitude vibrations of a cantilevered beam and beam buckling, with Duffing equation.

In the Duffing equation, the nonlinearity comes from the stiffness, which creates a nonlinear restoring force and distinguishes it fundamentally from linear oscillators. This restoring force is composed of a linear stiffness k_L multiplied by displacement x and a nonlinear stiffness k_{NL} multiplied by displacement cubed. Considering $k_L > 0$, the sign of the nonlinear term influences the observed dynamics. If the nonlinear stiffness: k_{NL} is positive, the system becomes stiffer as the displacement increases and exhibits hardening behavior. Conversely, when k_{NL} is negative, the system exhibits a softening behavior (Kovacic and Brennan, 2011; Brennan et al., 2008; Wawrzynski, 2021). In experimental setups where the restoring force manifests a cubic nonlinearity, such as in the study of Sadati et al. (2012), Shaw et al. (2016), or Taghipour et al. (2022), the Duffing oscillator is an effective mathematical framework for analysis and behavior prediction. In addition to stiffness-related terms, the following SDOF Duffing equation incorporates the terms of a classical oscillator with mass m and damping c coefficients:

$$m_d\ddot{x} + c\dot{x} + k_L x + k_{NL}x^3 = f\cos(\omega t), \tag{2.13}$$

where x is the displacement and t is the time. This oscillator is excited by an external harmonic force of amplitude f and frequency w.

All the parameters in Equation (2.13) are constant, then to reduce the number of parameters, facilitate the analysis, and the development of analytical solutions, the Duffing equation is usually studied in non-dimensional form such as

$$y'' + 2\zeta y' + y + \alpha y^3 = \cos(\Omega\tau). \tag{2.14}$$

Among other methods, we apply the dimensionless method of Brennan et al. (2008), and the coefficients become

$$y = \frac{k_L}{f}x, \quad \alpha = \frac{k_{NL}f^2}{k_L^3}, \quad \zeta = \frac{c}{2m_d\omega_0}, \quad \tau = \omega_0 t, \quad \Omega = \frac{\omega}{\omega_0}, \quad \omega_0^2 = \frac{k_L}{m_d}, \tag{2.15}$$

where $(\bullet)' = \frac{\mathrm{d}}{\mathrm{d}\tau}(\bullet)$.

To solve equation (2.14), researchers rely either on analytical methods, that provide a very good understanding of the system's behavior, or on numerical methods, when the equation involves strong nonlinearities, damping, or special external forcing, making analytical solutions impractical. Korsch et al. (2008) solve the equation numerically through time discretization and the implementation of a Runge–Kutta integration procedure. In contrast, analytical methods seek to find exact or approximate solutions in closed form. They are usually applicable under simplifying assumptions, such as weak nonlinearity, or the absence of forcing and damping. He (2006) and Kovacic and Brennan (2011), explain different methods for developing the analytical solution of the Duffing equation, particularly for free or harmonically forced oscillations of the undamped Duffing oscillator. For weakly nonlinear systems where the cubic nonlinearity is small ($\alpha \ll 1$), approximate solutions are easier to derive. In such cases, perturbations methods are commonly employed to obtain analytical expressions. In contrast, for strongly nonlinear systems, finding exact analytical solutions becomes significantly more challenging, and typically involves Jacobi elliptic functions, to capture the nonlinear oscillatory behavior. Adding damping and specific excitation forces complicates the determination of an analytical solution. Ongoing research efforts are therefore devoted to developing approximate methods that can handle, time delays or variable excitation, for example. Moatimid et al. (2023) analyze the effects of time delay on the dynamics of a damped harmonic forced Duffing oscillator, providing accurate approximate solutions. Wawrzynski (2021) highlight the influence of harmonic excitation with variable amplitude and time-dependent disturbances on Duffing-type oscillators behavior. Abohamer et al. (2025) show the diverse dynamical regimes that can arise form the chaotic and stability characteristics of the Duffing oscillator subjected to sinusoidal forcing.

Building on the work of Shaw et al. (2016), our study will focus on beam vibrations with a cubic restoring force in the small-displacement region, excluding chaotic or highly complex nonlinear behavior. Under the assumptions of weak damping and weak nonlinearity, the maximum amplitude response of a Duffing oscillator does not occur only at the linear natural frequency, as it would for a linear system. In addition to the primary resonances (which align with the natural frequency), the system can exhibit secondary, or nonlinear, resonances when the excitation frequency differs from the system's natural frequency. In the case of the Duffing oscillator, superharmonic resonance arises when the system is forced close to one-third of the natural frequency, and subharmonic resonance arises when the system is forced close to three times the natural frequency (Kovacic and Brennan, 2011). In the nonlinear resonance region, key analysis tools include, among others, the frequency response curve, and the backbone curve, which relates natural frequency to oscillation amplitude and characterizes the system's

nonlinear stiffness.

The frequency response curve describes how the steady-state amplitude of oscillations Y varies with the excitation frequency ω, and identifies resonance frequencies and jump phenomena, for both softening and hardening systems (Figure 2.3). Brennan et al. (2008) apply the harmonic balance method to determine the relationship between the frequency ω and the amplitude Y. Assuming a solution of the form $y = Y\cos(\Omega\tau + \phi)$ (with $\Omega = \omega/\omega_0$), to the Duffing equation (2.14) with low damping ($\zeta \ll 1$), and neglecting subharmonics, as we are focusing on primary resonance, we get

$$\left(\frac{3}{4}\alpha Y^2 + (1-\Omega^2)Y\right)^2 + 4\zeta^2\Omega^2 Y^2 = 1, \tag{2.16}$$

and solving for Ω, we obtain

$$\Omega_{1,2} \approx \left(1 + \frac{3}{4}\alpha Y^2 \pm \left(\frac{1}{Y^2} - 4\zeta^2\left(1 + \frac{3}{4}\alpha Y^2\right)\right)^{1/2}\right)^{1/2}. \tag{2.17}$$

Figure 2.3 presents the frequency–amplitude curves near the primary resonance, computed from Equation (2.17), for various values of α, including linear, softening and hardening characteristics. Unlike linear systems, where the amplitude-frequency response yields a single resonance curve, the frequency response for Duffing oscillators exhibits different behavior depending on the sign of the nonlinear coefficient. When $\alpha < 0$, the frequency response curve bends toward lower frequencies as the oscillation amplitude increases, resulting in a softening response. Conversely, $\alpha > 0$ induces a hardening effect and the curve leans toward higher frequencies with increasing amplitude. The larger α is, the more the amplitude peaks shift toward high frequencies. For the same value of $|\alpha|$, the peak vibration amplitude is higher in the softening response compared to the hardening response (Figure 2.3).

Because of the form of Equation (2.16) (cubic polynomial in Y^2), a fix excitation frequency gives, up to three different steady state amplitudes. This multi-valued behavior leads to jump phenomena and bistability near the primary resonance. Considering the hardening system, as the excitation frequency quasi-statically increase, moving rightward along the frequency response curve, the system's response follows the upper branch. Once the frequency reaches the peak amplitude, the upper branch becomes unstable and the system suddenly switches to the lower amplitude branch. This abrupt transition is known as 'jump phenomenon'. Conversely, when the excitation frequency sweeps leftward from high to low frequencies, the amplitude initially follows the lower branch until it reaches a critical point where it jumps up to the upper branch (Figure 2.3). These upward and downward jumps occur at different

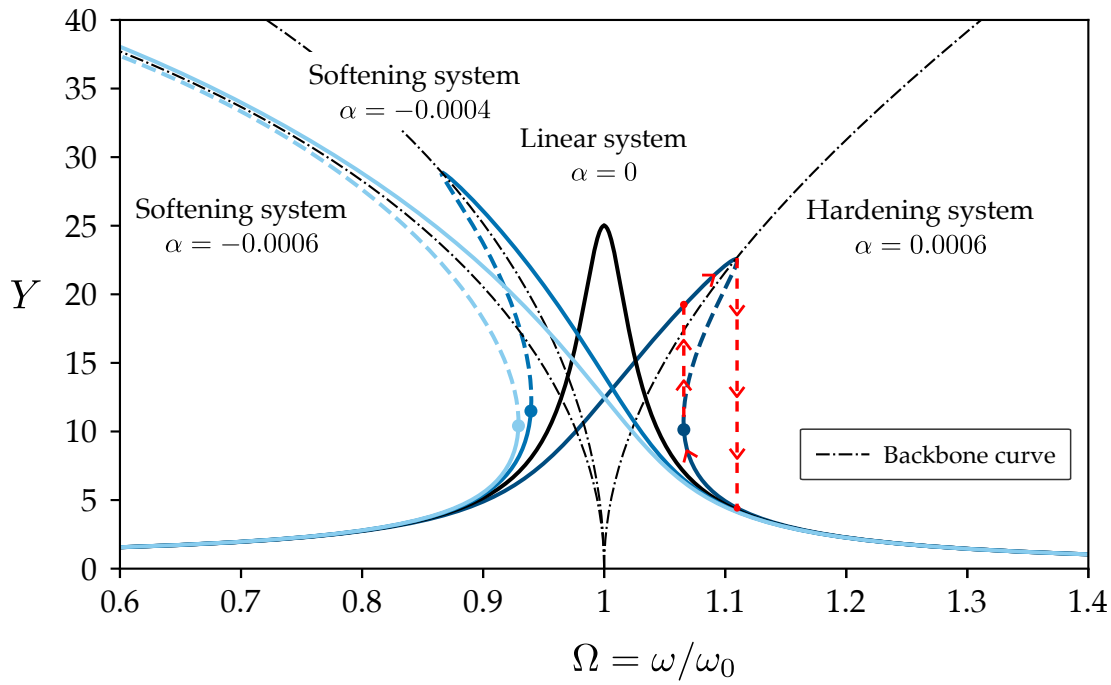

Figure 2.3 **Frequency–amplitude curves near the primary resonance simulated with Eq.**(2.17)**.** Softening ($\alpha = -0.0006$ and $\alpha = -0.0004$); hardening ($\alpha = 0.0006$) an linear ($\alpha = 0$) behavior are plotted. All cases are calculated with $\zeta = 0.02$ and the dashed lines represents the unstable regions. Backbones curves are also plotted with dash-dot lines

frequencies, creating a hysteresis loop. Brennan et al. (2008) developed an analytical solution to determine the amplitudes and corresponding frequencies, at which jump-up and jump-down transitions occur. Physically, it is hard to observe the intermediate solution branch, connecting the two stable branches, because it is unstable and any perturbation drives the system toward one of the stable states. Zhang et al. (2020) developed an experimental method that exploits the dynamics of the electromechanical shaker to measure all branches of the nonlinear system's response, including normally unstable or inaccessible solutions. Both hardening and softening Duffing oscillators exhibit this bistable response near resonance, with jump frequencies.

Backbones curves, given by $\Omega^2_{backbone} = 1 + \frac{3}{4}\alpha Y^2$, are also plotted in Figure 2.3 and show the relationship between the amplitude of vibration and the nonlinear natural frequency of the Duffing oscillator, for free oscillations. Unlike linear systems, the natural frequency depends on the excitation amplitude, due to the system's nonlinear restoring force. For a hardening nonlinearity ($\alpha > 0$), the backbone curve bends to the right, meaning higher amplitudes correspond to higher natural frequencies. Wang and Tang (2022) and Givois et al. (2020) identify key system parameters, including nonlinear stiffness coefficients with

backbones curves in, respectively, an asymmetric single oscillator with combined quadratic and cubic stiffness, and a coupled oscillators exhibiting internal resonance. Backbone curves are also a tool to understand nonlinear experimental systems. Shaw et al. (2016) extracted the backbone curve from the experimental data to analyze how internal resonance induces shifts, bifurcations, and complex interactions in the periodic response.

CHAPTER 3 SYNTHESIS OF THE LITERATURE REVIEW AND REASEARCH OBJECTIVES

3.1 Synthesis of the literature review

The intermittent nature of renewable energies when integrated into the grid results in hydroturbines being operated under off-design conditions, with more frequent start and stop, which increases their wear and need for close monitoring. In this context, a digital twin could continuously monitor the turbine, predict potential damage, and support the optimization of maintenance strategies. The global objective of this project, is to develop and test methods that can be applied to the creation of such a digital twin. We focus on parameter estimation which is an important step of building a digital twin. Without accurate parameters, even the most detailed models fail to replicate real-world behavior. The cubature Kalman filter is a model based technique and can estimate either states and parameters, while incorporating sensor measurements. Directly applying this framework to a real hydraulic turbine and collecting sensor measurements is too complex as a starting point. This study investigates the vibration behavior of the turbine's shaft line, focusing on the identification of nonlinear effects arising from deteriorated bearings. Simplifying the setup by considering a nonlinear cantilever beam provides a more practical entry point, and makes experimental data more accessible. The linear beam represents a healthy hydraulic turbine shaft line, and we build a model to accurately represent its behavior and fit experimental data. Adding nonlinear boundary condition, specifically the spring system, to the setup, simulates deteriorated nonlinear bearings, which are the focus of our identification efforts. Even a simple vibrating beam, when equipped with springs, displays nonlinear dynamics and rich behavior.

The CKF has been successfully applied in the literature to nonlinear systems with many degrees of freedom and high complexity, achieving robust parameter estimation with simulated data. However, applications involving experimental data from nonlinear vibrating systems, such as beams excited by a modal shaker, remain relatively rare. Applying the CKF to estimate unknown parameters from experimental data, aims to validate its effectiveness on real data.

3.2 Research objectives

As highlighted in the summary of the literature review, the central objective of this project is to estimate unknown parameters of a nonlinear vibrating system. We will combine exper-

imental data with a mathematical model inside a cubature Kalman filter to estimate these parameters. This project will lay the foundations for creating a digital twin of a more complex system like hydraulic turbine. We propose the following objectives:

1. **Develop a comprehensive understanding of the cantilevered beam system's physical behavior and acquire clear, high-quality nonlinear experimental data.** Prior to estimating the unknown parameters, it is necessary to characterize the system's dynamics through modal analysis and static force displacement tests. This process involves determining the system's natural frequencies and modal coefficients, as well as confirming the system's nonlinear behavior. Subsequently, we must develop the mathematical model of the system. The estimations from the linear model will be compared with the experimental data to verify that the model accurately captures the key features of the physical system's behavior before introducing the nonlinear boundary condition.

2. **Estimate the unknown parameters of the nonlinear cantilevered beam system with the CKF algorithm.** The CKF predict the behavior of the system with the mathematical model and update the estimated states and parameters with experimental data. For the linear beam, the parameters to be estimated include a point mass and the bending stiffness of the beam. For the nonlinear beam, the aim is to estimate both the linear and nonlinear spring stiffness, which are analogs to the bearing characteristics of a hydraulic turbine shaft line. The CKF is applied on the vibration response of the beam excited with harmonic (single frequency) and chirp (multi-frequency) signals. The algorithm is verified and validated with both simulated and experimental data ensuring its accuracy and reliability in identifying unknown parameters for a mechanical vibrating system.

CHAPTER 4 CHARACTERIZATION OF THE BEAM SETUP

4.1 The experimental setup

We a simple vibrating system: the beam with a complex boundary condition: the spring system. Shaw et al. (2016) originally designed the cantilever beam with springs to intentionally create an internal resonance. We took inspiration from their work to build a nonlinear vibrating beam, which allows collecting data, to estimate unknown parameters. The test bed, presented in Figure 4.1, consists of a steel cantilevered beam of total length $L = 0.513$ m, rigidly clamped between two steel clamping plates at one end. Four bolts tighten the beam in place over a 10 cm length to approximate an ideal clamped boundary condition. Table 4.1 summarizes the key physical parameters and characteristics of the experimental beam.

A uniaxial piezoelectric accelerometer (PCB 352C33) records the vertical acceleration at the free end of the beam. A modal shaker (K2004E01) imposes a force on the beam. The shaker is mounted on a slide to easily change its location and is positioned 8.5 cm away from the fixed end of the beam. After testing, we chose this location because placing the shaker closer to the fixed end limited the excitation amplitude, thereby reducing beam shaker interactions (Figure 4.4). A nylon rod stinger connects the shaker to the beam and a PCB 208C01 piezoelectric force sensor records the excitation force applied by the shaker to the beam. This force sensor is screwed on one hand to the stinger and on the other hand to a magnet. We chose to connect the beam and the shaker with a magnet to ensure contact without any unwanted movement or clearance. The NI-9234 dynamic signal acquisition module measures the vibration signal from the force sensor and the accelerometer. This module is connected to a computer that runs LabVIEW software to record signals with a fixed sampling frequency of 2048 Hz. Excitation signals are also sent to the shaker via LabVIEW. The shaker can impose different types of excitation on the beam, such as sinusoidal, white noise, or sin chirp signals. To control the amplitude of the excitation, we can change the input voltage sent to the shaker with a maximum value of 150 mV. Unlike the approach of Shaw et al. (2016), we don't actively control the amplitude of the excitation force applied to the beam. As a result, interactions between the beam and the shaker can influence the applied force, causing the excitation force to vary with the excitation frequency as shown in the sin chirp force signal in Figure 4.4 (b).

The setup also features two springs attached to the free end of the beam, with their axis perpendicular to the movement of the beam. This arrangement of springs creates a geometric nonlinearity that depends on the no-load spring length l_0, the preloaded length a, the stiffness

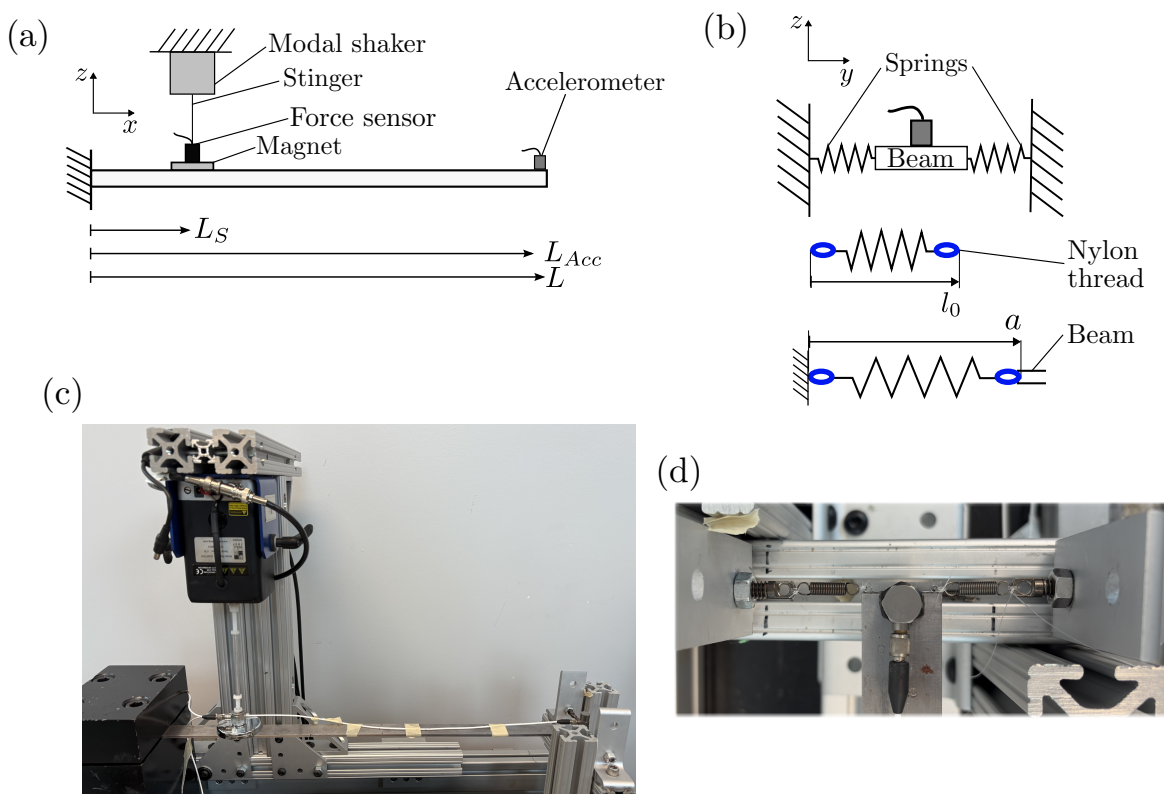

Figure 4.1 **Experimental setup. (a)** Schematic of the beam. **(b)** Schematic of the springs system at the end of the beam, highlighting of the no-load spring length l_0 and the preload length a. **(c)** Global photograph of the experimental setup - the beam measures half a meter. **(d)** Top view photograph of the spring mechanism

Description	Symbol	Value	Unit
Material density	ρ	7850	kg/m^3
Young's modulus	E	210×10^9	Pa
Length of the beam	L	0.513	m
Shaker location	L_S	0.085	m
Accelerometer location	L_{Acc}	0.507	m
Width of the beam	b	0.0257	m
Thickness of the beam	h	0.0033	m
Moment of inertia	I	$bh^3/12$	m^4
Cross section of the beam	A	bh	m^3
Mass per unit length	m	ρA	kg/m
Mass of the magnet and force sensor	m_S	0.115	kg
Mass of the accelerometer	m_{Acc}	0.0081	kg
Initial length of the spring	l_0	0.01905	m
Stiffness of the springs	k	770	N/m

Table 4.1 **Physical parameters of the system**

of each spring k (assuming both springs are the same), and the deflection at the free end of the beam w, as illustrated in Figure 2.1. Then the static force displacement curve P, derived form this configuration (2.10), can be approximated as the sum of a linear stiffness k_L and a cubic stiffness k_{NL}, applying Maclaurin expansion (Shaw et al., 2016),

$$P(w) = k_L w + k_{NL} w^3, \tag{4.1}$$

with,

$$k_L = 2k(1 - \frac{l_0}{a}), \tag{4.2}$$

and,

$$k_{NL} = \frac{k l_0}{a^3}. \tag{4.3}$$

The ratio l_0/a affects the nonlinear stiffness k_{NL}. If $l_0/a = 1$, the springs are not preloaded, k_L is equal to zero, and only the nonlinear stiffness remains. In contrast, when $a \gg l_0$, k_{NL} approaches zero and the system behaves like a linear system. Shaw et al. (2016) studied the response of their beam around the first natural frequency, and with this from of nonlinearity they observed a hardening response.

The value of the half-span of the mechanism a is not easy to measure precisely without installing other sensors. Small variations in this length significantly affect the ratio l_0/a and the estimated values of both linear and non-linear stiffness, as described in Equations (4.2) and (4.3). An alternative experimental approach presented in Section 4.1.1, quantifies approximately k_L and k_{NL}. We selected two identical springs with a stiffness $k = 770$ N/m and a free length of 19.05 mm. The no-load spring length $l_0 = 23.55$ mm is the sum of the free length of the spring and the nylon fasteners. Unlike Shaw et al. (2016), our objective is not to achieve a 3:1 internal resonance, but rather to maximize the nonlinearity within the system. To this end, we set the ratio l_0/a as close to 1 as possible, so the springs are preloaded by a minimal, yet necessary, amount.

4.1.1 Experimental procedure to quantify the linear and nonlinear stiffness

To verify Equation (4.1) and quantify the spring stiffness, Shaw et al. (2016) measured the static displacement of the beam with laser sensors, when applying a known force. In our cantilevered beam setup, due to space limitations, it was impractical to install additional sensors. The cubature Kalman filter will estimate both linear k_L and nonlinear stiffness k_{NL}, with only accelerometer and force sensor data. The true values of k_L and k_{NL} allow

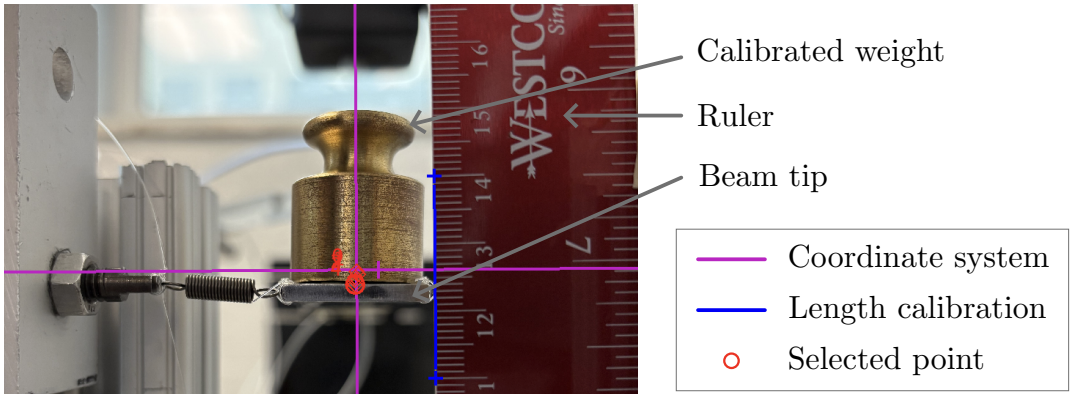

Figure 4.2 **Photograph of the tip of the beam post-processed in Tracker software**

us to validate the filter's estimation and ensure the accuracy of the methodology. However, in practical applications and in the context of digital twins for hydraulic turbines, it is generally not possible to obtain values for all unknown parameters. Hence, we opt for quick and straightforward tests without complex measurement techniques or intricate sensor setups. The tests carried out still allow the verification of the form and the presence of the nonlinear force added by the springs, and the validation of the spring stiffness Equation (4.1) given by Shaw et al. (2016) for our setup.

With the following experimental procedure, illustrated in Figure 4.2, we evaluate the static displacement at the tip of the beam, with controlled loading tests. A mobile phone takes a series of photographs of the tip of the beam, as we apply incrementally calibrated load from 0.02 kg to 1 kg, thereby generating known forces. The phone is mounted in a fixed position, to ensure identical camera alignment for all images. Then we analyze the pictures with the Tracker software. A ruler positioned within the field of view establishes length calibration and defines the coordinate system. We assume that lateral displacements of the beam are negligible compared to the dominant transverse (vertical) displacement. The maximal measured displacements during the static tests are on the order of one centimeter and the motion of the beam is planar. Accordingly, the effects of out-of-plane and lateral deformation are neglected, consistent with the standard small-deflection assumption of the classical beam theory. Parallax distortion is also not taken into account. For each image, we manually select the same point at the tip of the beam in order to track the displacement of this point for each loading case. The resulting data are plotted on a graph and represent the static force-displacement curve (Figure 4.7). To quantify the nonlinearity added by the springs, we fit a cubic function, with the same form as Equation (4.1), to our data with least

squares method. The obtained coefficients approximates k_L and k_{NL}. Since the stiffness can only be tested in the downward direction with this procedure, we cannot directly verify whether the nonlinearity have a symmetric behavior. However, we assume that the system behaves similarly in the upward direction.

4.1.2 Spring fixation design

Three different methods were developed to connect the springs to the beam, as illustrated in Figure 4.3. For each assembly, static force displacement tests were conducted applying the procedure explained in Section 4.1.1. Figure 4.5 compares the results of each test and allows us to qualify the nonlinear behavior of the beam for each different assemblies.

For Assembly 1, we hooked each spring directly onto the beam in a drilled hole, and on another hole screwed on the opposite side (Figure 4.3 (a)). However, the circular hook did not fit inside the sharp-edged cylindrical holes, and instead of following the shape of the hook, the contact zone consisted of two points at the edges. When the beam vibrates, the contact points shift, and the springs move with respect to the beam. The springs then start to vibrate as the beam's displacement amplitude increases. In addition to the noisy vibrations, Assembly 1 also added unwanted damping as a result of energy dissipation as the springs rubs in the hole.

We also observed a softening effect around the first natural frequency in the system response, shown in Figure 4.4, contrary to the expected hardening behavior. To study the region of the beam's first resonance, the shaker imposes a sin chirp excitation with frequencies linearly sweeping from 10 Hz to 25 Hz over 405 seconds, which yields a chirp rate of 0.037 Hz/s. Two tests are carried out with 50 mV and 150 mV input voltages, to study the response of the nonlinear system to different excitation amplitudes. According to Duffing oscillator theory, a system with a positive cubic term exhibits hardening nonlinearity and the natural frequency of the system should increase with the amplitude of the excitation force (Kovacic and Brennan, 2011; Brennan et al., 2008; Wawrzynski, 2021). However, as illustrated in Figure 4.4, the experiment demonstrates a softening effect: the resonance occurs earlier in time for the 150 mV excitation signal compared to the 50 mV signal. The resonance for the higher amplitude signal (150 mV) occurs around $t = 190$ s, and the chirp excites the system at approximately 17.1 Hz. In contrast, for the lower amplitude signal (50 mV), resonance occurs later, around $t = 235$ s, corresponding to a frequency near 18.7 Hz. In both cases, the drop in excitation force (Figure 4.4 (a)) and the marked increase in the amplitude of the acceleration response (Figure 4.4 (b)) characterize the resonance region (Varoto and de Oliveira, 2002). This unwanted effect also appears in the static force displacement curve

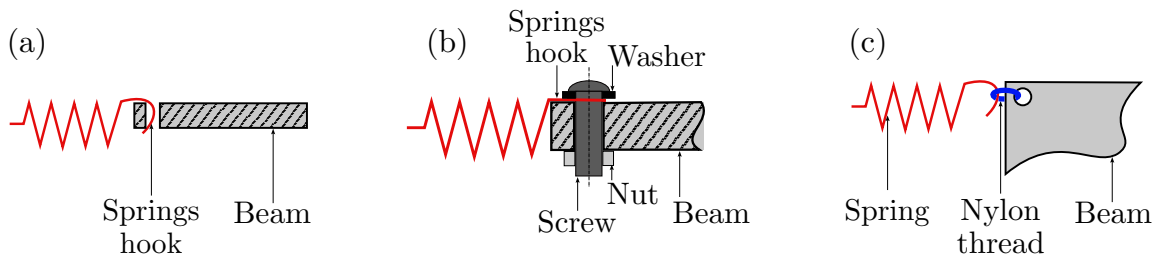

Figure 4.3 **Diagram of the different spring assemblies.** **(a)** Cut view of Assembly 1: the springs are hooked onto the beam. **(b)** Cut view of Assembly 2: the springs are rigidly compressed between a screw and the beam. **(c)** Top view of Assembly 3: a nylon thread knot the springs to the beam

of Assembly 1 shown in Figure 4.5. The static test data points deviate from the global cubic fit within the displacement range of 0 to 0.002 m and force range of 0 to 3 N, illustrating modeling inaccuracy in this region.

To address the hook vibration problem, we tested fixing the springs more rigidly with Assembly 2. We placed screws in the holes at both ends and hooked them with the springs. Then a washer and locknut tighten the spring against the beam and eliminate its relative movements, as presented in Figure 4.3 (b). However, Assembly 2 introduced new problems: the springs bent instead of extending, altering the nature of their nonlinearity. The force displacement curve obtained for assembly 2 is almost linear (Figure 4.5). When a cubic function is fitted to the experimental data points, the resulting linear coefficient is greater for assembly 2 than for assemblies 1 and 3. The fitted nonlinear coefficient is negative, corresponding to softening nonlinearity.

Finally, we adopted the current fixation method, Assembly 3, shown in Figure 4.1 (d) and in 4.3 (c). Nylon thread ties the spring hooks to the two holes at each end. The thread conforms to the shape of the spring hook, resulting in a better contact area. Then Assembly 3 allows the springs to follow the displacement of the beam without adding noisy vibrations. It also reduces the added damping compared to the previous mounting configurations. The force-displacement curve for Assembly 1 exhibits the expected behavior, with the cubic fit precisely matching the experimental data, as shown in Figure 4.5. Although the nonlinear term is less pronounced in Assembly 3 than in Assembly 1, the linear region is less important for Assembly 3 due to the reduced magnitude of the linear term. Consequently, the behavior of the beam, with Assembly 3, exhibits the desired hardening behavior.

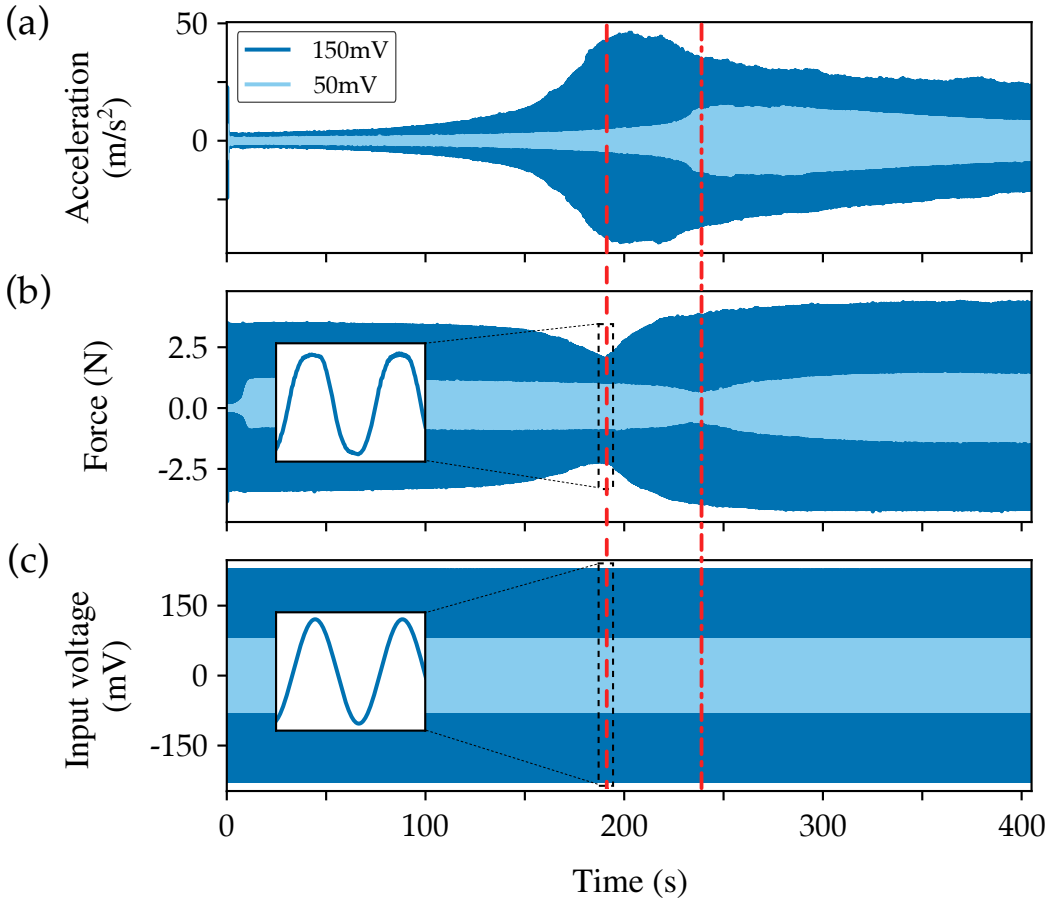

Figure 4.4 **Temporal response of the beam to a sin chirp excitation around the first natural frequency** from 10 Hz to 25 Hz, with a frequency rate of 0.037 Hz/s, for 50 mV and 150 mV of input voltages sent to the modal shaker. **(a)** Acceleration response at the tip of the beam. **(b)** Excitation force applied to the beam by the model shaker, with a zoomed-in view in the resonance region. **(c)** Input voltage signal sent to the shaker, with a zoomed-in view in the resonance region. (–·–·–) and (- - - -) are respectively the resonance region for the signal with 50 mV input voltage and 150 mV input voltage

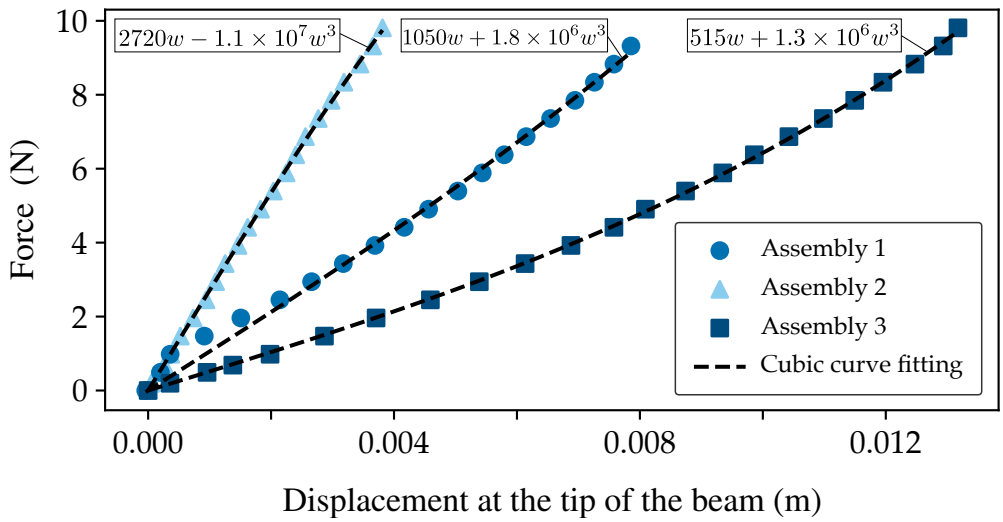

Figure 4.5 **Static force displacement at the free end of the beam for the 3 different springs assemblies**, with corresponding cubic curve fitting equations

4.2 Static force displacement tests

4.2.1 Experimental validation: static testing of the linear beam

We focus first on the linear cantilevered beam without the springs and the sensors, to verify the precision and accuracy of our measurement protocol and analysis method, presented in Section 4.1.1. We measure the static displacement of the beam when various known masses of 0.01 to 0.7 kg are applied to its tip, to estimate the intrinsic bending stiffness of the beam. We compare the experimental data with the theoretical bending stiffness based only on the material and geometric characteristics of the beam: Young modulus E, length L and bending moment of inertia I. We place the mass at the tip of the beam, but its center of gravity is offset from the tip by a distance b, equal to the radius of the mass. The deflection w of a linear cantilevered beam with a point load P not exactly at its free end is expressed as

$$w = \frac{Pa^2(3L - a)}{6EI}, \tag{4.4}$$

with $a = L - d$.

The tests are repeated four times, and four distinct series of photographs are analyzed. Figure 4.6 plots the mean displacement for all tests, with a 95 % confidence interval to quantify the uncertainty region. The confidence interval closely follows the experimental data, indicating that the standard deviation across the four tests is small and that the method exhibits good repeatability and precision. As shown in Figure 4.6, the experimental

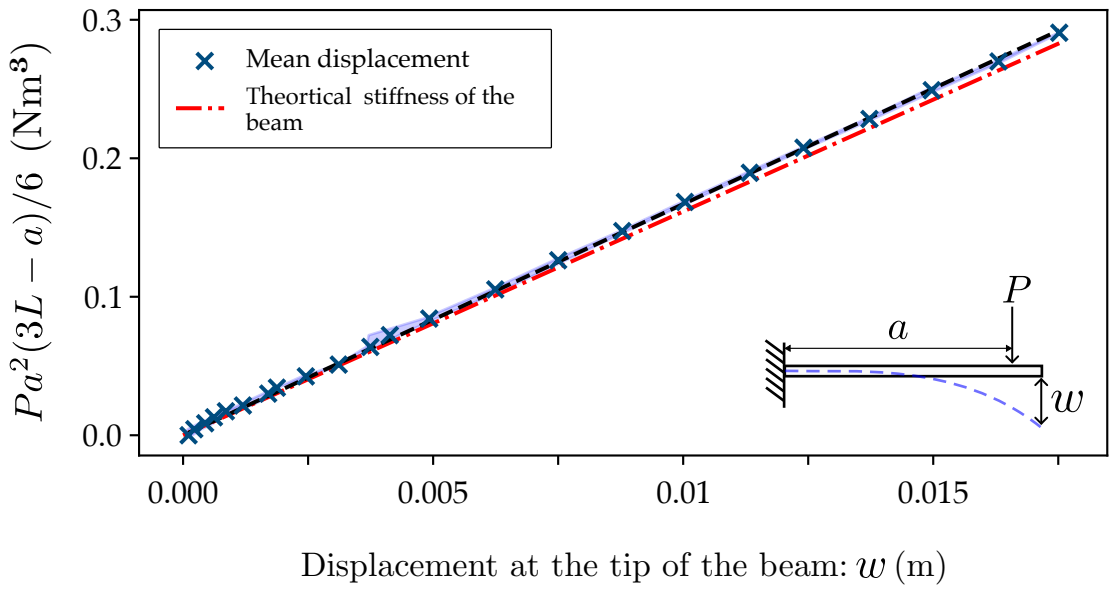

Figure 4.6 **Static displacement at the tip of the beam without the springs and the sensors, when imposing a known force,** with the 95 % confidence interval (shadow). Comparison with the theoretical stiffness of the beam, $EI_{th,geom}$ (-·-·-)

data exhibits the expected linear behavior. The linear fit to the measurements yields a slope of $EI_{th,exp} = 16.69$ Nm^2, whereas the theoretical prediction, based on the parameters given in Table 4.1, is $EI_{th,geom} = 16.16$ Nm^2. This corresponds to a relative error of 3.3 %.

Although the error is small, various factors influence the accuracy of the measurement protocol and must be carefully considered. First, the accuracy of defining the calibration stick within the image is limited by the resolution of the photo. Additionally, consistently selecting the same reference point during image post-processing is challenging, and can introduce further variability in the measured displacements. Although measurement uncertainty is difficult to quantify precisely due to the presence of multiple potential error sources, we estimate that the postprocessing can introduce an error of up to 0.5 mm. In practice, the calibrated weights applied are not true point masses, so the idealized forces delivered to the structure may include minor deviations. Slight changes in camera focus or position between photographs can also introduce minor discrepancies in displacement measurement.

In addition to the sources of uncertainty related to the experimental protocol, inaccuracies in measuring the dimensions of the beam especially the thickness h will directly affect the theoretical stiffness calculation. Since h is cubed in the calculation of the beam's moment of inertia, even a small discrepancy in the measurement of h results in a significant difference in the theoretical value of the beam's stiffness. For example, adding 0.1 mm to h results in a 9 % difference in the value of the theoretical stiffness $EI_{th,geom}$. The theoretical formula also

assumes that the beam's thickness is constant. If this is not the case, the value of I will also be affected, leading to error in the theoretical value.

This protocol allows us to estimate the stiffness added by the springs in the nonlinear case, thereby enabling validation of the CKF's estimation accuracy.

4.2.2 Experimental characterization of the nonlinear springs system

Following the tests on the linear beam, the static displacement of the nonlinear beam was measured with the same procedure. The objective is to confirm that the additional force introduced by the springs, mounted with Assembly 3, follows a cubic relationship. The tests also seek to evaluate both the linear and non linear stiffness coefficients. Calibrated weights, ranging from 0.02 kg to 1 kg, impose a known force and resultant displacement on the beam's free end. As for the linear beam, the mass is not applied exactly at the beam's tip but is offset by a distance equal to the radius of the mass. To account for this offset, we multiply the applied force by the first beam mode shape evaluated at the mass's actual location along the beam. This correction acknowledges that the effective excitation point differs from the geometric tip due to the mass's size. Each series of measurements is repeated four times, and the mean displacement for each load, along with the 95 % confidence interval, is plotted in Figure 4.7. The experimental force–displacement data are then fitted with a cubic model of the same form as Equation (4.1), representing the combined effect of linear and nonlinear stiffness contributions. The fitted curve identifies both the total linear stiffness, including the beam bending stiffness and the springs contribution, and the cubic stiffness coefficient. To isolate the linear stiffness contribution of the springs, we subtract the intrinsic bending stiffness of the linear beam, determined from the previous tests, from the total fitted linear stiffness of the nonlinear system. The resulting value corresponds solely to the stiffness introduced by the springs.

As shown in Figure 4.7, the experimental data follow a cubic nonlinear trend as the fitted curve matches the data points. From the fitted model, a total linear stiffness of 508 N/m and a cubic stiffness of $k_{NL} = 1.22 \times 10^6$ N/m^3 are obtained. Subtracting the experimental bending stiffness of the linear beam: $3EI_{th,exp}/L^3$ from the total estimated linear coefficient yields a stiffness attributable to the springs of $k_L = 138$ N/m. Although the identified nonlinear stiffness coefficient has a high value, its influence on the system's response becomes significant only at large displacements. When the amplitude of the displacement is below 0.004 m, the nonlinear term in the model is negligible compared to the linear term, and the resulting curve coincides almost exactly with the purely linear response plotted in the graph.

To verify the applicability of the geometrical model (2.10), we compare the experimental

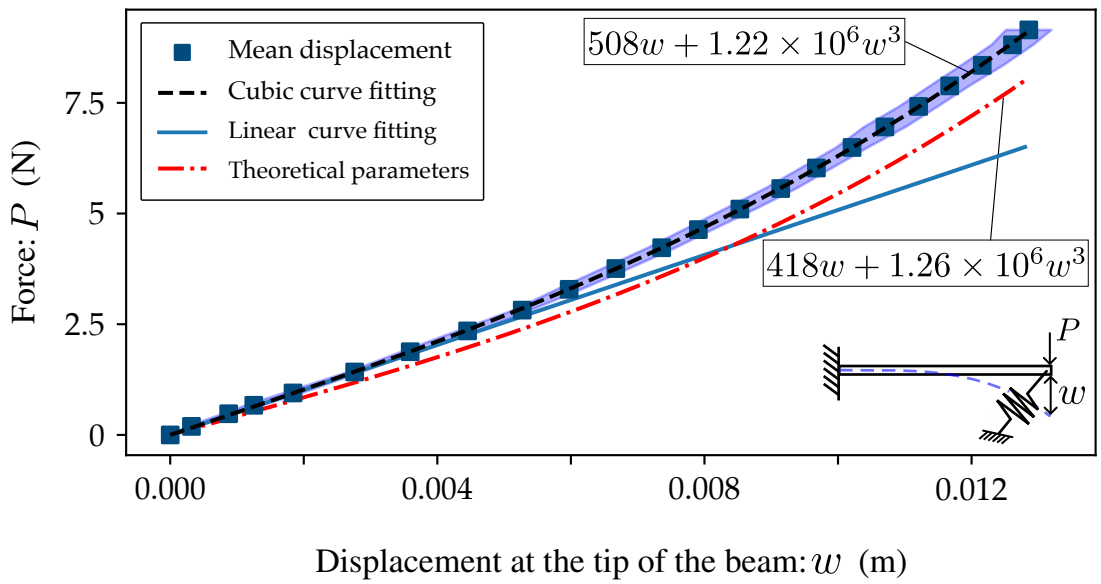

Figure 4.7 **Static displacement at the tip of the nonlinear beam with the springs, when imposing a known force**, with its 95 % confidence interval (shadow), and the corresponding cubic equation from curve fitting (- - - -). Comparison with the linear part of the equation (——), to illustrate the nonlinear behavior of the beam. The dotted curve (-·-·-) is obtained with Equations (4.2) and (4.3) from Shaw et al. (2016)

results with the analytical equations (4.2) and (4.3). We insert the known parameters of the setup into these equations, and the distance $a = 24.3$ mm is approximately estimated from beam photo. To obtain a coherent analytical curve, we add the experimentally determined linear bending stiffness of the beam, $3EI_{th,exp}/L^3 = 371$ N/m, to the linear stiffness. The resulting theoretical linear and nonlinear stiffness values are 47.5 N/m and 1.26×10^6 N/m^3, respectively. While the analytical k_{NL} differs by only 3.3 %, the linear stiffness predicted by the analytical model is significantly lower than the experimentally measured value. Measurement errors are not a critical issue, since the aim of the project is to estimate k_L and k_{NL} with the Cubature Kalman filter. In this context, the current estimates serve to confirm the accuracy of the estimated parameters and to validate that the CKF performs reliably for our system.

4.3 Beam setup modeling

4.3.1 General assumptions and equation of motion

Consider a slender cantilever beam with a transverse deflection $w(x,t)$, to which a harmonic excitation force of magnitude F_0 and excitation frequency Ω_e is applied at the shaker location

L_S. All structural parameters of the beam are constant: length L, Young modulus E, moment of inertia I and mass per unit length m. The perpendicular springs attached at the free end of the beam introduce nonlinearity as a force expressed in Equation (4.2). The nonlinear stiffness k_{NL} times displacement cubed recalls the Duffing oscillator expression, widely studied by Kovacic and Brennan (2011). Based on Euler-Bernoulli beam theory, the following equation of motion governs the transverse vibration of the beam:

$$\begin{aligned}&(m + m_S\delta(x - L_S) + m_{Acc}\delta(x - L_{Acc}))\,\frac{\partial^2 w(x,t)}{\partial t^2} + c\frac{\partial w(x,t)}{\partial t} + EI\frac{\partial^4 w(x,t)}{\partial x^4}\\&+ k_L w(x,t)\delta(x - L) + k_{NL}w^3(x,t)\delta(x - L) = F_0\sin(\Omega_e t)\delta(x - L_S),\end{aligned} \tag{4.5}$$

where δ is the Dirac delta. Meirovitch (2010) provides details about the derivation of this equation. In this mathematical model of the beam, we take into account the mass of the magnet plus the force sensor m_s at the shaker location L_S, and the mass of the accelerometer m_{Acc} at the accelerometer location L_{Acc}. Their effect on the behavior of the beam is non-negligible, as these masses influence the beam's natural frequencies. Furthermore, we will use this model within the CKF, so it must describe the real physics of the system as accurately as possible. We also consider the structural damping c of the beam and assume Rayleigh damping. Details regarding the determination of associated coefficients will be provided in Section 4.3.3 and 4.4.

4.3.2 Discretization through Galerkin method

We apply the Galerkin method to discretize the continuous equation of motion (4.5). The finite sum of modal coordinates $q_i(t)$ multiplied by spatial mode shape functions $\phi_i(x)$ approximate the transverse deflection $w(x,t)$:

$$w(x,t) = \sum_{i=1}^{N} \phi_i(x) q_i(t), \tag{4.6}$$

with N the number of modes considered to approximate the solution. A higher number of modes leads to more accurate solution, but also increases the size of the matrix equations, and so the computational cost. We can arbitrarily choose the mode shape functions $\phi_i(x)$ as long as they satisfy the boundary conditions. We consider cantilevered beam mode shape functions:

$$\phi_i(x) = \cosh(\frac{\lambda_i x}{L}) - \cos(\frac{\lambda_i x}{L}) - \sigma_i\left(\sinh(\frac{\lambda_i x}{L}) - \sin(\frac{\lambda_i x}{L})\right), \tag{4.7}$$

where :

$$\sigma_i = \frac{\sinh(\lambda_i) - \sin(\lambda_i)}{\cosh(\lambda_i) + \cos(\lambda_i)}, \tag{4.8}$$

and λ_i are the solutions of the transcendental equation:

$$\cos(\lambda_i)\cosh(\lambda_i) + 1 = 0, \tag{4.9}$$

as developed by Meirovitch (2010).

We substitute the assumed solution (4.6) in the equation of motion (4.5), multiply it by an orthogonal mode shape $\phi_j(x)$ and integrate the resulting equation over the length of the beam L. We obtain the following equation for $1 \leq j \leq N$:

$$\begin{aligned}
&\sum_{i=1}^{N} \Bigg[\int_0^L (m + m_S\delta(x - L_S) + m_{Acc}\delta(x - L_{Acc}))\phi_i(x)\phi_j(x)\ddot{q}_i(t)\mathrm{d}x \\
&+ \int_0^L c\,\phi_i(x)\phi_j(x)\dot{q}(t)\mathrm{d}x + \int_0^L EI\phi_i''''(x)\phi_j(x)q_i(t)dx \\
&+ \int_0^L k_L\delta(x - L)\phi_i(x)\phi_j(x)q_i(t)\mathrm{d}x + \int_0^L k_{NL}\delta(x - L)\phi_j(x)q_i^3(t)\mathrm{d}x \Bigg] \\
&= \int_0^L F_0\sin(\Omega_e t)\delta(x - L_S)\phi_j(x)\mathrm{d}x
\end{aligned} \tag{4.10}$$

with $(\dot{\cdot})$ for the time derivative and $(')$ for space derivative.

The mode shape function $\phi_i(x)$ and $\phi_j(x)$ are orthogonal, so

$$\int_0^L \phi_i(x)\phi_j(x)\mathrm{d}x = \begin{cases} 0 & \text{if } i \neq j \\ L & \text{if } i = j \end{cases}. \tag{4.11}$$

When we differentiate the cantilevered beam mode shape function four times, we get

$$\phi_i''''(x) = \frac{\lambda_i^4}{L^4}\phi_i(x). \tag{4.12}$$

Then we simplify equation (4.10) with equations (4.11) and (4.12), and we obtain the N

following equations

$$\sum_{i=1}^{N}\Bigg[(mL\delta_{ij}+m_S\phi_i(L_s)\phi_j(L_S)+m_Acc\phi_i(L_Acc)\phi_j(L_Acc))\ddot{q}_i(t)+c\,L\delta_{ij}\dot{q}_i(t) \\ +\left(\frac{EI\lambda_i^4}{L^3}\delta_{ij}+k_L\phi_i(L)\phi_j(L)\right)q_i(t)+k_{NL}\phi_i^3(L)\phi_j(L)q_i^3(t)\Bigg]=F_0\sin(\Omega_e t)\phi_j(L_S), \tag{4.13}$$

with $1 \leq j \leq N$. Written in matrix form, this equation becomes

$$\mathbf{M}\ddot{\mathbf{q}}(t)+\mathbf{C}\dot{\mathbf{q}}(t)+\mathbf{K_L}\mathbf{q}(t)+\mathbf{K_{NL}}\mathbf{q}^3(t)=\mathbf{F}\sin(\Omega_e t), \tag{4.14}$$

where $\mathbf{M}$, $\mathbf{C}$, $\mathbf{K_L}$, $\mathbf{K_{NL}}$ are respectively, mass, damping, linear stiffness and nonlinear stiffness $N \times N$ matrices. $\mathbf{q}$ and $\mathbf{F}$ are respectively, modal coordinates, and modal force coefficients $N \times 1$ vectors. Finally, the equation of motion obtained for the cantilevered beam with springs corresponds to the equation of a nonlinear forced multi-degree-of-freedom coupled Duffing oscillator. This kind of nonlinearity is commonly encountered in structural dynamics, and can produce amplitude-dependent frequencies, bifurcations, and chaos, especially for large forcing or nonlinearity (Kovacic and Brennan, 2011).

We will subsequently consider only the first three modes of vibration of the beam in the Galerkin decomposition ($N = 3$). They capture the dominant dynamic behavior of the beam within the frequency range of interest: around the first natural frequency. The energy contribution E_n for the first six modes of the beam without the springs is plotted in Figure 4.8. E_n is directly proportional to the square of its modal amplitude W_n and natural frequency ω_n, as expressed by the kinetic energy formula:

$$E_n=\frac{1}{2}W_n^2\omega_n^2. \tag{4.15}$$

W_n corresponds to the amplitude of each mode under harmonic excitation, and is governed by the classic forced vibration equation. When the harmonic excitation force has a frequency of 20 Hz and an amplitude of 3 N, the first mode represents more than 95 % of the total dynamic energy of the system (Figure 4.8). The natural frequencies of higher-order modes are significantly higher than the excitation frequency, resulting in an attenuated response from these modes. Limiting the model to the first three modes therefore provides a good balance between accuracy and computational efficiency.

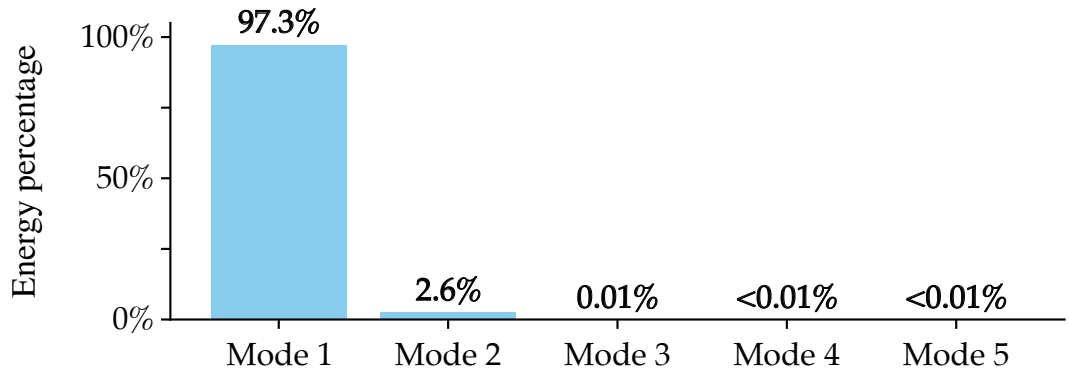

Figure 4.8 **Modal energy distribution** for the cantilevered beam, without the springs and accounting for the mass of the accelerometer and the magnet and force sensor assembly, excited at 20 Hz and with a force amplitude of 3 N

4.3.3 Rayleigh damping model

In this study, the forces induced by damping are proportional to the velocity of the beam. This viscous damping assumption is well-suited to lightly damped, homogeneous materials like steel, where complex, nonlinear damping effects are negligible. The energy dissipation mechanisms in the steel cantilevered beam are essential to accurately model the true dynamic behavior of the system, even if the intrinsic damping capacity of steel is very low: typically with damping ratios below 1 %. We model the damping matrix $\mathbf{C}$ as Rayleigh (or proportional) damping where $\mathbf{C}$ is a linear combination of both mass $\mathbf{M}$ and stiffness matrices $\mathbf{K}$ as

$$\mathbf{C} = \alpha\mathbf{M} + \beta\mathbf{K}. \tag{4.16}$$

We consider $\mathbf{K}$ as the stiffness matrix of the beam without the springs. α and β are two proportionality coefficients determined to match the modal damping coefficients ζ_i and the natural frequencies ω_i of the first two modes ($i = 1, 2$) with the following formula:

$$\zeta_i = \frac{1}{2}\left(\frac{\alpha}{\omega_i} + \beta\omega_i\right). \tag{4.17}$$

Modal coefficients ζ_i and ω_i are obtained through modal analysis of the experimental setup. According to equation (4.17), we only take the first two modes of vibration of the beam, into account to determine α and β. This approach is well justified, as the vibration response of the cantilevered beam is largely determined by the first mode in the region of interest (Figure 4.8). Therefore, considering only the first two modes ensures that the fitted damping model accurately reflects the main energy dissipation mechanisms governing the beam's behavior. Assuming Rayleigh damping, simplifies the mathematical formulation and enables classical

modal analysis while ensuring that the mathematical model accurately incorporates material damping.

4.4 Modal analysis of the cantilevered beam without the springs

In order to improve the understanding of the experimental setup and to determine the natural frequencies ω_n, and modal damping ratios ζ_n of the first three modes, we conducted a modal analysis on the beam without the springs. Then, with the modal parameters, we identified the Rayleigh damping coefficients required to model the damping in the setup.

The modal shaker imposes a white noise excitation to the structure, subjecting it to a broad range of frequencies. The accelerometer measures the acceleration response at the tip of the beam, while the force sensor records the excitation force at the shaker attachment point. Both signals are sampled at 2048 Hz. The experimental acquisition setup is detailed in Section 4.1, and shown in Figure 4.1. We repeated white noise tests six times with varying shaker input voltages, resulting in different excitation amplitudes. Given the system's linearity, these amplitude variations do not affect the results. For each test we recorded data continuously for 150 seconds to ensure sufficient data acquisition and improve frequency resolution, to reduce noise in the FRF. In a subsequent post-processing step, acceleration and force signals are converted in the frequency domain through the Fourier transform and the experimental FRF is computed according to Equation (2.11). Despite the acquisition time of 150 seconds, the FRF shown in Figure 4.9 (a) remains noisy. Therefore, to facilitate accurate identification of the modal parameters, a Savitzky-Golay filter filters high-frequency noise and smooths the FRF, as shown in Figure 4.9 (a).

The cantilevered beam system without the springs is simple and characterized by well-separated and decoupled modes with light damping. Therefore SDOF curve fitting methods are well suited, as discussed in Section 2.2.3. Then, each modes are considered separately. For the first three modes, we isolate the resonance region and fit the SDOF FRF analytical expression (2.12) to the FRF curve with the least squares methods (Figure 4.9 b, c, d). During the fitting process, the natural frequency ω_n, the damping ratio ζ_n, and the stiffness k_n are unknown parameters, and need to be identified. The mean values of these identified parameters over the six tests are summarized, for the first three modes, in Table 4.2. Then by incorporating $\omega_{1,2}$ and $\zeta_{1,2}$ of the first two modes in Equation (4.17), we obtain the Rayleigh damping coefficients $\alpha = 0.49$ and $\beta = 3.4 \times 10^{-6}$. α and β quantify the mass- and stiffness contributions, according to Equation (4.16). Therefore, the Rayleigh damping model is fully established.

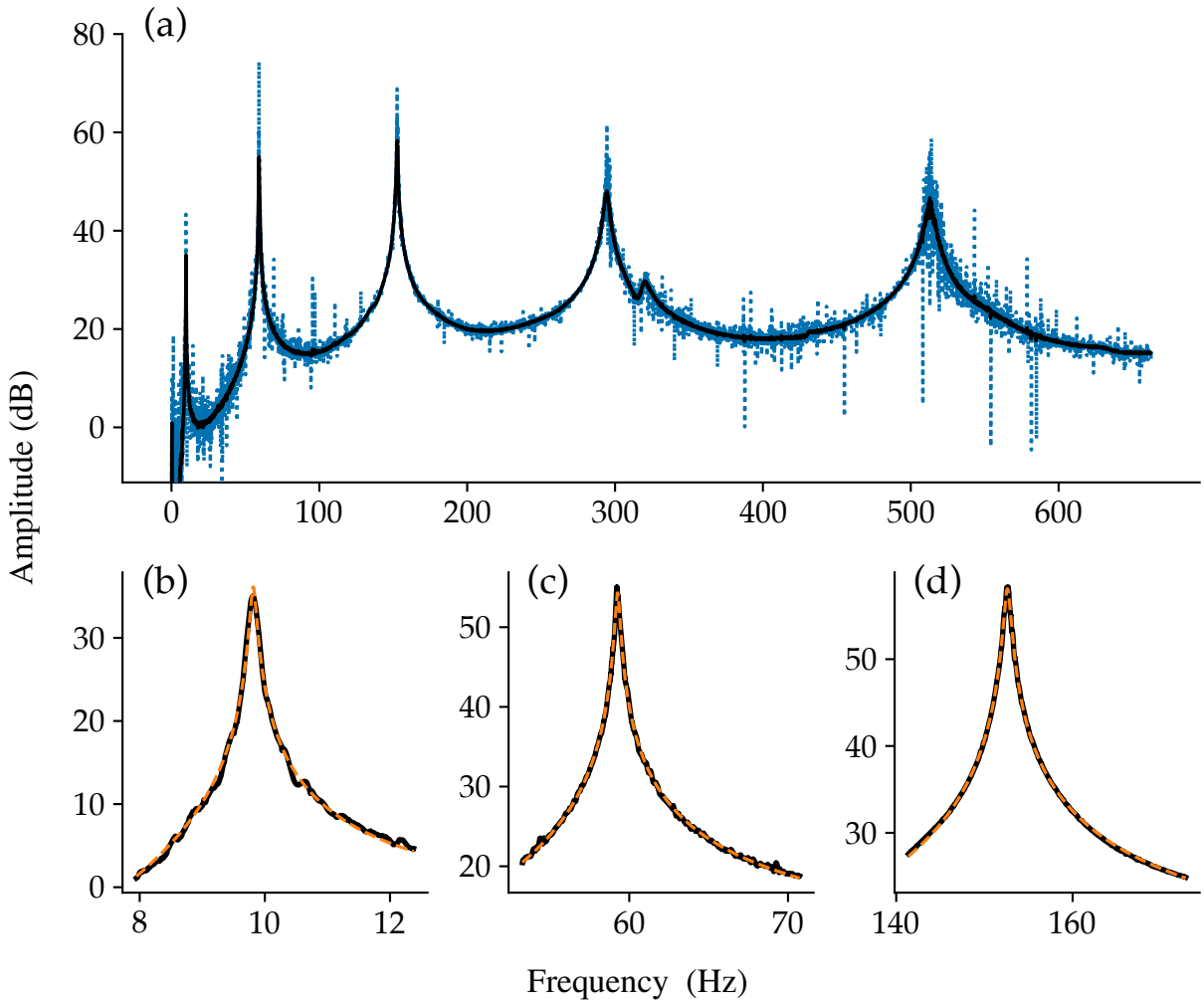

Figure 4.9 **Frequency response function and curve fitting for modal identification, of the cantilevered beam without the springs, and with the mass of the accelerometer and the magnet and force sensor assembly. (a)** Experimental (·····) and filtered (——) FRF of the beam. **(b)**, **(c)**, **(d)** are zoomed-in view of the first three resonance peaks (——) and the results of the curve fitting (- - - -)

4.5 Dynamic response of the cantilever beam setup: linear case, the beam without springs and nonlinear case, the beam with springs

Before estimating the unknown linear and nonlinear stiffness with the CKF, we first verify that the mathematical model accurately describes the experimental data. As the CKF is a model-based approach, its ability to solve the inverse problem depends on the quality of both the experimental data and the accuracy of the model. Before introducing the nonlinear boundary condition (the spring system), the model must first replicate the dynamic response of the linear cantilever beam without the spring but with the accelerometer and the magnet

Table 4.2 **Modal properties of the cantilevered beam, without the springs and with the accelerometer and the magnet and force sensor assembly, obtained with the FRF**

Mode N	Experimental f_n [Hz]	ζ_n
1	9.8	0.0041
2	59.2	0.0013
3	153	0.0040

and force sensor assembly, which serves as a baseline configuration analogous to a healthy hydraulic turbine shaft line. After verifying the accuracy of the linear model, we next confirm that our nonlinear dynamic data exhibit the expected nonlinear behavior. This step is essential before estimating parameter with the CKF, ensuring that we have clear, high-quality nonlinear measurements and that the system's dynamics are well characterized. We then extend the linear model by adding the nonlinear spring contribution and this nonlinear model will be incorporated into the CKF to estimate k_L and k_{NL}.

4.5.1 Comparison of experimental and simulated data for the cantilever beam without springs

To assess the accuracy of the mathematical model, the frequency–amplitude curves, obtained from experimental measurements, and numerical simulations are compared. To generate experimentally this curve, we measure the response of the beam for different frequencies. For each test, the shaker imposes a sinusoidal excitation with an input voltage of 150 mV to the beam. We tested 34 different frequencies around the first natural frequency, ranging from 6 Hz to 15 Hz, with a denser selection of points near resonance. Each test records the system's response: force and acceleration, during 90 seconds, at a sampling rate of 2048 Hz. After each measurement, we extract the steady-state amplitude of the response, and plot it as a function of the excitation frequency, yielding the amplitude–frequency curve (Figure 4.10).

The same model, implemented within the Kalman filter framework, simulates the response of the linear beam without springs, with identical frequency points, duration, and sampling rate as in the experiments. This model solves the equation of motion of the beam (4.14), without considering the terms added due to the springs, with a Range Kutta 4 integration scheme. Table 4.3 compares the natural frequencies obtained from experimental FRF analysis, with the frequencies computed from the mathematical model, with the two different stiffness values: determined experimentally $EI_{th,exp}$, and from geometric properties $EI_{th,geom}$.

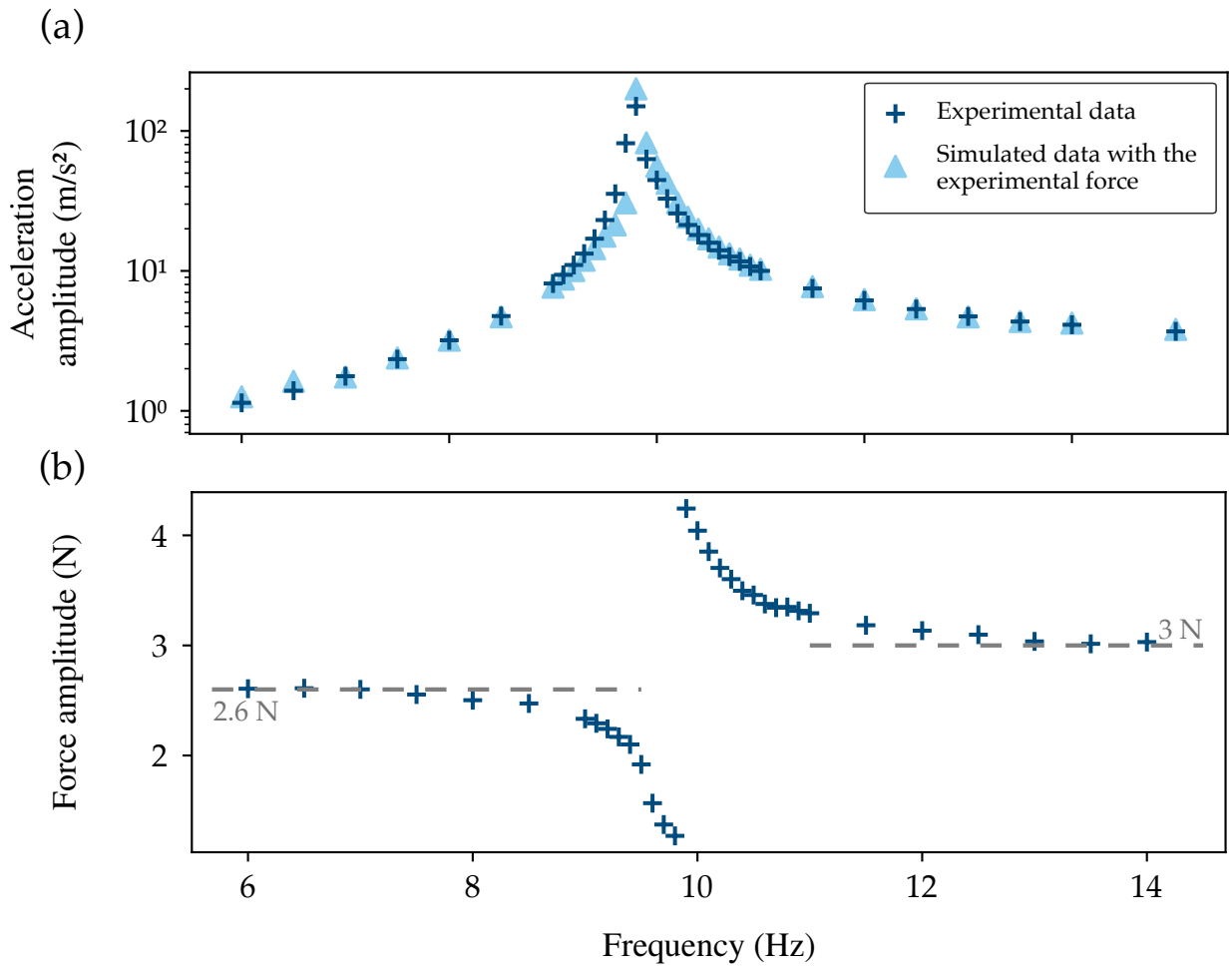

Figure 4.10 **Response of the linear beam, without springs and with the accelerometer and the magnet and force sensor assembly, in the resonance region as a function of frequency.** (a) Steady-state acceleration amplitude at different frequencies for experimental data (+), and simulated data considering the experimental excitation force (△). (b) Experimental excitation force amplitude recorded by the force sensor at different frequencies

With these two stiffness values, the simulated and experimental frequencies do not perfectly match. Our goal is to optimize the linear model to best fit the experimental linear data before introducing nonlinearity. To achieve this, we adjust the model derived from the experimental setup parameters, presented in Table 4.1, by identifying the optimal stiffness EI_{cor} and modal mass M_{cor} that align with both the experimental natural frequency and the amplitude outside the resonance regions. The first natural frequency $\omega_1 = \sqrt{EI/M_1}$ is fixed and is equal to the first experimental resonant frequency (9.8 Hz). The least squares method minimizes the sum of the squared differences between the experimental data and the simulated model predictions, fitting the stiffness and modal mass so that the amplitude in the frequency ranges

6 Hz to 8.5 Hz and 11.5 Hz to 15 Hz matches the experimental data. This process yields corrected values of $EI_{cor} = 12.14$ Nm^2 and a modal mass $M_{cor} = 0.26$ kg, which is reduced by 16 % relative to the initial modal mass $M_1 = 0.31$ kg. Table 4.3 also summarizes the new natural frequencies obtained. All the other parameter values implemented in the model correspond to those of the experimental setup, presented in Table 4.1.

In the CKF framework, the excitation force incorporated into the mathematical model is directly obtained from the experimental force measured by the force sensor. Then we incorporate the experimental excitation force of Figure 4.10 in the model, to reflect the real force magnitude generated by the shaker. Experimental and simulated steady-state acceleration amplitudes are presented together as functions of the excitation frequency in Figure 4.10(a), for direct comparison. The corresponding force magnitude applied by the shaker during each test is also plotted in Figure 4.10 (b), showing a drop at the resonance frequency due to interactions between the beam and the shaker. At the resonance frequency of 9.8 Hz, the amplitude of the excitation force reaches its minimum value of 1.3 N. Right after this, at 9.9 Hz, the force increases to 4.2 N. Outside the resonance region, the transmitted force remains relatively constant, at approximately 2.8 N.

With the corrected model, the simulated and experimental frequency responses show good agreement both in the location of the resonance, and in the acceleration amplitude. The maximum amplitudes observed at resonance (9.8 Hz), differ between experiment and simulation with a relative error of 30 %. In the frequency ranges before resonance (6 Hz to 9 Hz) and after resonance (10.8 Hz to 15 Hz), the theoretical model shows good agreement with the experimental data. The mean relative error in steady-state acceleration amplitudes 3.4 %.

The good accuracy of the model outside the resonance region is expected, as we applied the least squares method within these frequency ranges to improve the model's fit to the experimental data. The need to correct the initial model to improve its accuracy in describing experimental data may arise from several factors. Primarily, the assumed cantilever beam mode shape may not accurately represent the true mode shapes of beams with the discrete

Table 4.3 **Natural frequencies f_n of the first three modes for different stiffness values, compared with experimental values obtained from the FRF analysis**

	$EI_{th,exp} = 16.69$ Nm^2	$EI_{th,geom} = 16.16$ Nm^2	$EI_{corr} = 12.14$ Nm^2	FRF f_n
f_1	10.18	10.01	9.8	9.8
f_2	62.3	61.3	59.7	59.2
f_3	159.7	156.6	149.5	153

masses (magnet plus force sensor and accelerometer). Variations in the beam's thickness have a significant impact on its stiffness EI due to the cubic dependence of the moment of inertia on thickness. Then, slight inaccuracies in measuring critical dimensions, such as the exact positions of the shaker and accelerometer, can substantially affect the dynamic response of the model but are challenging to evaluate precisely. In the resonance region, the lower amplitude measured in the experiment indicates that the actual system is more damped than predicted by the mathematical model, meaning the model slightly underestimates damping.

The CKF framework is specifically designed to accommodate model imperfections and measurement noise. This allows effective parameter estimation, effective parameter estimation even when the model does not perfectly represent the observed data. Our model accurately describes the behavior of the beam without springs and matches the experimental data. It provides a solid foundation and serves as a reliable baseline before incorporating the spring boundary condition into the model and considering nonlinear data for parameter estimation.

4.5.2 Dynamic response of the beam with the perpendicular springs

Before applying the CKF to the nonlinear experimental data, it is essential to ensure that we measure clean and reliable data. The static tests presented in Section 4.2.2 confirm the nonlinear behavior of the beam due to the spring system under static conditions. To verify its dynamic behavior, we excite the beam with both single-frequency (harmonic) and multi-frequency (chirp) excitations, assessing whether the system's response also exhibits nonlinear characteristics.

We acquire the experimental data with the same procedure as for the linear configuration (beam without springs). Since adding the springs changes the system's natural frequency, the system is excited with frequencies ranging from 5 Hz to 25 Hz, with a denser selection of points around the new resonance region, making a total of 29 tests. Figure 4.11 (a) shows the steady-state acceleration amplitude, and Figure 4.11(b) presents the experimental force amplitude, both as functions of frequency. A force drop-out effect occurs in the resonance region due to interactions between the beam and shaker. This effect is less pronounced than in the linear case: the difference between the maximum and minimum force is 1.4 N (from 2.1 N to 3.5 N), whereas a force variation of 2.9 N is observed for the linear configuration.

The experimental frequency–amplitude response, in Figure 4.11 (a), shows the expected nonlinear hardening behavior, as the resonance curves bend towards higher frequencies. After reaching the peak amplitude at 11.5 Hz, the response exhibits a sharp jump down, highlighting the unstable region and the nonlinear nature of the system. Figure 4.12 presents the temporal response of the beam under a sin chirp excitation, sweeping frequencies from 8 Hz

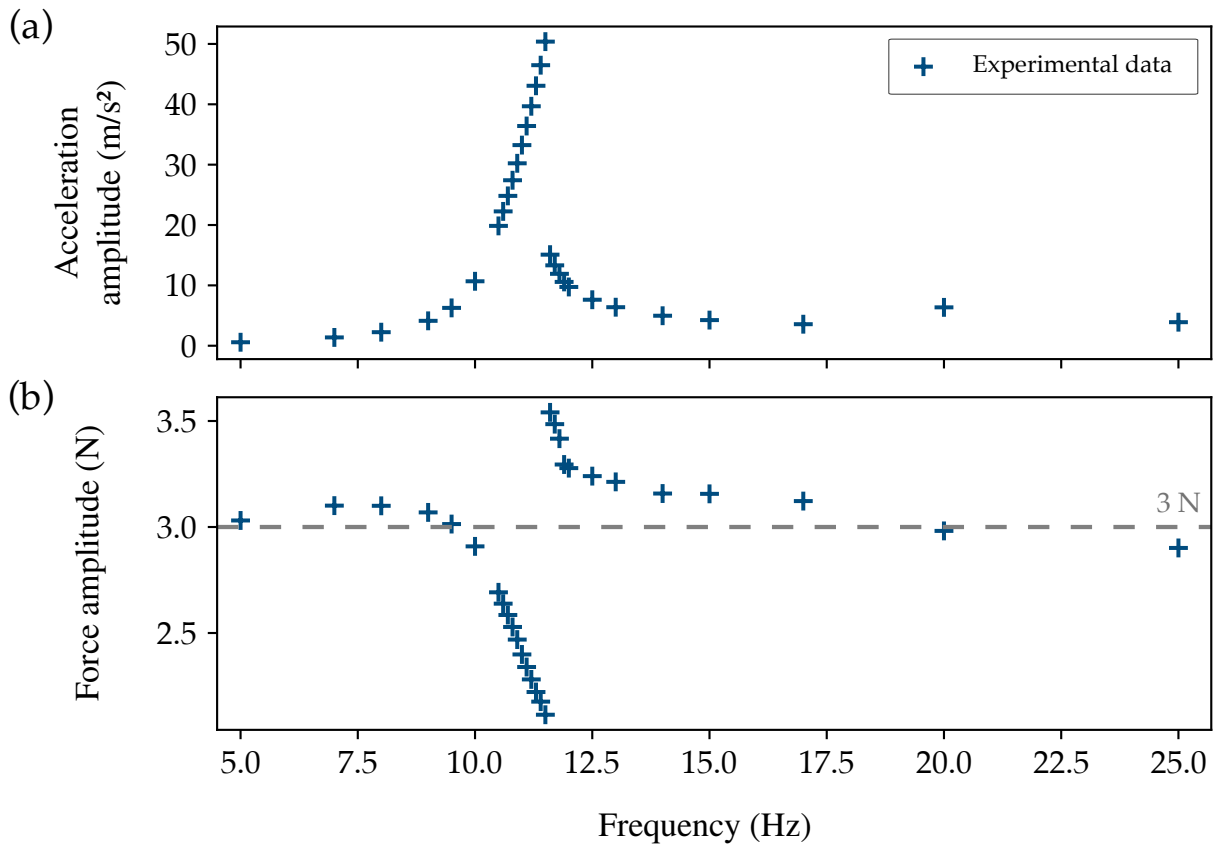

Figure 4.11 **Response of the beam with the perpendicular springs in the resonance region as a function of frequency.** (a) Steady-state acceleration amplitude at different frequencies for experimental data (+). (b) Experimental excitation force amplitude recorded by the force sensor at different frequencies

to 18 Hz, with a frequency rate of 0.083 Hz/s. This figure only shows the resonance region, between 35 s and 60 s, while the complete chirp excitation lasts 120 s in total. At time $t = 53$ s, the system passes beyond the resonance frequency and the acceleration amplitude decreases abruptly, confirming the jump down phenomenon.

We also examine whether the analytical frequency response for the SDOF Duffing oscillator in Equation (2.16), matches the experimental data. Near resonance, the first mode dominates the beam response, allowing the dynamics to be approximated by a SDOF model governed by Equation (2.13). Considering that the measured acceleration data in steady state is sinusoidal, we convert the acceleration amplitudes to displacement amplitudes by dividing the acceleration by ω^2. The experimental results are then nondimensionalized according to Equation (2.15). In our case the force f applied to the beam, correspond the modal force: the product of the force amplitude and the mode shape function evaluated at the shaker's location $\phi_1(L_S)$. Figure 4.13 displays the nondimensional experimental data alongside the

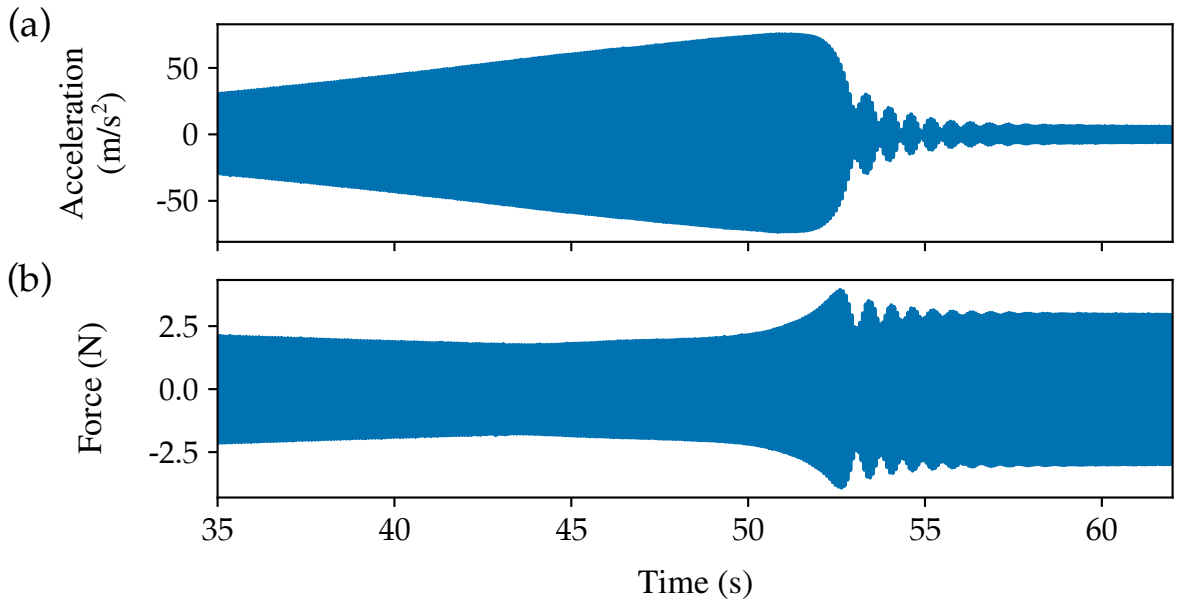

Figure 4.12 **Temporal response of the nonlinear beam with the springs to a sin chirp excitation around the first natural frequency**, from 8 Hz to 18 Hz, with a frequency rate of 0.083 Hz/s, for 150 mV input voltage. **(a)** Acceleration response at the tip of the beam. **(b)** Excitation force applied to the beam by the model shaker

theoretical curve. We selected the experimental values of k_L and k_{NL} obtained from the static as input parameters. The damping coefficient is manually adjusted to achieve a good agreement between the experimental and theoretical amplitude responses. The theoretical curve is computed with the input parameters presented in Table 4.4. With these input parameters, the resulting RMSE is 0.68, indicating a good agreement between the Duffing model and the experimental results.

The damping value required to match the experimental amplitude response is higher than the one obtained from the modal analysis of the beam without springs system for the first mode (Table 4.2). Although the addition of the spring system should not theoretically increase damping, in practice, additional energy dissipation occurs. In the nonlinear configuration, the nylon threads attaching the springs to the beam move along with the beam's vibration, generating friction and thus contributing to energy loss. Consequently, the experimental damping in the nonlinear configuration is higher than in the linear case, primarily affecting the response amplitude in the resonance region, while having a limited effect outside this frequency range. Overall, the theoretical Duffing oscillator frequency response described well our nonlinear system. The experimental results demonstrate the intended nonlinear hardening behavior in the resonance region, confirming that the addition of nonlinear springs to the beam effectively generated the desired dynamics.

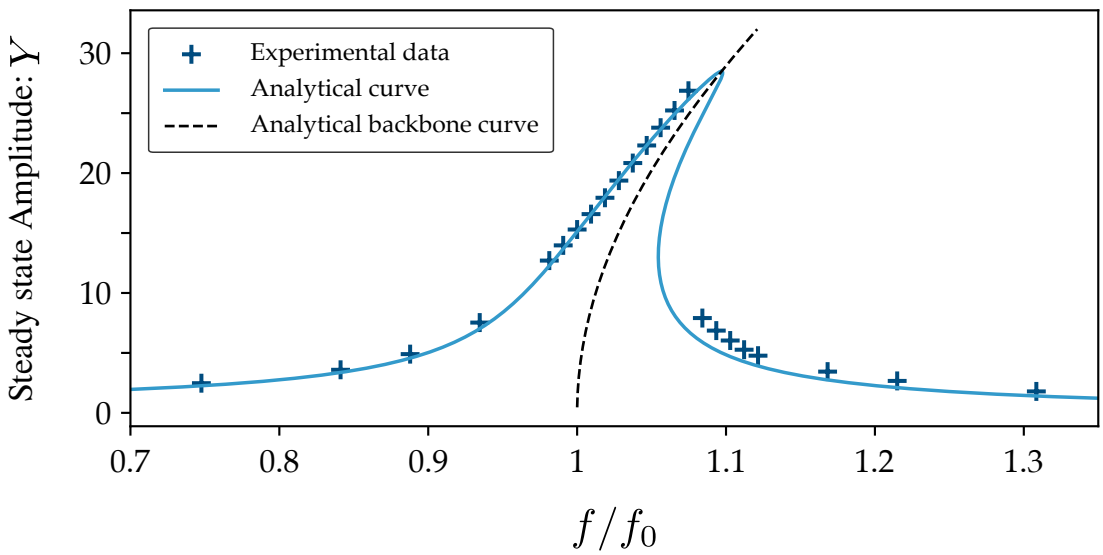

Figure 4.13 **Dimensionless frequency-amplitude curve**, comparing experimental data points (+) with the theoretical fit (——), around the first natural frequency

Table 4.4 **Fitting input values compared to excepted values**

	Input Values	Units
k_L	508	N/m
k_{NL}	1.22×10^6	N/m^3
ω_0	10.7	Hz
f	0.19	N
ζ	0.017	

CHAPTER 5 PARAMETER ESTIMATION OF THE BEAM SETUP WITH CUBATURE KALMAN FILTER

After developing the mathematical model to describe the behavior of the cantilever beam, and ensuring the acquisition of clean nonlinear experimental data, this chapter presents the CKF framework for solving inverse problems and estimating unknown system parameters. The proposed method is first verified with simulated data and then validated through experiments, demonstrating its capability to accurately estimate nonlinear coefficients.

5.1 Methodology: The cubature Kalman filter framework

The CKF jointly estimates the states $\mathbf{x}_k$ and the unknown parameters $\boldsymbol{\theta}_k$ through an augmented state space vector $\mathbf{z}_k$, as expressed in Equation (5.1). It incorporates both the physical model of the beam, developed in Section 4.3, and experimental data recorded by the accelerometer and the force sensor. Based on the physical model, the overall state vector includes, the system's modal coordinates and their derivatives: $\mathbf{q}$ and $\dot{\mathbf{q}}$, and the linear and nonlinear stiffness coefficients: k_L and k_{NL}. We approximate the motion of the beam with the first $N = 3$ modes. M is the number of estimated parameters. Then the 8×1 augmented state space vector is written as:

$$\mathbf{z}_k = \begin{bmatrix} \mathbf{x}_{k,(2N\times 1)} & \boldsymbol{\theta}_{k,(M\times 1)} \end{bmatrix}^\top = \begin{bmatrix} \mathbf{q}_{N\times 1} & \dot{\mathbf{q}}_{N\times 1} & k_L & k_{NL} \end{bmatrix}^\top . \tag{5.1}$$

To adjust the values of the process and the measurement noise covariance matrices ($\mathbf{Q}$ and $\mathbf{R}$) at each iteration, we add the adaptive equations (2.6),(2.7) to the CFK algorithm presented in Algorithm 2. The NOMAD optimizer, developed by Audet et al. (2021), optimizes the initial values of the CKF: including the diagonal elements of the matrices $\mathbf{Q}$, and $\mathbf{R}$, as well as their associated forgetting factors α_Q and α_R, by running the filter multiple times. Figure 5.1 presents an overview of this framework with the CKF loop inside the NOMAD optimization loop.

The estimation process with the CKF requires initializations of the system states $\mathbf{x}_0$ and parameters θ_0. We also define the initial covariance matrix $\mathbf{P}_0$, to quantify the level of confidence in this prior knowledge and inform the filter about the assumed level of uncertainty at the start of the estimation. For the first iteration of the NOMAD optimization, initial values of the parameters to be optimized ($\mathbf{Q}$, $\mathbf{R}$, α_Q and α_R) are selected to ensure the numerical stability of the first CKF iteration. Subsequent iterations rely on at least one valid

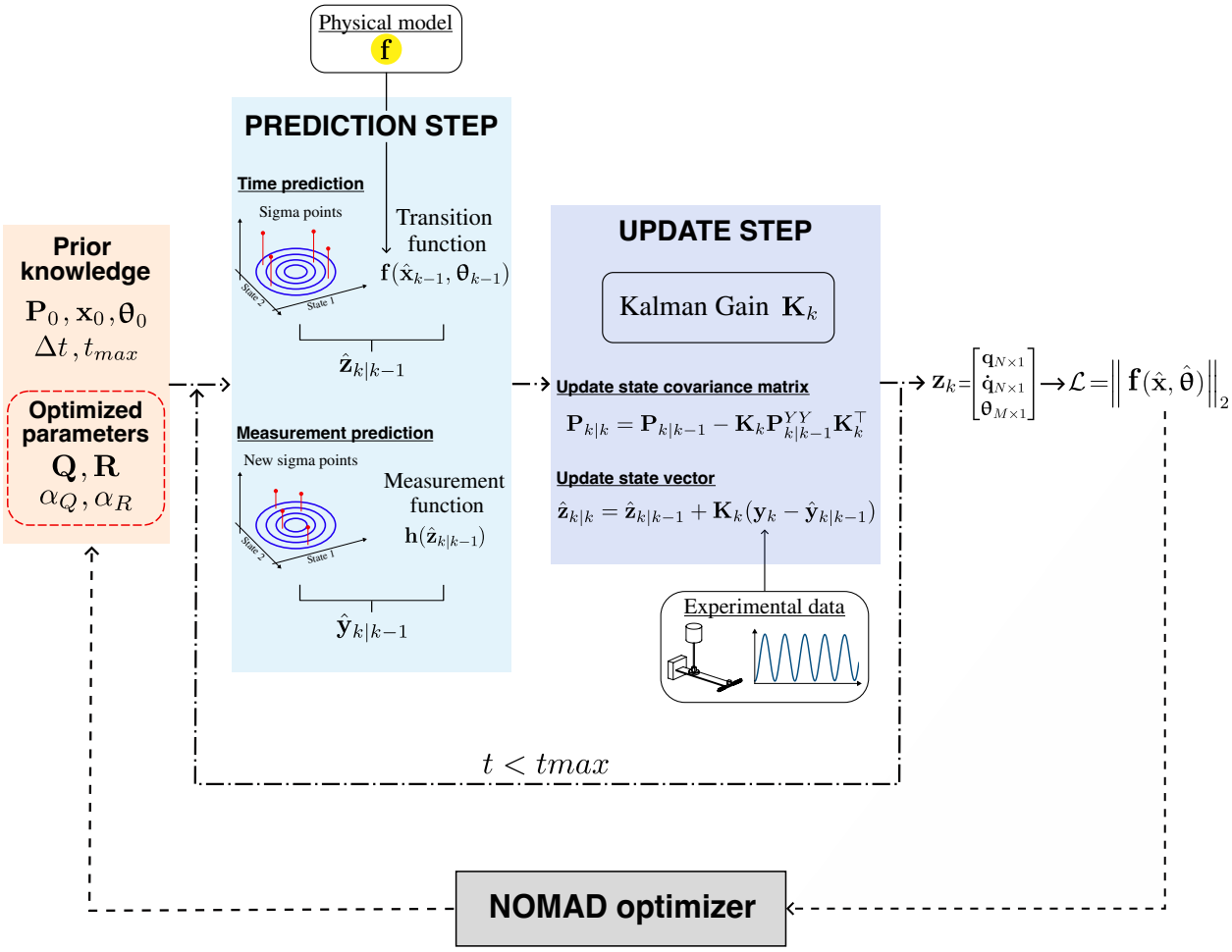

Figure 5.1 **Schematic of the CKF framework.** Based on the prior knowledge, the CKF estimates the augmented state space vector $\mathbf{z}$ (-·-·-). While $t < t_{max}$, CKF estimates both states $\hat{\mathbf{x}}$ and parameters $\hat{\theta}$, from the mathematical model Ω, during the prediction step. Then it updates the estimation according the the measurement $\mathbf{y}$. Running multiple CKF iterations, NOMAD subsequently optimizes the process and noise covariance matrices and their forgetting factors $(\mathbf{Q}, \mathbf{R}, \alpha_Q, \alpha_R)$ by minimizing the physical loss $\mathcal{L}$ (- - - -)

loss function, so the filter may encounter errors after this point. The time step Δt between two increments of the CKF is the same as the experimental measurement. The LabVIEW setup records the data with a constant sampling frequency of 2048 Hz so $\Delta t = 4.88 \times 10^{-4}$ s.

Then the CKF operates through its two usual steps: prediction and update. During the prediction step, the filter predicts the states, and generates a set of $2n$ sigma points with n the dimension of the augmented state vector. The nonlinear transition function $\mathbf{f}$ propagates each sigma point by integrating the physical model's differential equations (4.14) over the time step, which is discretized using fourth-order Runge-Kutta scheme. After propagation, the filter applies appropriate weights to the sigma points and sums them to calculate the predicted state vector $\hat{\mathbf{z}}_{k|k-1}$ and the associated covariance matrix $\mathbf{P}_{k|k-1}$. Next, the CKF proceeds with the measurement prediction, executing the same procedure: it generates a new set of sigma points and propagates them through the measurement function $\mathbf{h}$ describing the link between the physics and the sensor output, in this case, the acceleration measured by the accelerometer at the beam tip. The CKF calculates the innovation covariance matrix and the cross-covariance matrix between the predicted states and the predicted measurement to compute the Kalman gain during the update step. The filter then compares the predicted measurement $\hat{\mathbf{y}}_k$ with the actual sensor data $\mathbf{y}_k$, weights the difference with the Kalman gain and updates the state estimate $\mathbf{z}_k$ and the covariance matrix $\mathbf{P}_k$. This two steps iterative procedure repeats for each experimental data points.

According to the methodology developed by Ghorbani et al. (2025), the NOMAD algorithm optimizes a physics-aware loss function to tune the filter without a tedious trial and error approach. This loss function ensures that the estimates of the CKF align with the mathematical model. Then the physical system is accurately described and the physics-based prediction requires only minimal Bayesian correction to converge to the correct values. To compute the following loss, the estimated modal displacements, velocities, accelerations, and the stiffness coefficients are substituted into the system's equation of motion (4.14):

$$\begin{aligned} \underset{\substack{\mathbf{Q}=Q_0\cdot\mathbf{I},\\ \mathbf{R}=R_0\cdot\mathbf{I},\\ \alpha_Q,\,\alpha_R}}{\text{minimize}} \quad & \mathcal{L} = \left\|\mathbf{f}(\hat{\mathbf{x}}, \hat{\boldsymbol{\theta}})\right\|_2 = \left\|\mathbf{M}\ddot{\mathbf{q}} + \mathbf{C}\dot{\mathbf{q}} + \mathbf{K_L}\mathbf{q} + \mathbf{K_{NL}}\mathbf{q}^3 - \mathbf{F}\right\|_2 \\ \text{subject to} \quad & Q_0,\ R_0 \in [10,\ 10^{-7}] \\ & \alpha_Q,\ \alpha_R \in [0,\ 1]. \end{aligned} \tag{5.2}$$

Ideally the loss should be zero when the model perfectly describes the physical system but due to modeling inaccuracies and estimation errors, a residual arises. The loss function quantifies this discrepancy applying the L2 norm to the residual vector. The diagonal values of the pro-

cess and measurement noise covariance matrices Q_0 and R_0 well as their forgetting factors, are optimized. NOMAD iteratively runs the CKF with different process and measurement noise characteristics within bounded domains, $Q_0, R_0 \in [10^1, 10^{-7}]$ and $\alpha_Q, \alpha_R \in [0, 1]$ to minimize the physics-aware loss. We also check that the estimated states and parameters are not equal to zero to avoid the trivial solution. To maintain consistency across NOMAD iterations the CKF always run with the same set of experimental sensor data and initial state and covariance matrix values. To study the response of the beam to harmonic excitation, we apply NOMAD on a case with a single excitation frequency and obtain a set of optimized parameters reused for other excitation conditions. Restricting the tuning to one representative scenario reduces computational cost and is consistent with practical concerns discussed by Ghorbani et al. (2025).

5.2 Parameter estimation with synthetic data

To test and verify the method, the measured data are simulated with the mathematical model of the cantilevered beam, and incorporated to the CKF. We generate synthetic experimental data by integrating the nonlinear cantilevered beam equation of motion (4.14) in the time domain with the fourth-order Runge-Kutta method. The simulated acceleration of the beam tip is the synthetic sensor measurement incorporated into the CKF over a period of 20 seconds at a sampling frequency of 2048 Hz. A white noise of 15 % is added to the synthetic acceleration to approximate real-world conditions. Unlike the real experimental setup, we assume that in the synthetic experiments the beam is subjected to a perfect harmonic excitation force with a constant amplitude F_0. We simulate the system in similar conditions to the experimental setup considering the same parameters of the setup, described in Section 4.1. The linear and nonlinear spring stiffness values considered here differ slightly from those estimated experimentally in Section 4.2: $k_L = 136$ N/m and $k_{NL} = 1.37 \times 10^6$ N/m^3.

The aim of the CKF is to estimate the linear k_L and non linear stiffness k_{NL} of the system, knowing only the underlying mathematical model and the acceleration at the tip of the beam. The augmented state space vector is presented in Equation (5.1). Table 5.1 summarizes the initial values of the state vector and the covariance matrices, implemented in the CKF. The initial values chosen for the parameters are approximately 35% below the true value. The diagonal of the initial covariance matrix $\mathbf{P}_0$ is filled with the initial covariances $\mathbf{P}_{0,\mathbf{q}}$, $\mathbf{P}_{0,\dot{\mathbf{q}}}$, $\mathbf{P}_{0,k_L}$, $\mathbf{P}_{0,k_{NL}}$, given in Table 5.1. These values are chosen with trial and error and intuition. They reflect the uncertainty associated with the initial guess of the state and parameter estimates, and determine how broadly the filter searches around the initial guess, in order to refine the estimation. In this simulation study, the uncertainties are fully known, so tuning

Table 5.1 **Initial Values of states, parameters and variances, for the initialization of the CKF**

	Initial value	Variance: P_0
$\mathbf{x}_{0,\mathbf{q}}$	0.001	10^{-4}
$\mathbf{x}_{0,\dot{\mathbf{q}}}$	0.01	10^{-4}
k_L	80	10^4
k_{NL}	890000	10^{12}
	Initial value	Forgetting factor: α
$\mathbf{Q}$	$10^{-7} \cdot \mathbf{I}_{8\times 8}$	1
$\mathbf{R}$	$10 \cdot \mathbf{I}_{1\times 1}$	1

the covariance parameters with NOMAD is unnecessary. The measurement noise covariance $\mathbf{R}$ is a scalar because the acceleration is the only available measurement. A value of $\mathbf{R} = 10$ is chosen to incorporate noisy measurements. In this simulation study, as we are confident that the model accurately represents the system, we assume a diagonal process noise covariance matrix $\mathbf{Q}$, and we choose $\mathbf{Q} = 10^{-7} \cdot \mathbf{I}_{8\times 8}$. As the model embedded in the filter matches the system that generates the data, there is no need to adjust the values of $\mathbf{Q}$ and $\mathbf{R}$ during the iterations. The forgetting factors are set to 1 so that $\mathbf{Q}$ and $\mathbf{R}$ remain constant.

Figure 5.2 presents the parameter and state estimation results obtained with the CKF, when the nonlinear beam shown in Figure 5.2 (a) is excited by harmonically, with a frequency of $\Omega_e = 14$ Hz, and a force amplitude of $F_0 = 15$ N. In this case, k_L and k_{NL} are simultaneously identified, with respective estimation errors of 0.05% and 0.7%, compared to the true values. In addition to showing the evolution of the parameter estimates over the first 5 seconds, Figure 5.2 (b),(c) also illustrate the corresponding 3σ uncertainty interval (pale halo), derived from $\mathbf{P}$. In addition to the parameters, CKF also identifies the states of the system. The estimated acceleration, velocity and displacement, at the tip of the beam, are compared with the ground truth synthetic signals, respectively in Figure 5.2 (d),(e),(f). Despite the presence of white noise, the filter accurately reconstructs the acceleration and suppresses the noise. The Normalized Root Mean Square Error (NRMSE) of the estimation is 0.29 % for the deflection and 0.18 % for the velocity, so the CKF provides an accurate reconstruction of the unmeasured states. Moreover, the filter is not limited to estimation at the beam tip: it can reconstruct the state variables at locations where no sensors are available, thus acting as a virtual sensing tool.

In the specific case of the nonlinear beam excited by a harmonic force with a frequency of 14 Hz and a force amplitude of 15 N, the CKF is able to estimate accurately both states and

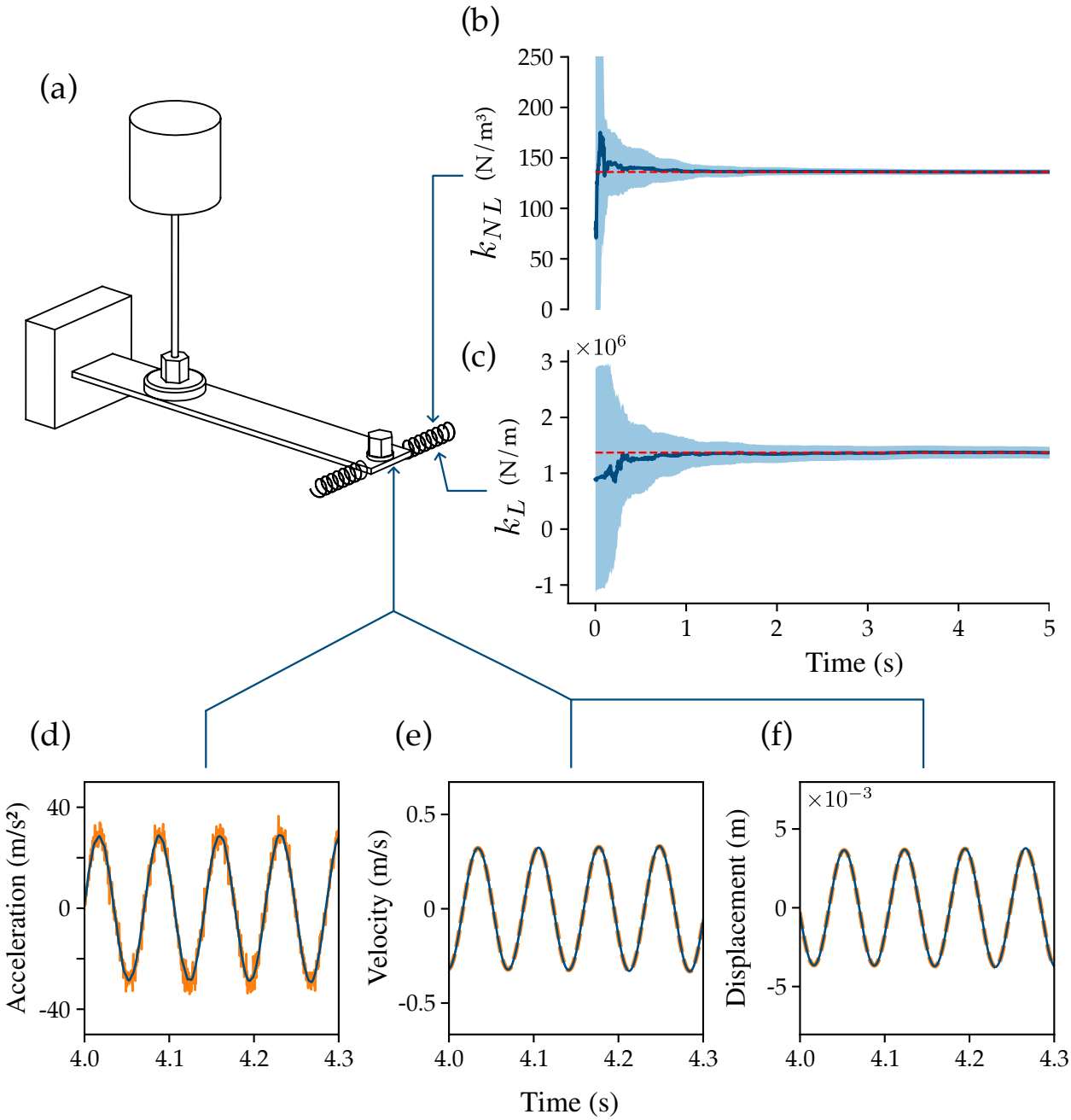

Figure 5.2 **CKF state and parameter estimations from synthetic acceleration data**, when the beam is subjected to an harmonic excitation 15 N and 14 Hz. **(a)** 3D schematic of the nonlinear beam with the springs. **(b), (c)** Respectively, CKF estimation (——) of the nonlinear stiffness k_{NL} and the linear stiffness k_L, compared to the true value (- - - -), during the first 5 seconds. The shadow represents the 3σ uncertainty interval of the estimate. The CKF also estimates the states: it reconstruct the true acceleration form the noisy measurements **(d)** and estimates the velocity **(e)** and the deflection **(f)**

parameters. Then, to generalize, we examined the performance of the filter over a range of excitation frequencies and force amplitudes. These parameters can be varied experimentally to control the beam's response. We vary the excitation frequency and force amplitude to evaluate the filter's ability to estimate the parameters for beam tip displacements ranging from 7×10^{-4} m and 1×10^{-2} m, across 19 test cases. For each case, the filter is initialized according to Table 5.1. The shaker's location is kept constant (as close as possible to the fixed end of the beam), to minimize unwanted interactions between the beam and the shaker. For each test case, data are simulated with the equation of motion of the beam (4.14) and the CKF estimates the parameters with the noisy acceleration as measurement data.

For each excitation condition and tip displacement, the filter successfully estimates the unknown displacement and velocity and reconstructs the acceleration. We focus on the estimation of the unknown parameters k_L and k_{NL}. Figure 5.3 (b) shows the relative error between the estimated value and the ground truth for both linear k_L and nonlinear stiffness k_{NL} as a function of beam tip displacement amplitude. The tip displacement corresponds to the limit cycle reached for specific excitation force and frequency values, and directly affects the magnitude of the nonlinear force term according to the beam's equation of motion (4.14). Figure 5.3 (a) illustrates how the forces associated with the linear and nonlinear stiffness vary with tip displacement. Since the nonlinear force scales with the cube of the displacement, its contribution drops rapidly as displacements decrease. If the displacement amplitude is below 0.004 m, the cubic force is almost null: less than 0.2 N.

The ability of the CKF to estimate k_L is independent of the displacement amplitude, with a mean relative error for all tested cases of 0.8 %. In contrast, accurate estimation of k_{NL} strongly depends on amplitude. When the tip displacement is below 0.004 m, the percentage error in estimating k_{NL} exceeds 5 %, reaching up to 35 % for displacements under 0.003 m. The the estimated values of k_{NL}, for each displacement values, are plotted in Figure 5.3, with their associated 2σ uncertainty intervals. When the tip displacement is below 0.003 m the filter is unable to estimate k_{NL}. Its output remains close to the initial value assigned during initialization, rather than converging towards the true value. In such cases, the associated uncertainty interval grows significantly, often exceeding twice the excepted nonlinear stiffness. This indicates that the filter lacks sufficient information and cannot reliably identify the parameter under the given conditions.

Conversely, as the displacement amplitude increases, the error in estimating k_{NL} decreases and falls below 1 %. Between 0.003 m and 0.005 m of tip displacement, the CKF identifies accurately k_{NL}, but the uncertainty around the estimate remains relatively large, indicating that while the filter captures the true value, it is not fully confident (Figure 5.3 (c)). In

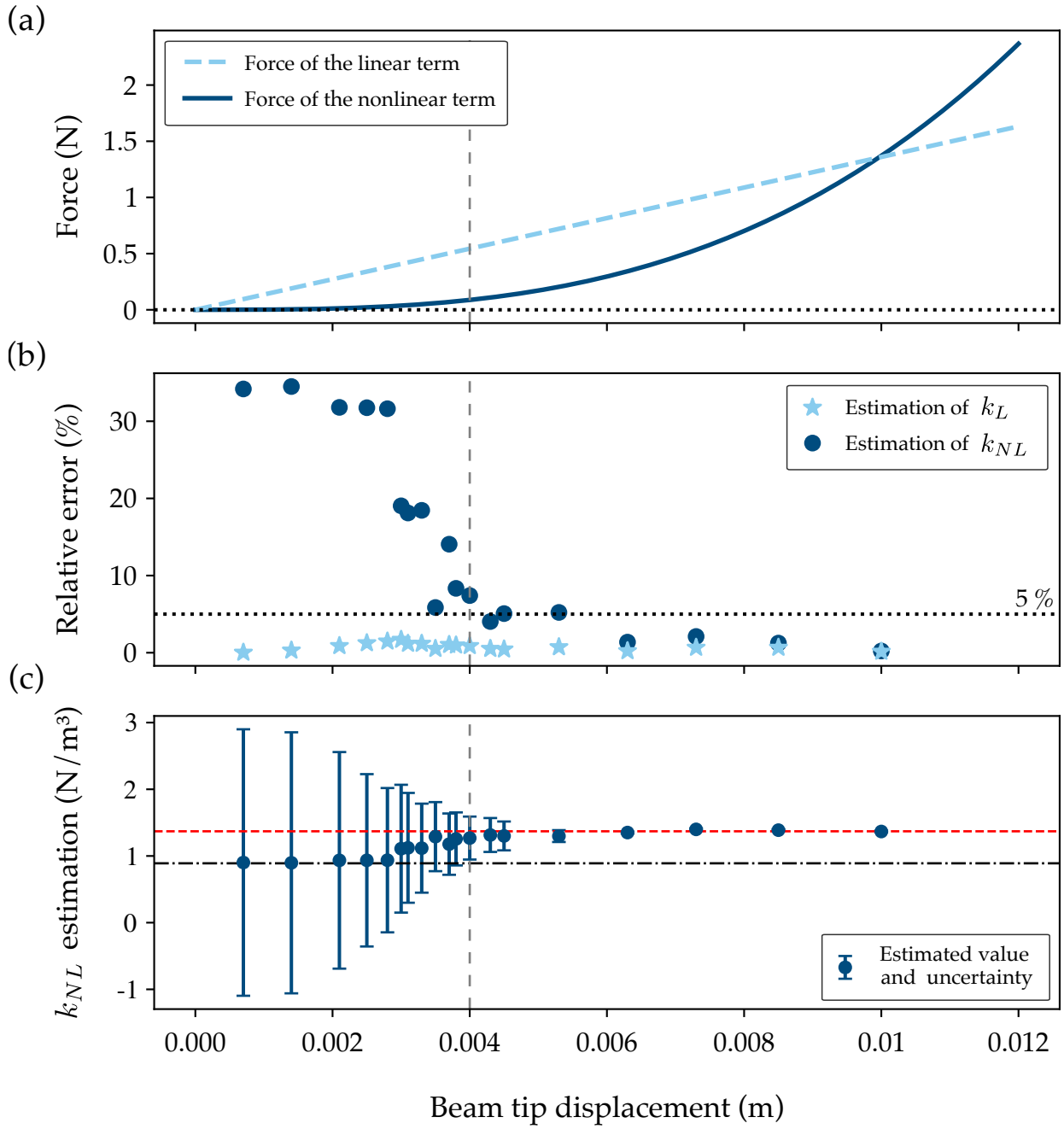

Figure 5.3 **Ability of the CKF to estimate the linear and nonlinear stiffness (k_L et k_{NL}) as a function of the displacement amplitude at the tip of the beam. (a)** Force contribution of the linear (- - - -) and nonlinear terms (——) of the beam's equation of motion (4.14) as a function of tip displacement. **(b)** Relative estimation error of the CKF for linear (★) and nonlinear (◯) stiffness parameters as a function of the displacement amplitude at the beam tip. **(c)** Estimated nonlinear stiffness coefficient k_{NL} as a function of tip displacement, with associated 2σ uncertainty interval (◯). The estimations are compared with the expected value (- - - -) and initial value (-·-·-) of k_{NL}

practical experimental conditions, additional model errors or measurement noise tend to increase the confidence interval, and makes accurate estimation challenging for the CKF. Then for displacements above 0.005 m, the errors become negligible, showing that the CKF estimates k_{NL} with high confidence. These results obtained with the CKF are consistent with those presented in Figure 5.3 (a), and they confirm that when the tip displacement is too small, the nonlinear term has little influence on the system's dynamics and the CKF cannot accurately estimate its value. A minimal tip displacement amplitude of 0.004 m is necessary for the nonlinear term to significantly influence the behavior of the beam and for the CKF to successfully identify its value.

In summary, the CKF enables joint estimation of both states and unknown parameters of the nonlinear beam, with only a single point acceleration measurement. It consistently provides accurate estimates of the linear stiffness, regardless of the tip displacement amplitude, and accurately estimates the nonlinear stiffness when the displacement is sufficiently large. Even when the model in the CKF perfectly matches the measured data, if a parameter does not significantly influence the system dynamics, the CKF cannot estimate its value. Overall when the model and data are well aligned, the CKF estimates accurately states and parameters and is also effective in filtering out measurement noise. Conducting simulation study demonstrate that the estimation framework presented in Section 5.1 is robust to various conditions and implemented without errors, ensuring reliable results with experimental data.

5.3 Parameter estimation with experimental data

Following the verification of the CKF framework in the synthetic data study, the next step is to validate the method on a physical vibrating system, and investigate its performance in estimating parameters, directly from measured vibration data. The experimental study focuses on two beam configurations: the baseline linear cantilevered beam without the springs and the nonlinear beam with the perpendicular springs (Figure 4.1). In both configurations, the experimental data, obtained from acceleration measurements, provide the measurement data for the CKF estimation procedure. The mathematical model within the filter incorporates the measured force as the external forcing term. For the linear beam, the objective is to estimate the mass of the attached magnet and force sensor m_S, as well as the intrinsic bending stiffness EI. We want to compare the estimated value of EI with the values presented in Table 4.3. In the nonlinear configuration, we consider the modified model described in Section 4.5.2, which has been fitted to the linear beam data. Then the objective is to estimate both the linear and nonlinear stiffness and assess if we can identify of the new boundary condition. Beyond confirming its accuracy in identifying physical unknowns properties of both linear

and nonlinear beams, the objective is to validate the CKF as a practical method for solving inverse problems and enabling joint estimation in real nonlinear vibrating systems such as the bearings of a hydraulic turbine shaft line.

5.3.1 Configuration 1: The linear cantilevered beam, without the springs

We first consider the additional mass introduced by the magnet and the force sensor m_S, as the single unknown parameter. The augmented state-space vector has a dimension of 7×1. We compare the CKF estimation of the mass with the reference value $m_S = 0.115$ kg obtained by scaling the mass. For this test case, the experimental data incorporated into the CKF, were obtained with the shaker positioned at $L_S = 0.38$ m, closer to the free end of the beam, to increase the displacement at the beam tip. Although this location is not the final intended position for the shaker, it allows us to validate the NOMAD algorithm for effective tuning of the CKF's initial parameters. At $L_S = 0.38$ m we also ensures that the added mass has a significant impact on the beam's dynamics.

The filter is initialized following the same procedure as in the simulation study. The unknown parameter initial guess: $m_{S,0} = 0.07$ kg, is chosen with a bias of approximately 35 % from the ground truth. The initial states and their corresponding covariance values are assigned as specified in Table 5.1. The initial covariance matrix is assumed to be diagonal. We set the initial covariance of the parameter to $P_{0,m_S} = 10^{-2}$. This value must be set high enough to ensure that the filter captures the parameter correctly. Setting the covariance too large may reduce estimation accuracy, while setting it too small prevent the filter from searching the parameter space sufficiently, possibly leading to estimation bias or failure.

Considering experimental data involves unknown levels of process and measurement noise. The NOMAD algorithm tunes and optimizes the initial covariance matrices $\mathbf{Q}_0$, $\mathbf{R}_0$, and their forgetting factors α_Q and α_R, as described in Section 5.1. NOMAD searches over these parameters by running consecutive CKF evaluations to minimize the physics-aware loss. The filter's integration time step is set to match the measurement data acquisition frequency of 2048 Hz. These data are recorded from the linear beam excited by a harmonic signal with a frequency of 18 Hz and a shaker input voltage of 150 mV. We initialize the first CKF in NOMAD assuming $\alpha_Q = \alpha_R = 1$, and setting all the diagonal values of $\mathbf{Q}$ as 10^{-1} and $\mathbf{R}$ as 10^{-4}. Each NOMAD trial runs the CKF for 25,000 iterations, equivalent to approximately 12 s of experimental measurement. NOMAD obtains the minimum physics-aware loss after $it_{opt} = 32$, trials out of 120 possible evaluations, and the bests parameters are: $\mathbf{Q}_0 = 0.06 \cdot \mathbf{I}_{7\times7}$, $\mathbf{R}_0 = 1 \times 10^{-7} \cdot \mathbf{I}_{1\times1}$, $\alpha_Q = 0.975$, $\alpha_R = 0.941$. The results of the optimization and the associated CKF estimations of m_s are presented in Figure 5.4.

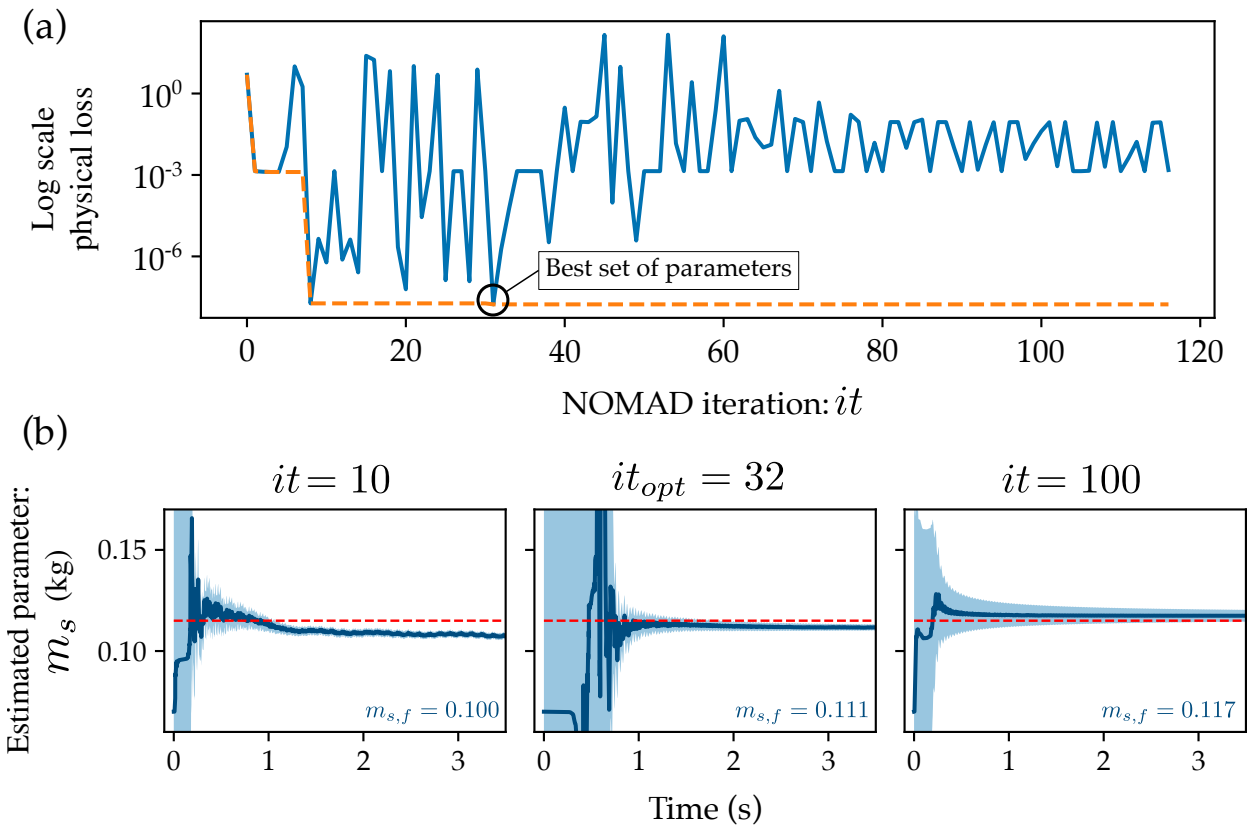

Figure 5.4 **NOMAD optimization process with associated CKF parameter estimation**, under experimental sine excitation at 18 Hz with an input voltage of 150 mV. **(a)** Physical loss of the CKF estimation as a function of the NOMAD iteration i. **(b)** Estimated parameters at different iteration steps (——), with their 3σ uncertainty intervals (shadow), compared to the true value (- - - -)

Figure 5.4(a) shows the evolution of the physical loss across all NOMAD trials, highlighting the trial with the best parameter set. The dashed line illustrates the convergence of the optimization process, decreasing from a maximum physical loss of 1.46×10^2 and converging to a minimum of 1.71×10^{-8} at $it_{opt} = 32$. Figure 5.4(b) specifies intermediates parameter estimates at trials $it = 10$, $it = 100$, and the parameter estimation obtained with the optimized set at trial $it_{opt} = 32$. Before NOMAD algorithm reaches convergence, such as at $it = 10$, the parameter estimates do not yet achieve sufficient accuracy. Even if the loss is 4.45×10^{-6}, the relative error in the CKF parameter estimation remains high, at 12.1 %. With the optimal set of parameters at $it_{opt} = 32$, the CKF accurately estimates m_S with a relative error of 3.5 %. The CKF successfully reconstructs the measured acceleration, with a NRMSE of 3.2 %. We cannot assess of the accuracy of the estimated deflection and velocity, because these quantities are not measured in the experimental setup.

Although NOMAD optimizes the physics-aware loss function, the best parameter set is not the only one yielding good results for the estimation of m_S. Sometimes, the estimation of m_S demonstrates comparable or even better accuracy, for example at iteration $it = 100$ (Figure 5.4(b)). With $\mathbf{Q}_0 = 1 \times 10^{-3} \cdot \mathbf{I}_{7\times7}$, $\mathbf{R}_0 = 1 \times 10^{-7} \cdot \mathbf{I}_{1\times1}$, $\alpha_Q = 0.90$, $\alpha_R = 0.9999$, the physical loss is 1.41×10^{-2}, and the relative error of the CKF estimation is 1.7 %, which is lower than that achieved with the optimal parameter set. However, the normalized RMSE of the predicted acceleration in this case is slightly higher at 3.5 %, which can explain the larger physical loss despite the better parameter estimation accuracy. These observations suggest that while NOMAD effectively tunes parameters to achieve accurate estimation, multiple combinations of $\mathbf{Q}_0$, $\mathbf{R}_0$, α_Q, α_R, may provide acceptable solutions when balancing loss minimization and prediction accuracy.

The CKF struggles to reliably distinguish and estimate parameters when their impact is insufficient, as illustrated Section 5.2. When the shaker is positioned near the fixed end of the beam, the first beam mode shape have lower amplitudes at that location, causing m_S to contribute less to the overall mass matrix. As a result, its influence on the beam's dynamic behavior is reduced compared to when the shaker is located closer to the free end, which was therefore chosen to estimate m_S. In the nonlinear case, however, interactions between the beam and shaker altered the desired nature of the nonlinearity. Then, to mitigate these side effects in the rest of the study, we repositioned the shaker nearer the fixed end at $L_S = 0.085$ m, despite it reducing the free-end displacement.

The intrinsic bending stiffness of the beam (Young's modulus E times moment of inertia I), is a very important parameter in the system modeling, as it significantly affects the dynamic behavior of the beam, especially the natural frequencies. This parameter is also often unmeasurable directly in complex mechanical systems. Even in our setup, the effective bending stiffness is difficult to determine precisely. Three different values are obtained from three approaches: the stiffness calculated from the beam geometry $EI_{th,geom}$, the stiffness estimated experimentally $EI_{th,exp}$ as described in Section 4.2.1, and the corrected stiffness used in the linear model to fit the data EI_{corr} (Section 4.5.1). Therefore, without a precise ground truth for this value to include in the model, accurate estimation of EI with the CKF becomes critical.

The CKF estimates jointly EI and the states, with the shaker positioned at $L_S = 0.085$ m. The filter incorporates the beam's response to two different input signals. The first signal is a harmonic excitation at 15 Hz with an input voltage of 150 mV, meaning the beam is excited far from its resonance frequency. The second signal is a multi-frequency linear chirp excitation that sweeps frequencies from 9 Hz to 11 Hz and back to 9 Hz, repeated three

times over a duration of 60 seconds, with an input voltage of 100 mV. Figure 5.5 presents the results of the CKF. For the two cases presented in Figure 5.5, the values implemented in to initialize the CKF are summarized in Annex A, Table A.1.

For the harmonic signal, the CKF estimates $EI = 21.3$ Nm^2, whereas the expected value, calculated from the beam's geometric properties, is $EI_{th,geom} = 16.15$ Nm^2 and the experimental value is $EI_{th,exp} = 16.69$ Nm^2, resulting in a relative error of 31.8 % and 27.6 %, respectively (5.5 (a)). This comparison with the expected values is difficult to interpret because we don't precisely know the true value of EI. However, we identified experimentally the first natural frequency of the beam at 9.8 Hz. When the EI estimate obtained from harmonic experimental data is inserted into the model, the resulting natural frequency is 11.4 Hz, leading to a relative error of 16.3 %. This substantial deviation reflects the poor quality of the estimation.

Figure 5.5 (b), (c) present the results of estimating EI with the CKF, for the chirp signal. With a multi-frequency input signal the CKF converges to $EI = 15.3$ Nm^2. Incorporating this value into the model yields a first natural frequency of 9.7 Hz, which corresponds to a relative error of about 1 % compared to the experimental value. While we cannot directly verify if the amplitude of the deflection and velocity are accurately estimated, the filter successfully detects the resonance region, and the increase in amplitude in this region is visible in the reconstructed states, as shown in Figure 5.5 (c). The reconstructed acceleration matches the experimental measurements with a NRMSE of 4.8 %. Although the CKF does not have memory like artificial intelligence methods, sweeping through the resonance region enables the filter to adjust the covariance matrix $\mathbf{P}$. The resulting uncertainty band around the estimated parameter is relatively wide and includes $EI_{th,geom}$. However, the chosen values of process and measurement noise covariance matrices $\mathbf{Q}$ and $\mathbf{R}$, strongly influence the estimation of the uncertainty. In this study, the filter parameters are tuned to achieve convergence to a final value, but the true values of $\mathbf{Q}$ and $\mathbf{R}$ cannot be accurately determined from the available data.

The difficulties of estimating EI in the case of the harmonic signal can be due to several factors inherent in the nature of inverse problems. Firstly, the modeling error between the mathematical model in the filter, and the real experimental data is a very important factor and have a big impact on the estimation of the parameters. Because the CKF is model-based, its ability to estimate unknown parameters relies heavily on how well the model captures the true dynamics of the beam and describes properly the experimental data. Inverse problem are also highly sensitive to model uncertainties and errors. When the discrepancy is too large, the algorithm tends to minimize the difference between the model and the

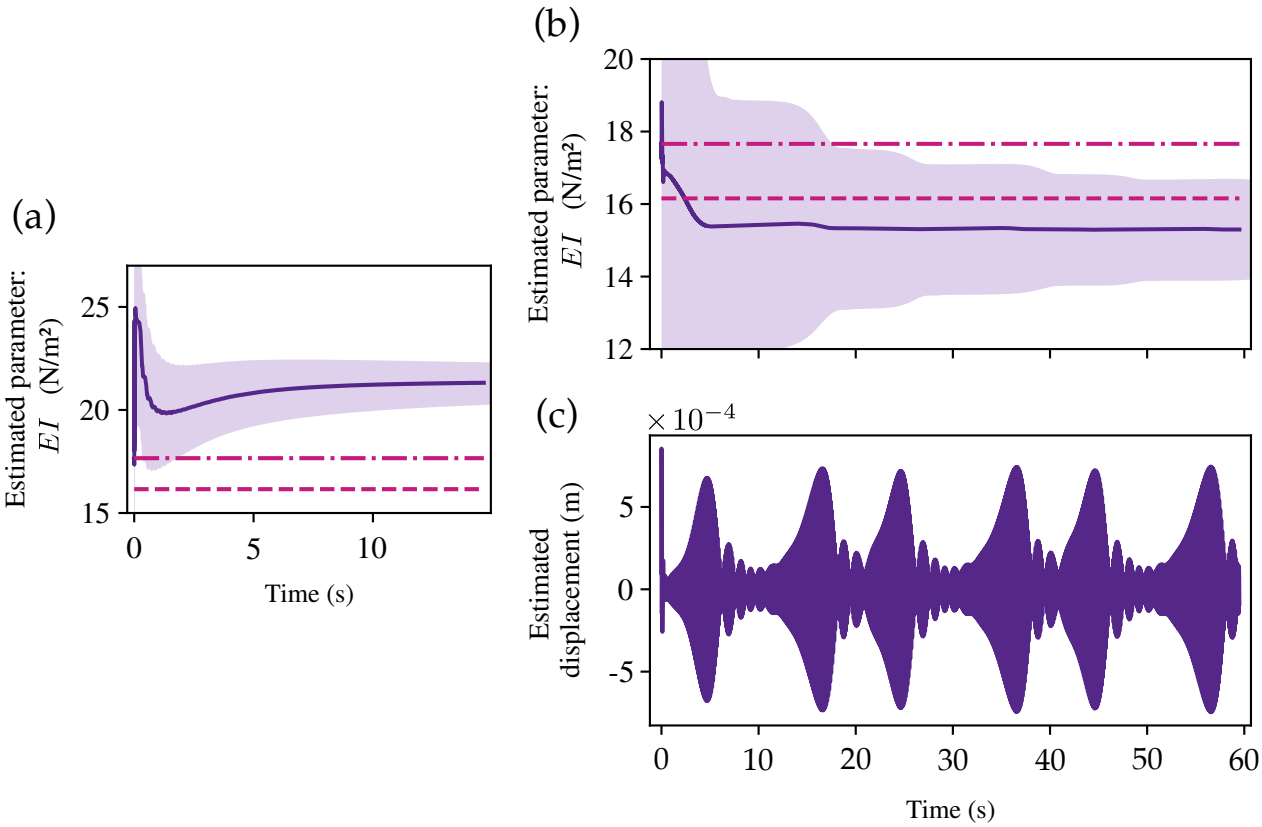

Figure 5.5 **CKF estimation of the intrinsic stiffness of the beam EI for different input signals.** **(a)** Under sine excitation at 15 Hz with an input voltage of 150 mV. **(b)** Under a chirp excitation with a cyclic frequency sweep from 9 Hz to 11 Hz and back to 9 Hz, repeated 3 times over 60 seconds. In both cases, the estimated parameters (——) are compared with the bending stiffness obtained with geometrical parameters (- - - -), and with the experimental value obtained from static tests (–·–·–). The shaded area represents the 3σ uncertainty interval. **(c)** Reconstructed tip displacement of the beam under chirp excitation

data rather than accurately identifying the true parameters. Another major challenge is to uniquely identify the true parameter values, especially when several different parameter values can produce similar system responses. The CKF can become trapped in a local minimum, producing the correct output amplitude with the wrong combination of parameters, rather than truly matching the physical system. The more unknown parameters there are, the higher the chance of having multiple mathematically possible solutions, which makes parameter identification more complicated.

Consequently, reliable parameter estimation in such scenarios, often requires additional constraints, high-quality data, or regularization techniques to reduce the number of potential solutions and improve identifiability. Carefully incorporating prior knowledge is the simplest and the first regularization strategy. By incorporating reasonable assumptions about the

expected solution, prior knowledge can make estimation more stable, and guide the identification of parameters. It can also mitigate the non-uniqueness and sensitivity to measurement noise. To maximize the ability of the filter accurately estimating, we initialize the bending stiffness with the experimental value obtained with the static tests $EI_{th,exp} = 16.69$ Nm^2, and we set the initial displacement and velocity to be within the order of magnitude of anticipated system behavior. Moreover, the initial values of the process and noise covariance matrices as well as their forgetting factors ($\mathbf{Q}$, $\mathbf{R}$, α_Q, and α_R), play a critical role in ensuring reliable filter convergence. As demonstrated in Figure 5.4 (a), certain parameter choices may cause the physical loss to increase significantly, leading to incorrect estimates. The NOMAD algorithm helps to address this issue to tune $\mathbf{Q}$, $\mathbf{R}$. However, in this case, we opted not to consider forgetting factors and set both α_Q, and α_R to 1, in order to maintain constant noise and process covariance matrices.

In the case of estimating EI, carefully initializing the filter is not enough. An incorrect estimation of EI results in an inaccurate natural frequency. When the beam is excited at 15 Hz with a sinusoidal input, the filter lacks enough information about the natural frequency because a purely harmonic signal does not provide enough vibration content (Figure 5.5 (a)). Consequently, when the value of EI is estimated with a harmonic signal, the predicted first natural frequency of the beam differs from the experimental value by 16.3 %. Exciting the system with a multi-frequency signal, sweeping around the natural frequency, resolves this issue, explaining the improved estimation accuracy.

5.3.2 Configuration 2: The nonlinear cantilevered beam

After developing and refining the linear model to best replicate the behavior of the linear cantilever beam analogous to a healthy hydraulic turbine shaft line, the next step is to estimate the new unknown parameters of a worn or damaged nonlinear bearing of the same turbine. In our case, we introduce a nonlinear boundary condition by adding the spring system with the aim of estimating both the linear k_L and nonlinear stiffness k_{NL} coefficients with the CKF. As discussed in Section 5.1, the CKF estimates the state space vector (5.1) and its state covariance matrix $\mathbf{P}$ by combining the experimental data and the previously developed model.

As demonstrated in the synthetic data study, when the displacement at the tip of the beam is too small, the nonlinear term does not sufficiently influence the system dynamics. In this case, it becomes impossible to estimate the associated nonlinear stiffness coefficient. Therefore, we apply the CKF within the first natural frequency region, characterized by the maximum amplitude of vibration. To maximize the information available to the filter, the

CKF estimates parameters under multi-frequency excitation. We consider a chirp signal that sweeps linearly through the resonant frequency range, from 8 Hz to 13 Hz, over 60 seconds, corresponding to a frequency sweep rate of 0.083 Hz/s. The measured excitation force and accelerometer data at the end of the beam constitute the experimental input data for the CKF, recorded at a sampling frequency of 2048 Hz.

We initialize the state as well as and their corresponding covariance with the same values of the synthetic data study (Table 5.1). For the unknown parameters k_L and k_{NL}, covariance values are also retained from the synthetic data study and we initialize the filter with the experimentally obtained linear and nonlinear stiffness ($k_L = 138$ N/m; $k_{NL} = 1.22 \times 10^6$ N/m^3). Since these values are not precisely known, providing the filter with this informed prior knowledge aims to enhance its convergence to the correct values. The optimal initial process noise covariance and measurement noise covariance are $\mathbf{Q} = 10^{-6} \cdot \mathbf{I}_{7\times7}$ and $\mathbf{R} = 0.1 \cdot \mathbf{I}_{1\times1}$, respectively, with their corresponding forgetting factors $\alpha_Q = 1$ and $\alpha_R = 0.99$. Since $\alpha_Q = 1$, the process noise covariance matrix $\mathbf{Q}$ remains constant and does not update during the CKF iterations.

Figure 5.6 presents CKF-based estimation results for k_L, k_{NL} and the reconstruction of the acceleration at the tip of the beam. The CKF estimates the linear stiffness as $k_L = 50.8$ N/m, which deviates notably from the experimental value $k_{L,exp} = 138$ N/m. However, this estimate is close to the theoretical linear stiffness computed from geometric relations, $k_{L,th} = 47.5$ N/m, corresponding to a relative error of 6.9 %. The estimated nonlinear stiffness $k_{NL} = 9.95 \times 10^5$ N/m^3 deviates from both the theoretical and experimental values, with respective discrepancies of 21 % and 18 %. The filter underestimates the acceleration, especially at the resonance frequency. the NRMSE is 5.57 % close to the resonance region, where the CKF struggles the most to reconstruct the acceleration.

To validate the CKF estimation results, we compare them with additional experimental data. We simulate the nonlinear beam response to sinusoidal excitation at various frequencies within the resonance region, ranging from 7 Hz to 25 Hz, with finer frequency resolution near resonance. The measured experimental excitation force is input into the simulation. A fourth-order Runge-Kutta integration scheme solves the same mathematical model within the CKF algorithm, incorporating the estimated linear and nonlinear stiffness parameters. We compare the simulation results with the experimental data points shown in Figure 4.11. Figure 5.7 presents the steady-state amplitude of acceleration for both simulated and experimental data, along with the magnitude of the excitation force. Excluding the three anomalous points at 11.4 Hz, 11.5 Hz, and 11.6 Hz, the mean relative error between the simulated and experimental amplitudes is 3 %, indicating good agreement between the simulated data,

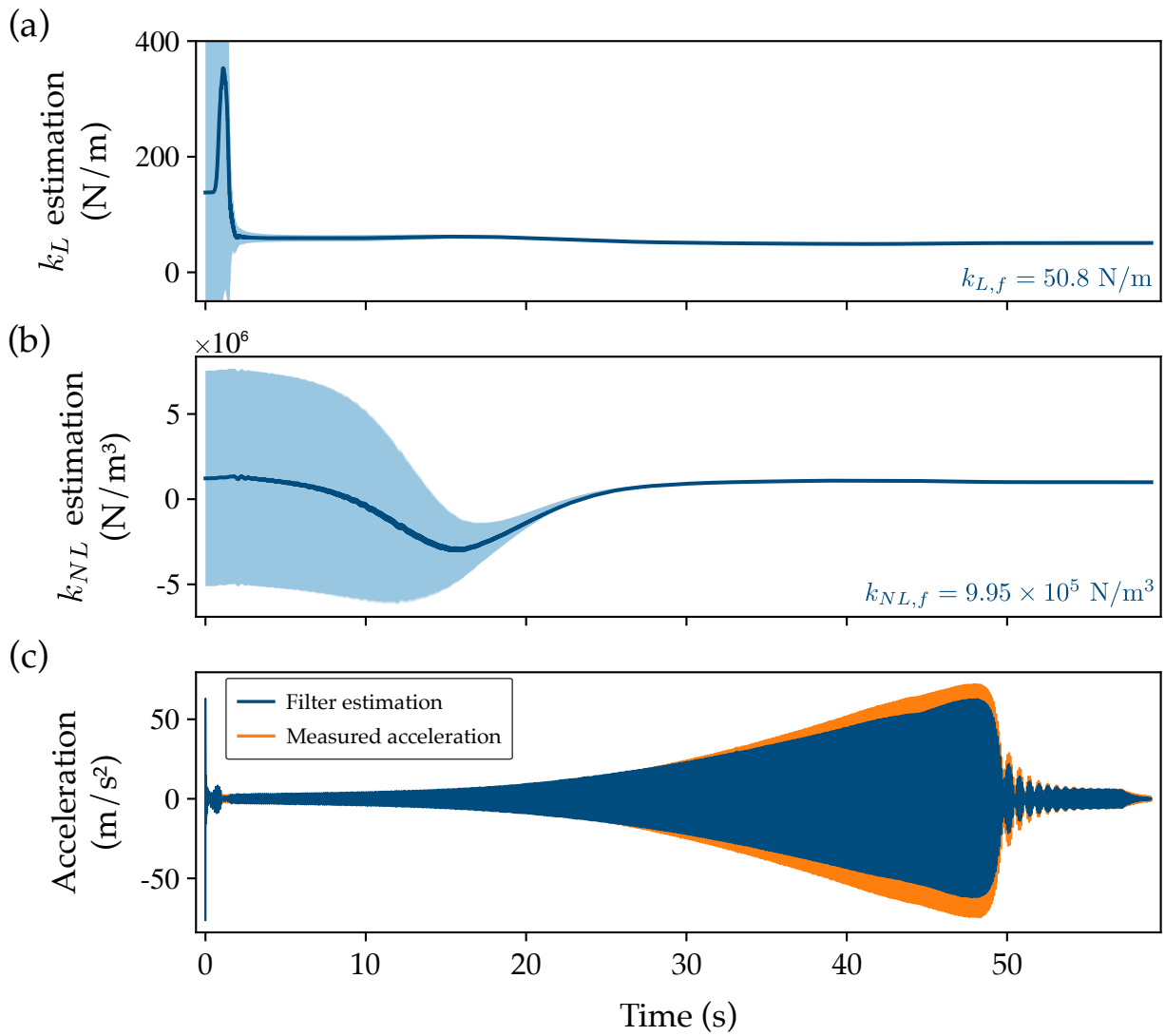

Figure 5.6 **CKF estimation results with the measured acceleration response at the tip of the beam under chirp excitation as the filter input signal.** **(a)** Time evolution of the estimated linear stiffness k_L. **(b)** Time evolution of the estimated nonlinear stiffness k_{NL}. The shaded regions around the estimated parameters represent the 2σ uncertainty intervals. **(c)** Comparison between the experimental acceleration and its CKF-based reconstruction

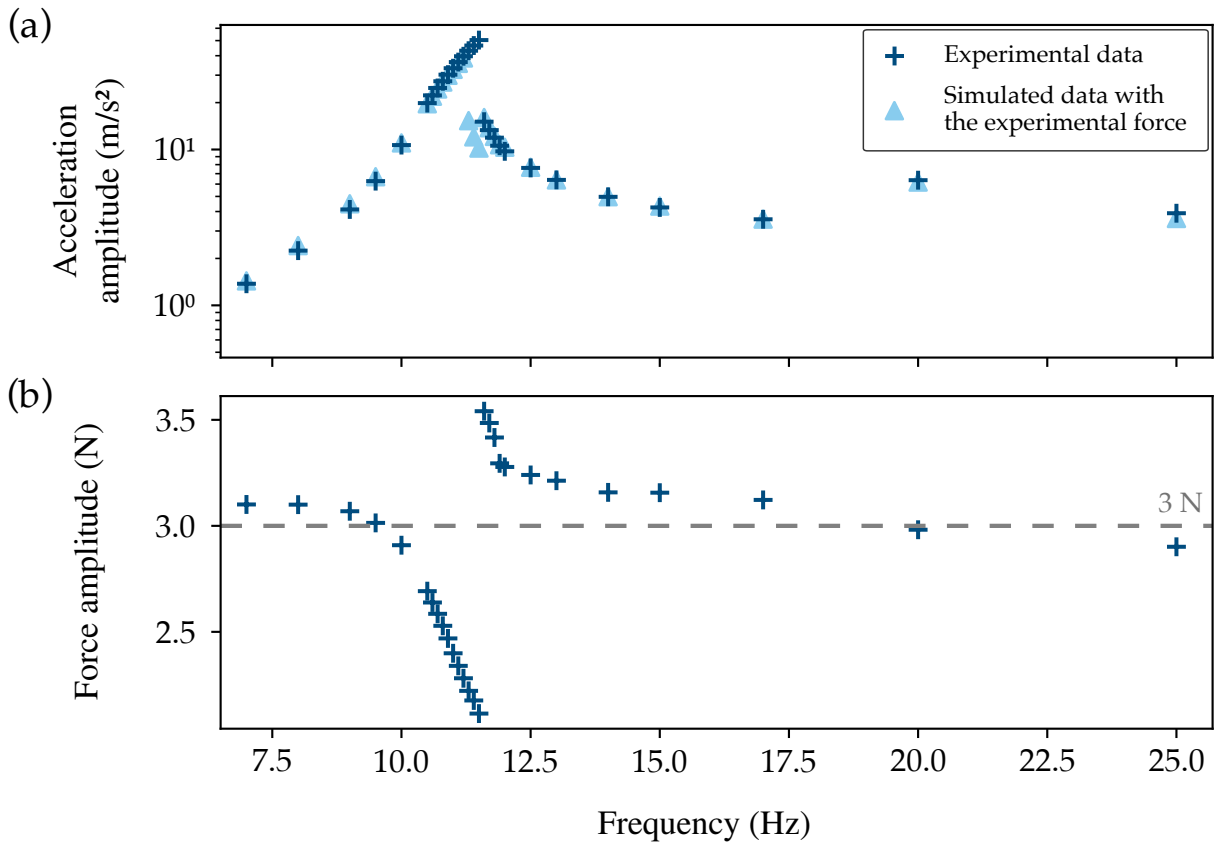

Figure 5.7 **Response of the nonlinear beam under harmonic excitation as a function of the excitation frequency in the resonance region.(a)** Comparison between the experimental steady-state acceleration amplitude and the simulated amplitude, considering the experimental force as input, and the estimated linear and nonlinear stiffness obtained from the CKF. **(b)** Amplitude of the experimental excitation force recorded by the force sensor at various frequencies

based on the estimated values of k_L and k_{NL}, and the experimental measurements.

With the two estimated values of k_L et k_{NL}, the model accurately reproduces the experimental frequency-acceleration amplitude curve, demonstrating the reliability of the estimates. The estimated linear stiffness value aligns well with the theoretical prediction. In the case of the nonlinear stiffness, a greater discrepancy is observed, and the filter converge to the theoretical value with around 20 % error. This raises the question: is the nonlinear stiffness well estimated, or is its influence on the system's dynamics too weak for the filter to accurately capture it? With a maximum deflection amplitude of 0.01 m estimated by the CKF at the resonance frequency, the nonlinear term should have a sufficient impact on the dynamics for the CKF to accurately estimate the nonlinear stiffness, as supported by the results presented in Section 5.2. However, verification of the estimated states is not possible due to the lack of corresponding measurements. Additionally, unlike the simulation study, the experimental context introduces measurement and modeling errors that significantly impact the CKF's estimation accuracy. Although the estimated nonlinear stiffness is consistent, we cannot validate it due to the limited degree of nonlinearity in the data, which introduces uncertainty.

CHAPTER 6 CONCLUSION

6.1 Summary of Works

In this work, we solve an inverse problem with the cubature Kalman filter. Based on the mathematical model and experimental data from the setup, the CKF estimates the states and unknown parameters of a cantilever beam to which a nonlinear spring system has been added.

Before estimating the linear and nonlinear stiffness added by the springs, we characterized the system's dynamic through modal analysis and static force displacement tests. These static tests confirmed that the spring system exhibit a cubic (Duffing-type) nonlinearity, characterized by a restoring force proportional to the displacement cubed. We also ensured that the acquired nonlinear dynamic data are clean and suitable before incorporating them into the CKF. A mathematical model describing the nonlinear behavior of the beam was developed and calibrated to accurately represent the dynamics of the linear cantilever beam, serving as an analog to a healthy hydraulic turbine shaft line.

We verify the presented CKF framework through a simulation study with synthetic data. In ideal conditions, without modeling errors and with known process and measurement noise covariances, the CKF accurately estimate the linear stiffness. The nonlinear stiffness can be reliably identified only when the nonlinear term is sufficiently large to have a significant influence on the system dynamics. Then, the NOMAD algorithm, which optimizes the initial covariance matrices and forgetting factors, is validated by estimating the combined mass of the force sensor and magnet with linear experimental data. Next, the CKF estimates the beam's intrinsic stiffness under both sinusoidal and chirp excitations, demonstrating the advantage of chirp excitation's multi-frequency content over purely sinusoidal signals when solving inverse problems. Finally, parameter estimation is performed on the nonlinear beam by incorporating clean experimental data and combining the developed linear model with nonlinear terms within the CKF framework. This process allows for accurate estimation of both linear and nonlinear stiffness coefficients, which are subsequently validated by comparing simulation results with experimental frequency response curves.

This work constitutes a first step towards building a digital twin of a hydraulic turbine shaft line. Our framework can identify nonlinear boundary conditions, analogous to a damaged bearing, by relying solely on a model calibrated for the linear beam (i.e. that of a healthy turbine) behavior and on nonlinear experimental data.

6.2 Limitations

In this work, accurate estimation of the nonlinear stiffness strongly depends on the degree of nonlinearity present in the experimental setup. Due to the constraints of the modal shaker excitation method, both the input voltage and the achievable shaker amplitude are limited, restricting the maximum beam tip displacement, particularly outside the resonance region. As a result, it is challenging to explore the beam's response at high vibration levels and to perform parameter estimation under stronger nonlinear conditions. Additionally, the shaker introduces undesired and unmodeled dynamics through interactions with the beam, potentially distorting the measurements. In summary, while inducing nonlinear behavior is straightforward, achieving controlled, repeatable, and well-characterized nonlinear behavior remains a significant challenge and requires careful attention to test procedure and setup.

In addition to the experimental constraints, accurately modeling the system proved challenging, because it demands high precision in measuring beam lengths and positions. Even minor discrepancies can significantly influence the system's dynamic response. Another difficulty concerns the accurate representation of the damping in the nonlinear cantilevered beam system. Its modeling appears to be more complex than initially assumed. Experimental observations suggest that the nylon thread attaching the springs introduces additional damping which may not be purely proportional, as assumed in the chosen Rayleigh formulation for modeling the structural damping of the beam without springs. A further limitation arises from the assumptions made in the reduced-order modeling. The Galerkin decomposition method relies on the mode shapes of the cantilevered beam without explicitly accounting for the influence of the mass of the accelerometer and the magnet and force sensor assembly. Similarly, we also neglected the effect of the perpendicular springs on the mode shape for the nonlinear system. These simplifications may result in slight deviations in the modal representation and in the overall accuracy of the reduced-order model.

These challenges are further amplified by the model-based nature of the CKF identification method, which heavily relies on the fidelity of the physical model. The accuracy of the parameter estimates depends heavily on the precision of the model and the reliability of the measurements. Furthermore, solving the inverse problem presents its own challenges, particularly regarding the non-uniqueness of solutions. Although optimization techniques for tuning the initial measurement and process uncertainty, can partially mitigate these issues, the best estimation results are not always obtained with the optimized initial parameters.

Moreover, Kalman filtering techniques, including the CKF, inherently lack adaptive intelligence and long-term memory. The filter operates iteratively, estimating the covariance of

new states solely from the previous step, without integrating broader historical trends or learning from past data. Computational time represents also a significant limitation of the CKF framework, as it solves the underlying physical model $2n$ times at each iteration during the prediction step. This can be highly time-consuming, especially as model complexity and the size n of the state vector increases. In theory, the CKF architecture permits continuous data integration for real-time parameter estimation. However, in practice, it often fails to achieve true real-time performance due to the computing demands. Achieving genuine real-time operation require model simplification, parallelization strategies, or hardware acceleration techniques, especially for systems with rich and complex dynamics. As a result, KFT alone are insufficient for the development of digital twins, particularly when long-term prediction, autonomous adaptation or true real time monitoring are required. Building a functional DT demands complementary techniques, such as machine learning algorithms, to enhance flexibility, prediction capability, and self-updating behavior.

6.3 Future Research

This project is part of the broader effort to build a digital twin of a hydroelectric production unit. Based on the limitations discussed, several directions for future research can be outlined. From an experimental standpoint, we could redesign the excitation method to excite the beam directly from the cantilever base, as demonstrated in Habtour et al. (2022). This approach would eliminate the effects of beam–shaker interaction and enable higher vibration amplitudes and stronger nonlinear responses. From a modeling perspective, future work should focus on refining the damping formulation to better capture the physical mechanisms observed experimentally, especially for the spring mechanism. To include frictional effects and obtain a more realistic representation of the energy dissipation in the system, we could develop amplitude-dependent or localized damping representations. Integrating damping descriptions into the numerical model would provide a more realistic description of the observed behavior and enhance the accuracy of the estimation process. Then, form algorithmic perspective, future work should prioritize uncertainty quantification, especially for measurement and process noise. In the current CKF-based approach, the NOMAD algorithm optimizes process and measurement noise covariances because their values are difficult to quantify. Developing techniques to systematically quantify modeling and measurement uncertainties would enhance estimation reliability without depending solely on optimization or trial-and-error.

In this work, we demonstrated the application of the CKF specifically for parameter identification in a simplified vibrating system. Beyond this, Kalman filters can be extended to

damage detection by tracking dynamic changes or parameter variations that indicate deterioration in system health, as demonstrated by Laperle (2025). Additionally, Kalman filters are effective virtual sensing tools because they can estimate unmeasured states. However, Kalman filtering alone is insufficient for building a fully functional digital twin with real-time monitoring and predictive capabilities. Future research should explore integrating Kalman filtering for parameter identification, damage detection, and virtual sensing within a broader digital twin framework to create a modular and versatile system. Combining CKF with machine learning or artificial intelligence techniques can produce hybrid frameworks capable of autonomous model correction, uncertainty quantification, and enhanced prediction (Rosafalco et al., 2025). Integrating these approaches to build digital twins and overcome the limitations of traditional model-based filtering remains an open avenue for research.

REFERENCES

Abohamer, M., Amer, T., Arab, A., and Galal, A. (2025). 2.2-F) Analyzing the chaotic and stability behavior of a duffing oscillator excited by a sinusoidal external force. *Journal of Low Frequency Noise, Vibration and Active Control*, 44(2):969–986. Publisher: SAGE Publications Ltd STM.

Adams, M. L. (2001). *IN) Rotating machinery vibration: from analysis to troubleshooting*. Number 130 in Mechanical engineering. Dekker, New York, NY.

Afshari, H., Gadsden, S., and Habibi, S. (2017). Gaussian filters for parameter and state estimation: A general review of theory and recent trends. *Signal Processing*, 135:218–238.

Akhlaghi, S., Zhou, N., and Huang, Z. (2017). Adaptive adjustment of noise covariance in kalman filter for dynamic state estimation. In *2017 IEEE power & energy society general meeting*, pages 1–5. IEEE.

Arasaratnam, I. and Haykin, S. (2009). Cubature kalman filters. *IEEE Transactions on automatic control*, 54(6):1254–1269.

Arthur, R., French, M., Ganguli, J., Kinard, D., Kraft, E., Marks, I., Matlik, J., Fischer, O., Sangid, M., Seal, D., et al. (2020). Digital twin: Definition & value—aiaa and aia position paper. *AIAA Digital Engineering Integration Committee*.

Audet, C., Digabel, S. L., Montplaisir, V. R., and Tribes, C. (2021). Nomad version 4: Nonlinear optimization with the mads algorithm. Rapport technique, Groupe d?études et de recherche en analyse des décisions, GERAD, Montréal QC H3T 2A7, Canada.

Bergs, T., Gierlings, S., Auerbach, T., Klink, A., Schraknepper, D., and Augspurger, T. (2021). The concept of digital twin and digital shadow in manufacturing. *Procedia CIRP*, 101:81–84.

Brandt, A. (2023). *Noise and vibration analysis: signal analysis and experimental procedures*. John Wiley & Sons.

Brennan, M., Kovacic, I., Carrella, A., and Waters, T. (2008). On the jump-up and jump-down frequencies of the duffing oscillator. *Journal of Sound and Vibration*, 318(4-5):1250–1261.

Butlin, T., Woodhouse, J., and Champneys, A. (2015). The landscape of nonlinear structural dynamics: an introduction.

Chatzi, E. N. and Smyth, A. W. (2009). The unscented kalman filter and particle filter methods for nonlinear structural system identification with non-collocated heterogeneous sensing. *Structural Control and Health Monitoring: The Official Journal of the International Association for Structural Control and Monitoring and of the European Association for the Control of Structures*, 16(1):99–123.

Chen, Z., Heckman, C., Julier, S., and Ahmed, N. (2018). Weak in the nees?: Auto-tuning kalman filters with bayesian optimization. In *2018 21st International Conference on Information Fusion (FUSION)*, pages 1072–1079. IEEE.

Cloutier, D., Avitabile, P., Bono, R., and Peres, M. (2009). Shaker/stinger effects on measured frequency response functions. In *Proceedings of the 27th International Modal Analysis Conference*, volume 122.

Dollon, Q., Ghorbani, E., and Gosselin, F. P. (2025). Bayesian input-state-parameter inference of hydrodynamic bearings: From partial displacement measurements to force reconstruction. *Mechanical Systems and Signal Processing*, 230:112610.

Duffing, G. (1918). *Erzwungene Schwingungen bei veränderlicher Eigenfrequenz und ihre technische Bedeutung*. Number 41-42. Vieweg.

Ewins, D. J. (2000). *IN) Modal testing: theory, practice and application*. Number 10 in Mechanical engineering research studies engineering dynamics series. Research Studies Press, Baldock, 2. ed edition.

Gabos, Z. and Dombovari, Z. (2025). Open-loop swept frequency response of nonlinear structures subjected to weak coupling. *Nonlinear Dynamics*, 113(6):5091–5108.

Garcia, R. V., Pardal, P. C. P. M., Kuga, H. K., and Zanardi, M. (2019). Nonlinear filtering for sequential spacecraft attitude estimation with real data: Cubature kalman filter, unscented kalman filter and extended kalman filter. *Advances in Space Research*, 63(2):1038–1050.

Ghorbani, E. (2021). *Nonlinear Kalman Filtering Based Damage Quantification for Civil Infrastructure*. Doctor of Phylosophy, The University of Manitoba.

Ghorbani, E. and Cha, Y.-J. (2018). An iterated cubature unscented kalman filter for large-dof systems identification with noisy data. *Journal of Sound and Vibration*, 420:21–34.

Ghorbani, E., Dollon, Q., and Gosselin, F. P. (2025). Physics-aware tuning of the unscented kalman filter: statistical framework for solving inverse problems involving nonlinear dynamical systems and missing data. *Nonlinear Dynamics*, 113(5):4301–4323.

Giroux, A.-M., Gauthier, J.-P., and Dollon, Q. (2023). Application of the Digital Twin Concept for Operation and Maintenance of Hydro Generating Units.

Givois, A., Tan, J.-J., Touzé, C., and Thomas, O. (2020). 2.2.BB) Backbone curves of coupled cubic oscillators in one-to-one internal resonance: bifurcation scenario, measurements and parameter identification. *Meccanica*, 55(3):481–503.

Gouvernement du Canada, L. R. d. l. d. C. (2024). ONÉ - Profils énergétiques des provinces et territoires – Québec. Last Modified: 2024-09-10.

Greś, S., Döhler, M., Dertimanis, V. K., and Chatzi, E. N. (2025). Subspace-based noise covariance estimation for kalman filter in virtual sensing applications. *Mechanical Systems and Signal Processing*, 222:111772.

Guo, G. and Zhao, S. (2022). 3d multi-object tracking with adaptive cubature kalman filter for autonomous driving. *IEEE Transactions on Intelligent Vehicles*, 8(1):512–519.

Habtour, E., Di Maio, D., Masmeijer, T., Cordova Gonzalez, L., and Tinga, T. (2022). Highly sensitive nonlinear identification to track early fatigue signs in flexible structures. *Journal of Nondestructive Evaluation, Diagnostics and Prognostics of Engineering Systems*, 5(2):021005.

He, J. and Fu, Z.-F. (2001). *IN) Modal analysis*. Butterworth-Heinemann, Oxford Boston.

He, J.-H. (2006). Some asymptotic methods for strongly nonlinear equations. *International journal of Modern physics B*, 20(10):1141–1199.

Hippold, P., Wei, T., Zhou, T., Mueller, F., Scheel, M., Pacini, B., Renson, L., Schwingshackl, C., and Krack, M. (2022). Handling shaker-structure interactions in nonlinear dynamic testing. Technical report, Sandia National Lab.(SNL-NM), Albuquerque, NM (United States).

Hoshiya, M. and Saito, E. (1984). Structural identification by extended kalman filter. *Journal of engineering mechanics*, 110(12):1757–1770.

Hydro-Québec (2023). Plan d'action 2035 : Vers un québec décarboné et prospère. Rapport, Hydro-Québec, Montréal, Québec, Canada. Dépôt légal : novembre 2023. ISBN 978-2-550-96175-8 (PDF, français). La version française fait foi.

Hydro-Québec (2024). Wind power development strategy: Charting the course toward collective success. Report, Hydro-Québec, Montréal, Québec, Canada. Legal deposit – 2nd quarter 2024. ISBN 978-2-550-97696-7 (PDF, English). The original French text prevails.

Hydro-Québec (2025). Une approche évolutive pour une ambition de 3 000 mw d'énergie solaire au québec : Le solaire, une autre étape vers la diversification énergétique. Rapport, Hydro-Québec, Montréal, Québec, Canada. Dépôt légal : 2025. Référence : 2025G217F. La version française fait foi.

Jimenez, J. J. M., Schwartz, S., Vingerhoeds, R., Grabot, B., and Salaün, M. (2020). Towards multi-model approaches to predictive maintenance: A systematic literature survey on diagnostics and prognostics. *Journal of manufacturing systems*, 56:539–557.

Julier, S. J. and Uhlmann, J. K. (1997). New extension of the kalman filter to nonlinear systems. In *Signal processing, sensor fusion, and target recognition VI*, volume 3068, pages 182–193. Spie.

Julier, S. J. and Uhlmann, J. K. (2004). Unscented filtering and nonlinear estimation. *Proceedings of the IEEE*, 92(3):401–422.

Julier, S. J., Uhlmann, J. K., and Durrant-Whyte, H. F. (1995). A new approach for filtering nonlinear systems. In *Proceedings of 1995 American Control Conference-ACC'95*, volume 3, pages 1628–1632. IEEE.

Kalman, R. E. (1960). A new approach to linear filtering and prediction problems.

Kalman, R. E. and Bucy, R. S. (1961). New results in linear filtering and prediction theory.

Kang, Y., Qiu, Z., Fan, Q., Zhang, H., Shi, Z., and Gu, F. (2022). Tacholess estimation of time-varying dynamic coefficients of journal bearing based on the square-root cubature kalman filter. *Measurement*, 203:111956.

Khodarahmi, M. and Maihami, V. (2023). A review on kalman filter models. *Archives of Computational Methods in Engineering*, 30(1):727–747.

Kontoroupi, T. and Smyth, A. W. (2016). Online noise identification for joint state and parameter estimation of nonlinear systems. *ASCE-ASME Journal of Risk and Uncertainty in Engineering Systems, Part A: Civil Engineering*, 2(3):B4015006.

Korsch, H. J., Jodl, H.-J., and Hartmann, T. (2008). *Chaos: a program collection for the PC*, chapter 8 – The Duffing Oscillator, pages 157–184. Springer Berlin Heidelberg, Berlin, Heidelberg.

Kovacic, I. and Brennan, M. J., editors (2011). *The Duffing Equation: Nonlinear Oscillators and their Behaviour*. Wiley, 1 edition.

Laperle, V. (2025). Kalman filter-based digital twin framework for anomaly detection and system identification of a pipe conveying fluid. Master's thesis, Polytechnique Montréal.

Li, R., Arzaghi, E., Abbassi, R., Chen, D., Li, C., Li, H., and Xu, B. (2020). Dynamic maintenance planning of a hydro-turbine in operational life cycle. *Reliability Engineering & System Safety*, 204:107129.

Liang, H., Moya, B., Seah, E., Weng, A. N. K., Baillargeat, D., Joerin, J., Zhang, X., Chinesta, F., and Chatzi, E. (2025). Harnessing hybrid digital twinning for decision-support in smart infrastructures. *Data-Centric Engineering*, 6:e43.

Mayes, R. L. and Gomez, A. J. (2006). Part 4: what's shakin', dude? effective use of modal shakers. *Experimental Techniques*, 30(4):51–61.

McClellan, A., Lorenzetti, J., Pavone, M., and Farhat, C. (2022). A physics-based digital twin for model predictive control of autonomous unmanned aerial vehicle landing. *Philosophical Transactions of the Royal Society A*, 380(2229):20210204.

Meirovitch, L. (2010). *Fundamentals of vibrations*. Waveland Press.

Menegaz, H. M. T., Ishihara, J. Y., Borges, G. A., and Vargas, A. N. (2015). A systematization of the unscented kalman filter theory. *IEEE Transactions on Automatic Control*, 60(10):2583–2598.

Moatimid, G. M., Amer, T. S., and Amer, W. S. (2023). 2.2-DF) Dynamical analysis of a damped harmonic forced duffing oscillator with time delay. *Scientific Reports*, 13(1):6507.

Modak, S. V. (2023). *IN) Analytical and Experimental Modal Analysis*. CRC Press, Boca Raton, 1 edition.

Mohammadali, M. and Ahmadian, H. (2016). Improvement in modal testing measurements by modeling and identification of shaker–stinger–structure interactions. *Experimental Techniques*, 40(1):49–57.

Noël, J. and Kerschen, G. (2017). Nonlinear system identification in structural dynamics: 10 more years of progress. *Mechanical Systems and Signal Processing*, 83:2–35.

Nässelqvist, M., Gustavsson, R., and Aidanpää, J.-O. (2013). IN) A Methodology for Protective Vibration Monitoring of Hydropower Units Based on the Mechanical Properties. *Journal of Dynamic Systems, Measurement, and Control*, 135(041007).

Peng, J., Luo, J., He, H., and Lu, B. (2019). An improved state of charge estimation method based on cubature kalman filter for lithium-ion batteries. *Applied energy*, 253:113520.

Peres, M. A. and Bono, R. W. (2011). Modal testing excitation guidelines. *Sound & vibration*, 45(11).

Romanenko, A. and Castro, J. A. (2004). The unscented filter as an alternative to the ekf for nonlinear state estimation: a simulation case study. *Computers & Chemical Engineering*, 28(3):347–355.

Rosafalco, L., Conti, P., Manzoni, A., Mariani, S., and Frangi, A. (2025). Online learning in bifurcating dynamic systems via sindy and kalman filtering. *Nonlinear Dynamics*, pages 1–21.

Sadati, S. S., Nobari, A., and Naraghi, T. (2012). Identification of a nonlinear joint in an elastic structure using optimum equivalent linear frequency response function. *Acta Mechanica*, 223(7):1507–1516.

Sadeghi, M. H. and Lotfan, S. (2017). Identification of non-linear parameter of a cantilever beam model with boundary condition non-linearity in the presence of noise: an nsi-and ann-based approach. *Acta Mechanica*, 228(12):4451–4469.

Santo, D. R., Mencik, J.-M., and Goncalves, P. J. P. (2020). On the multi-mode behavior of vibrating rods attached to nonlinear springs. *Nonlinear Dynamics*, 100(3):2187–2203.

Sari, M. S. and Al-Solihat, M. K. (2025). Free and forced nonlinear vibrations of a functionally graded porous cantilever beam with an intermediate spring subjected to a harmonic tip force. *Journal of Vibration Engineering & Technologies*, 13(1):92.

Scardua, L. A. and Da Cruz, J. J. (2017). Complete offline tuning of the unscented kalman filter. *Automatica*, 80:54–61.

Shaw, A., Hill, T., Neild, S., and Friswell, M. (2016). Periodic responses of a structure with 3:1 internal resonance. *Mechanical Systems and Signal Processing*, 81:19–34.

Sun, Y., Bao, W., Qu, S., Li, Q., Jiang, P., Zhou, Z., and Shi, P. (2023). Development of the consider cubature kalman filter for state estimation of hydrological models with parameter uncertainty. *Journal of Hydrology*, 625:130080.

Taghipour, J., Khodaparast, H. H., Friswell, M. I., Shaw, A. D., Jalali, H., and Jamia, N. (2022). Harmonic-balance-based parameter estimation of nonlinear structures in the

presence of multi-harmonic response and force. *Mechanical Systems and Signal Processing*, 162:108057.

Tang, B., Brennan, M., and Gatti, G. (2018). Use of the dynamic stiffness method to interpret experimental data from a nonlinear system. *Journal of Sound and Vibration*, 421:91–110.

Tian, Y., Huang, Z., Tian, J., and Li, X. (2022). State of charge estimation of lithium-ion batteries based on cubature kalman filters with different matrix decomposition strategies. *Energy*, 238:121917.

Tidriri, K., Chatti, N., Verron, S., and Tiplica, T. (2016). Bridging data-driven and model-based approaches for process fault diagnosis and health monitoring: A review of researches and future challenges. *Annual reviews in control*, 42:63–81.

Tripura, T., Bhowmik, B., Pakrashi, V., and Hazra, B. (2020). Real-time damage detection of degrading systems. *Structural Health Monitoring*, 19(3):810–837.

Varoto, P. S. and de Oliveira, L. P. R. (2002). On the force drop off phenomenon in shaker testing in experimental modal analysis. *Shock and Vibration*, 9(4-5):165–175.

Wang, B., Costa-Castello, R., Na, J., de la Torre, O., and Escaler, X. (2022). Modeling and adaptive parameter estimation for a piezoelectric cantilever beam. *IEEE transactions on circuits and systems I: regular papers*, 70(1):481–491.

Wang, S. and Tang, B. (2022). 2.2.BB) A Comparative Study of Parameter Identification Methods for Asymmetric Nonlinear Systems with Quadratic and Cubic Stiffness. *Sensors (Basel, Switzerland)*, 22(15):5854.

Wawrzynski, W. (2021). Duffing-type oscillator under harmonic excitation with a variable value of excitation amplitude and time-dependent external disturbances. *Scientific reports*, 11(1):2889.

Wright, L. and Davidson, S. (2020). How to tell the difference between a model and a digital twin. *Advanced Modeling and Simulation in Engineering Sciences*, 7(1):13.

Wu, M. and Smyth, A. W. (2007). Application of the unscented kalman filter for real-time nonlinear structural system identification. *Structural Control and Health Monitoring: The Official Journal of the International Association for Structural Control and Monitoring and of the European Association for the Control of Structures*, 14(7):971–990.

Younesian, D., Hosseinkhani, A., Askari, H., and Esmailzadeh, E. (2019). Elastic and viscoelastic foundations: a review on linear and nonlinear vibration modeling and applications. *Nonlinear Dynamics*, 97(1):853–895.

Zhang, G., Xiaochen, W., and Zhichun, Y. (2022). Study on excitation force characteristics in a coupled shaker-structure system considering structure modes coupling. *Chinese Journal of Aeronautics*, 35(7):227–245.

Zhang, G., Zang, C., and Friswell, M. I. (2020). Measurement of multivalued response curves of a strongly nonlinear system by exploiting exciter dynamics. *Mechanical Systems and Signal Processing*, 140:106474.

Zoljic-Beglerovic, S., Stettinger, G., Luber, B., and Horn, M. (2018). Railway suspension system fault diagnosis using cubature kalman filter techniques. *IFAC-PapersOnLine*, 51(24):1330–1335.

APPENDIX A INITIALIZATION OF THE CKF

Table A.1 **Experimental signal types and initial Values of states, parameters and variances, for the initialization of the CKF, for the two tests cases presented in Figure 5.5**

	Figure 5.5 (a)	Figure 5.5 (b)
Type	sin	chirp
Frequency [Hz]	15	9-11-9 (3 times)
Input Voltage [mV]	150	100
Duration [s]	12.2	60
L_s [m]	0.085	0.085
$\mathbf{x}_{0,\mathbf{q}}$	0.001	0.001
$\mathbf{x}_{0,\dot{\mathbf{q}}}$	0.01	0.01
EI_0 [Nm^2]	16.69	16.69
$P_{0,\mathbf{x}_{0,\mathbf{q}}}$	10^{-3}	10^{-3}
$P_{0,\mathbf{x}_{0,\dot{\mathbf{q}}}}$	10^{-3}	10^{-3}
$P_{0,EI}$	10^2	10^2
$\mathbf{Q}$	$10^{-6} \cdot \mathbf{I}_{7\times7}$	$10^{-6} \cdot \mathbf{I}_{7\times7}$
$\mathbf{R}$	$10^{-3} \cdot \mathbf{I}_{1\times1}$	$10^{-3} \cdot \mathbf{I}_{1\times1}$
α_Q	1	1
α_R	1	1